Synthesis, Characterisation and Biological Activity of a Series of Single-Ligand and Heteroleptic Copper(II) Schiff Base Complexes: Potential Chemotherapeutic Agents

Submitted in fulfilment of the requirement for the degree of

Master of Science

By

Teshica Chatturgoon

BSc, (Hons.) (UKZN)

November 2016

UNIVERSITY OF KWAZULU-NATAL

School of Chemistry and Physics,
University of KwaZulu-Natal
Pietermaritzburg

Declaration

I, Teshica Chatturgoon, declare that:

(i) The research reported in this thesis/dissertation, except where otherwise indicated, is my original research.

(ii) This thesis/dissertation has not been submitted for any degree or examination at any other university.

(iii) This thesis/dissertation does not contain other persons' data, pictures, graphs or other information, unless specifically acknowledged as being sourced from other persons.

(iv) This thesis/dissertation does not contain other persons' writing, unless specifically acknowledged as being sourced from other researchers. Where other written sources have been quoted, then:

a) Their words have been re-written but the general information attributed to them has been referenced;

b) Where their exact words have been used, their writing has been placed inside quotation marks, and referenced.

(v) Where I have reproduced a publication of which I am author, co-author or editor, I have indicated in detail which part of the publication was actually written by myself alone and have fully referenced such publications.

(vi) This dissertation/thesis does not contain text, graphics or tables copied and pasted from the internet, unless specifically acknowledged, and the source being detailed in the dissertation/thesis and in the References sections.

Signed: _____ Date: _____

Teshica Chatturgoon

I hereby certify that this statement is correct to the best of my knowledge:

Signed: _____ Date: _____

Dr. Matthew P. Akerman (Supervisor)

Acknowledgements

Foremost, I would like to express my sincere gratitude to my supervisor Dr M. P. Akerman for his assistance, guidance and input throughout the duration of this project. I acknowledge his expertise and encouragement throughout my post graduate years.

A very big thank you to Leigh Hunter for being a great mentor throughout my postgraduate years, for proof reading my thesis and for all the guidance and advice.

Thank you to the Akerman Research Group for all the great memories and support.

I would like to thank Mr C. Grimmer and Mrs C. Janse van Rensburg for their assistance with my data collection. Their willingness to assist wherever possible is most appreciated.

Thank you to the School of Chemistry and Physics on the Pietermaritzburg campus of the University of Kwazulu-Natal for creating a conducive environment for my studies.

My heartfelt thanks to the South African National Research Foundation for awarding me the Scare Skills Scholarship which aided me in pursuing my studies.

I am forever grateful for all the support, guidance and encouragement from my parents Suresh and Shobhana Chatturgoon and my brother Samil throughout my university career.

To Pranesh, who has been most understanding and supportive throughout my university career. Thank you for all the encouragement, motivation and for being my pillar of strength.

“If I have been able to see further, it is because I have stood on the shoulders of giants.”

-Sir Isaac Newton

This thesis is dedicated to my parents who have been my giants.

Without them, I will not be who I am today nor will I have accomplished what I have.

Publications

1. Bezuidenhout, Daniela I., Belinda Van der Westhuizen, Pieter J. Swarts, Teshica Chatturgoon, Orde Q. Munro, Israel Fernández, and Jannie C. Swarts. *Chemistry - A European Journal* 20, no. 17 (2014): 4974-4985.

2. Akerman, Matthew P., Teshica Chatturgoon, and Orde Q. Munro. *Inorganica Chimica Acta* 421 (2014): 292-299.

3. Teshica Chatturgoon, and Matthew P. Akerman. *Acta Crystallographica Section C: Structural Chemistry* 72, no. 3 (2016): 234-238.

List of Abbreviations

%Diff.	percentage difference
Å	Angstrom
°	degrees
A	Absorbance
A_2	binding site size
a	Lattice constant
aq	Aqueous
B3LYP	Becke three parameter Lee-Yang Parr
Bpy	2,2'-Bipyridine
br	broad
Calc.	calculated
CSD	Cambridge Structural Database
ctDNA	Calf Thymus DNA
D_2O	Deuterated Water
d	doublet
DCM	dichloromethane
dd	doublet of doublets
DFT	Density Functional Theory
DMF	*N, N'*-dimethylformamide
DMSO	dimethyl sulfoxide
DMSO-d_6	deuterated dimethyl sulfoxide
DNA	deoxyribonucleic acid

DNA-EB	deoxyribonucleic acid ethidium bromide
DPQ	pyrazino[2,3-f][1,10]phenanthroline
DPPZ	dipyrido[3,2-a:2',3'-c]phenazine
(e)	electron units
E	energy
EB	ethidium bromide
EB-ctDNA	ethidium bromide calf-thymus DNA
eq.	equivalent
ES	electron spray
Exp.	experimental
FT-IR	Fourier transform infra-red
g	gram/ gas
GI_{50}	growth inhibition 50%
I	nuclear spin quantum number
IC_{50}	inhibitory concentration 50%
IR	infra-red
J	coupling constant
K	kelvin
k_{app}	apparent binding constant
k_{EB}	ethidium bromide binding constant
LanL2DZ	Los Alamos National Labs Double Zeta
LC_{50}	lethal concentration 50%
LMCT	Ligand to metal charge transfer
LUMO	lowest unoccupied molecular orbital
m	multiplet/ medium intensity

M^+	positive molecular ion
M^-	negative molecular ion
MO	molecular orbital
MS	mass spectrum
MRI	magnetic resonance imaging
m/z	mass to charge ratio
n	nonbonding orbital
NMR	Nuclear Magnetic Resonance
PBE	Perdew, Burke and Ernzerhof
Phen	1,10-phenanthroline
Phen-NH_2	1,10-phenanthroline-5-amine
ppm	parts per million
RMSD	root mean-square deviation
s	singlet/ strong
t	triplet
TGI	total growth inhibition
THF	tetrahydrofuran
T_m	melting temperature
TMS	tetramethyl silane
TOF	time of flight
tris	tris(hydroxymethyl)aminomethane
UV	ultraviolet
vis	visible
w	weak
XRD	X-ray diffraction

List of Figures

Chapter 1

Chapter 2

Chapter 3

Chapter 4

Chapter 5

Chapter 6

Chapter 7

Chapter 8

List of Tables

Abstract

In this study, a range of single-ligand and heteroleptic copper(II) Schiff base chelates were synthesised as potential chemotherapeutic agents. The copper(II) chelates are anticipated to exert their cytotoxicity *via* DNA cleavage (through the production of hydroxyl radicals) and DNA binding. Three single-ligand copper(II) chelates were successfully synthesised and characterised. Two of these had *N,N',N''* donor atom sets: $[Cu(L)(Cl)_2]$ and $[Cu(L2)(Cl)_2]$, which were synthesised by the reactions of pyridine-2-carbaldehyde with picolylamine and 8-aminoquinoline, respectively. The third Schiff base had *N,N',O* donor atoms and was synthesised by the reaction of salicylaldehyde and 8-aminoquinoline. Reaction of the respective ligands with $CuCl_2$ yielded the desired chelates. [Cu(L1)(Cl)] was then further reacted with three co-ligands: 2,2'-bipyridyl, 1,10-phenanthroline and 1,10-phenanthroline-5-amine to afford three heteroleptic chelates. The ligands and chelates have been characterised by mass spectrometry, CHN analysis as well as NMR (where possible), IR and UV/vis spectroscopy. DNA binding affinities of the copper(II) chelates were measured using fluorescence competitive binding assays. The binding affinities of the complexes ranged from $1.75 \times 10^5 – 8.65 \times 10^5$ M^{-1}. [Cu(L1)(Cl)] was the strongest binder, while $[Cu(L)(Cl_2)]$ was the weakest.

The solid state structures of two single-ligand and the three heteroleptic chelates were elucidated. The copper(II) chelates all exhibited a square pyramidal coordination geometry. Measurements of the angle subtended by the ligand planes showed interesting variations of ring bending as well as angle deviations in the three heteroleptic complexes. DFT simulations were used to run geometry optimisations on all copper(II) chelates at the B3LYP/6-311G(d,p) level of theory to investigate the influence of intermolecular forces on the geometry of the chelates. RMSDs for both the single-ligand and heteroleptic chelates were low indicating good correlation between the gas phase and solid state structures. The similarity of the structures suggests that an appropriate level of theory was applied in the simulations. The key difference in the structures was the angle subtended by the primary and co-ligands in the absence of packing constraints. The DFT-optimised structures tended towards a trigonal bipyramidal geometry as opposed to a square pyramidal geometry.

Hydroxyl radical studies showed that all the copper(II) chelates have the ability to produce hydroxyl radicals *in situ* in the presence of ascorbic acid and hydrogen peroxide. The *in vitro* cytotoxicity of all six copper(II) chelates were assessed against a panel of four human cell lines of which three were cancer cell lines: TK-10, U937 and MT-4. The forth cell line was a normal human cell line and was used as a control (HEK293). The most active copper(II) chelate was $[Cu(L)(Cl)_2]$ with the highest mean activity (IC_{50} = 2.19 µM) against the three cancer cell lines. $[Cu(L)(Cl)_2]$ was also screened against HEK293 and showed lower cytotoxicity (IC_{50} = 3.18). The cytotoxicity in general did not correlate with the DNA binding affinities, suggesting that the mechanism of action may be more complicated than simply inhibiting cell replication through DNA binding. The catalytic production of reactive oxygen species is therefore likely a key aspect in the mechanism of action.

Table of Contents

Chapter 1 | Introduction

1.1 Preface

Cancer is a genetic disease which has plagued humankind for generations. It has become a global health threat, affecting individuals all around the world, regardless of socioeconomic status. Cancer remains the second leading cause of death in developing countries and the number one cause of death in developed countries.[1] Statistics from the National Cancer Institute (USA) show that the most prevalent cancers in 2016 are of the breast, lung and bronchus, prostate and colon.[1] In 2016, an estimated 1,685,210 new cases of cancer will be diagnosed in the United States alone and 595,690 people will die from this disease. The number of new cancer cases worldwide is expected to rise to 22 million within the next two decades.[1]

These alarming statistics have fuelled cancer research for the past four decades. However, drawbacks such as the lack of selectivity and toxic side effects of current chemotherapeutics have prompted researchers to continue development of new and improved drugs which are aimed to be more selective with reduce side effects.[2]

Metals play various roles within living systems and medicinal inorganic chemistry has been practiced for millennia. The first recorded medicinal use of copper was found in an ancient Egyptian medical text, written between 2600 and 2200 B.C., which records the use of copper to sterilise chest wounds and drinking water.[3] Copper has since been shown to have numerous antibacterial and antifungal properties and its cytotoxicity when used as a base for chemotherapeutics has shown promising results.[4] An additional advantage of copper derived chemotherapeutics is that they are one of few classes of compounds with the potential for both diagnosis and treatment of cancerous lesions.[4]

This study focuses on the synthesis of single-ligand and heteroleptic Schiff base copper(II) chelates which are anticipated to exert their cytotoxicity by two mechanisms: Firstly, by intercalating between the base pairs of the DNA helix, hindering DNA replication. Secondly, copper(II), being a redox active metal, can catalyse the production of hydroxyl radicals which will cleave DNA inducing tumour cell apoptosis. The significance of selecting Schiff bases, heteroleptic chelate systems and copper(II) will be outlined in this chapter.

1.2 Transition Metals in Medicine

It is a well-established fact that most drugs in the pharmaceutical sector are "organic" in nature. However, in recent years other elements in the Periodic Table, metals in particular, have been shown to have important medicinal properties with some being essential for normal biological function in humans.[5] The discipline of inorganic medicinal chemistry was born after the serendipitous discovery of the platinum-based anticancer drug cisplatin, which remains one of the best-selling anticancer drugs today.[2] Cisplatin and its derivatives, oxaliplatin and carboplatin, have been very effective in treating cancer, but show activity towards only a limited number of tumours. Further drawbacks of using platinum-based drugs are that secondary tumours often show drug resistance during treatment and they induce intense side effects.[2]

These findings led to the progression of inorganic medicinal chemistry away from solely platinum-based drugs. Current research in medicinal inorganic chemistry is directed towards two goals. The first is the synthesis of new anticancer drugs with the potential to overcome the issues of drug resistance. The second focus is to develop metal-based drugs with higher selectivity towards neoplastic tissue over healthy tissue leading to a significant reduction in the side effects of treatment.[2] Clinical and preclinical research have shown that the development of new cytostatic metal agents with novel modes of action can be achieved.[6] The application of metals in medicinal chemistry may at first seem an odd choice. However, provided the metal ions can be stabilised in the reducing cellular environment of mammalian cells, they can serve as an ideal scaffold around which ligands baring cell targeting groups can be attached in a precise three-dimensional arrangement. Gold, iron and cobalt complexes have already shown encouraging results in preclinical studies while gallium, titanium and ruthenium metal complexes have passed into phase I and phase II clinical trials.[6] These metal-based drugs and drug candidates are discussed below.

Gold(I)-based compounds, particularly cyanide complexes, were used in the treatment of human and bovine tuberculosis (TB) for several years in the early 20th century.[6] Auranofin, a gold(I) phosphine complex is one of the compounds used for the treatment of rheumatoid arthritis. However, in the early 1980s reports showed that Auranofin and other gold(I) phosphine complexes could inhibit the growth of tumour cells *in vitro*. Auranofin did not interact directly with DNA like other gold complexes, but inhibited synthesis of RNA, DNA and protein at cytotoxic concentrations. Exposing cells to Auranofin also resulted in morphological

changes such as cell rounding and surface membrane changes.[6] Figure 1.2.1 shows the structure of the gold(I) complex Auranofin.

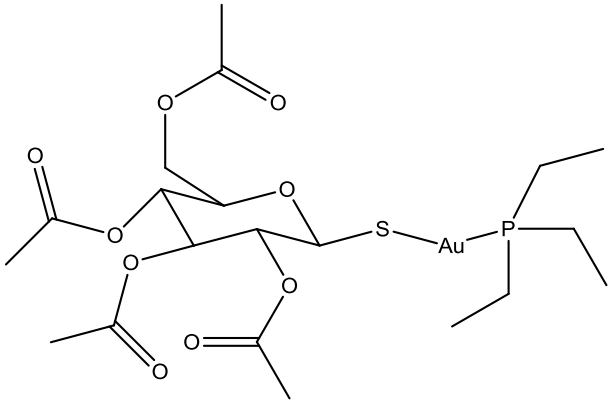

Figure 1.2.1: Structure of the gold(I) anti-arthritic and anti-tumour agent Auranofin.[3]

Gold(III) complexes show electronic and structural similarities to cisplatin rendering them ideal candidates in the search for potential anticancer agents. A drawback of gold(III) complexes is that they exhibit low stability under physiological conditions which has slowed the development of these drugs.[7] A wide range of gold(III) complexes with various ligands have in recent years been synthesised and biochemically investigated. Most of these complexes contain Au-N bonds for example, $[Au(phen)Cl_2]Cl$, $[Au(terpy)Cl]Cl_2$ and $[AuCl(dien)]Cl_2$ (depicted in Figure 1.2.2). These complexes all showed good stability in physiological-like environments. In addition, all three compounds showed promising cytotoxic activities towards human ovarian cancer cells (A2780).[7]

It is also noted that this class of complexes could overcome the issue of drug resistance in cisplatin-resistant A2780 cells.[7] In the presence of thiosulfate or ascorbate, the compounds $[Au(phen)Cl_2]Cl$ and $[Au(terpy)Cl]Cl_2$ were readily reduced indicating the release of their toxic ligands upon *in vivo* reduction could be the reason for their bioactivity.[7]

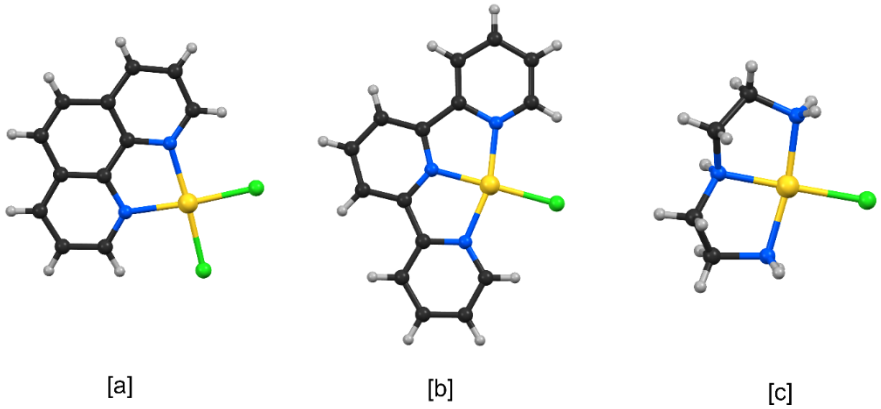

Figure 1.2.2: Cytotoxic gold(III) complexes with N-donor ligands (a) $[Au(phen)Cl_2]Cl$, (b) $[Au(terpy)Cl]Cl_2$ and (c) $[AuCl(dien)]Cl_2$.

Budotitane and titanocene dichloride, Figure 1.2.3, are titanium complexes which have both passed into clinical trials. Preclinical trials of these complexes have shown cytotoxic activity against a wide variety of cancerous tissues. Budotitane was studied in a clinical phase I trial which showed no objective tumour response.[6] Titanocene dichloride delivered encouraging results in phase I trials and was moved to phase II trials. Once in phase II trials, patients with metastatic renal-cell carcinoma showed no response. The hydrolytic instability under physiological conditions and the poor solubility in aqueous media of titanocenium compounds are cited as the likely reasons for the low activity in clinical studies.[6]

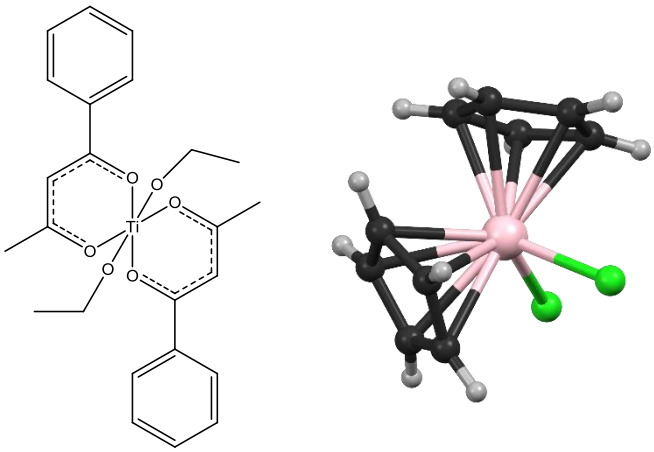

Figure 1.2.3: Structures of cytotoxic titanium complexes (a) budotitane and (b) titanocene dichloride.

Reports indicating the potential anti-cancer properties of ruthenium complexes surfaced as early as the 1970s, thus leading to increased efforts in this field. Numerous potential chemotherapeutics have since emerged, such as the octahedral ruthenium(III) complexes NAMI-A and KP1019, shown in Figure 1.2.4, which have entered clinical trials.[6] KP1019 showed cell growth inhibitory effects on cultured cancer cells and is efficiently taken up by cells inducing apoptosis *via* mitochondrial pathways.[6]

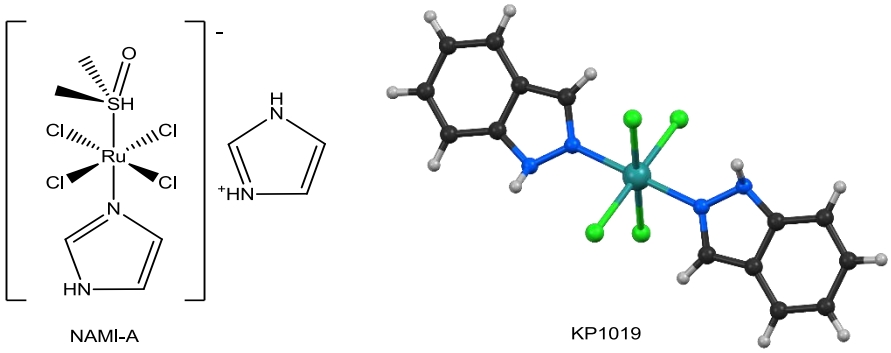

Figure 1.2.4: Ruthenium complexes NAMI-A and KP1019, which have entered clinical trials for the treatment of various malignant tumours.[3]

The examples above are just a small extract of the vast library of metal chelates which have shown potential in drug research. The inclusion of metal ions in the next generation of chemotherapeutics will hopefully adjust mechanisms of action, helping to overcome the issues associated with current therapies. Targeted drug delivery with correspondingly reduced side effects holds the key to more effective and selective drug administration; this can be achieved with metal-based chemotherapeutics.[8]

1.3 Copper Chemistry

The applications of copper in medicinal chemistry date back centuries when ancient Egyptians, Romans, Greeks and Aztecs reported the application of copper for the treatment of various ailments.[9] Copper is an essential element for plants, animals and humans and for this reason it is believed that copper-based medicinal compounds could be less toxic to healthy tissue than exogenous metals such as platinum.[9]

The aqueous coordination chemistry of copper is limited to its three accessible oxidation states (I-III). Copper(I) has a diamagnetic d^{10} configuration and forms complexes without any crystal field stabilisation energy. Copper(II) is a d^9 metal of borderline softness, which favours a wide range of coordination geometries. Copper(III) is uncommon and is only stable with the use of strong π-donor ligands.[10]

The d^9 electronic configuration of copper(II) makes it subject to Jahn-Teller distortion when placed in an environment of cubic symmetry. The Jahn-Teller effect which describes the geometrical distortion of ions and molecules is associated with certain electronic configurations. The Jahn–Teller theorem states that any non-linear molecule with a spatially degenerate electronic ground state will undergo a geometrical distortion that removes that degeneracy, because the distortion lowers the overall energy of the species. The effect is most commonly encountered in octahedral complexes of the transition metals.[11]

Copper(II) favours coordination to amines, imines, and bidentate ligands to form distorted square-planar, square-pyramidal, trigonal-pyramidal, and distorted octahedral geometries. When hexa-coordinate, the typical distortion is an elongation along one four-fold axis i.e. four normal bonds lie in a square-planar configuration (equatorial positions) and two longer or shorter bonds occur above and below the plane (axial positions). This distortion is a result of the Jahn-Teller effect. [12]

1.3.1 Copper-Based Antimicrobials

Research has shown copper, particularly copper(II), to have both antimicrobial and anticancer properties.[13] Antimicrobial agents have the ability to kill or inactivate microbes, such as bacteria, fungi and viruses. Numerous scientific studies have shown that copper has a reliable antimicrobial activity against some toxic bacteria, viruses and fungi including *Escherichia coli, Bacillus subtilis* and *Staphylococcus aureus* to name a few.[4] Antibiotic resistance is also on the increase and research to develop new, more efficient drugs to control pathogenic organisms is an ongoing process.

There are various mechanisms through which copper exerts its activity as an antimicrobial agent. These mechanisms include:

- The alteration of the three-dimensional structure of proteins by coordination to various amino acids in the proteins which leads to the inactivation of viruses and bacteria.[14]
- The formation of highly reactive hydroxyl radicals by copper(II) complexes which inactivate viruses by impairing the viral proteins.[15]
- Copper readily binds to the sulfur, carboxylate-containing and amino groups of proteins disrupting the structure and functions of enzymes.[16]
- Copper interacts with lipids resulting in peroxidation and the formation of holes in the cell membrane resulting in leakage of essential solutes.[17]
- The cellular metabolism in *Escherichia coli* cells is impaired by damage to the respiratory chain caused by copper.[18]

In a study by Mezey *et al.* the antimicrobial potential of a series of copper(II) complexes was investigated along with the free ligand, pyridoxal isonicotinoyl hydrazone (HL), which acts as a control, against a spectrum of Gram-positive and Gram-negative bacteria. The antimicrobial activity of the solvents (pyridine and dimethylsulfoxide), HL and the newly synthesised copper(II) hydrazone compounds were tested against *Escherichia coli W3110, Pseudomonas aeruginosa ATCC 9027* (Gram-positive), *Staphylococcus aureus ATTC 6538* (Gram-negative) and *Bacillus cereus ATCC 14579* bacterial strains.[19] The study was successful in confirming a significantly higher antimicrobial activity for the copper(II) complexes compared to the free ligand. The increased antimicrobial activity of the copper(II) hydrazone complexes is due to direct contact of the copper(II) complexes with the pathogenic bacteria. The chelates cause cell damage by membrane rupture resulting in loss of cytoplasmic content and loss of

membrane potential leading to cell death.[19] Figure 1.3.1 illustrates the solid state structure of HL as well as the proposed structure of the copper complex.

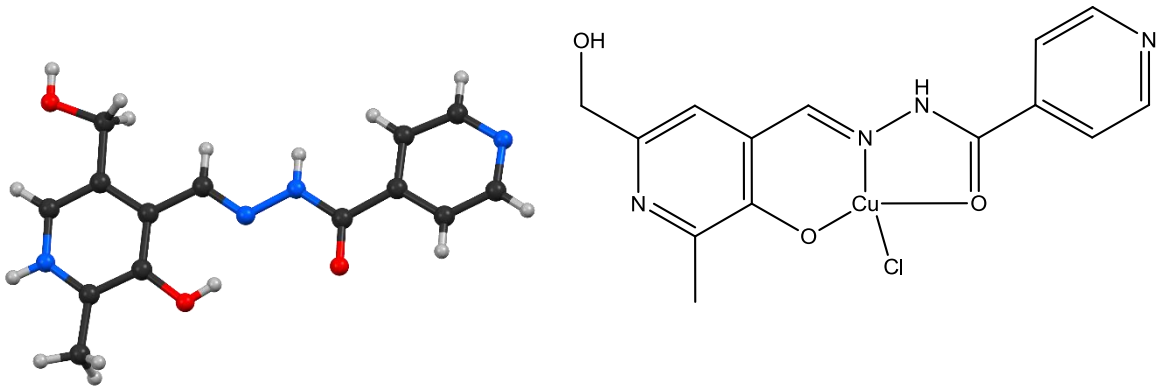

Figure 1.3.1: The ligand pyridoxal isonicotinoyl hydrazone (HL) and proposed structure of the copper(II) antimicrobial complex.[19]

1.3.2 Copper Toxicity

The toxicity of copper(II) originates from its ability to produce reactive oxygen species (ROS), as shown in Figure 1.3.2 , *in vivo*. These are chemically reactive molecules containing oxygen. They also have the ability to displace other metal ions, peroxidise lipids and directly cleave DNA and RNA. In many types of cancers such as prostate, breast, colon, lung and brain cancer there have been reports of elevated levels of copper.[20]

There are at least two possible mechanisms in which the copper(II) complexes can generate hydroxyl radicals (an example of a ROS), namely the Fenton and Harber-Weiss mechanisms. In the Fenton mechanism Copper(II) is reduced to Copper(I), usually by ascorbate, which is a naturally occurring thiol ($HS\text{-}R\text{-}S^-$). The copper(I) then reacts with hydrogen peroxide *via* a redox reaction to produce hydroxyl radicals.[20] The following reaction scheme illustrates the hydroxyl radical formation:

$$HS\text{-}R\text{-}S^- + Cu^{2+} \rightarrow HS\text{-}R\text{-}S^{\cdot} + Cu^+$$

$$HS\text{-}R\text{-}S^{\cdot} + O_2 \rightarrow S\text{-}S\text{-}R + H^+ + O_2^{-\cdot}$$

$$2O_2^{-\cdot} + 2H^+ \rightarrow H_2O_2 + O_2$$

$$Cu^+ + H_2O_2 \rightarrow OH^{\cdot} + OH^- + Cu^{2+}$$

$$OH^{\cdot} + DNA \rightarrow Fragments$$

Scheme 1: The reaction equations for the formation of hydroxyl radicals for DNA degradation catalysed by copper(II).

In the Haber-Weiss mechanism copper(I) reacts with singlet dioxygen to form copper(II) and a superoxide anion which further reacts with hydrogen peroxide to form hydroxyl radicals.[20] Hydrogen peroxide is generated in living organisms due to the existence of certain enzymes. A copper(II)/(I) redox process will lead to the formation of the superoxide ion from dioxygen. The superoxide can then form the dioxygen and hydrogen peroxide.[20]

The following pathway in Figure 1.3.2 illustrates the sequential events for DNA cleavage (which is the key attribute of copper(II) chemistry which renders the complexes cytotoxic) performed by the copper chelates in the presence of ascorbate ($2H_2asc$). Ascorbate is one of the more commonly used reducing agents which is a naturally occurring thiol.[21]

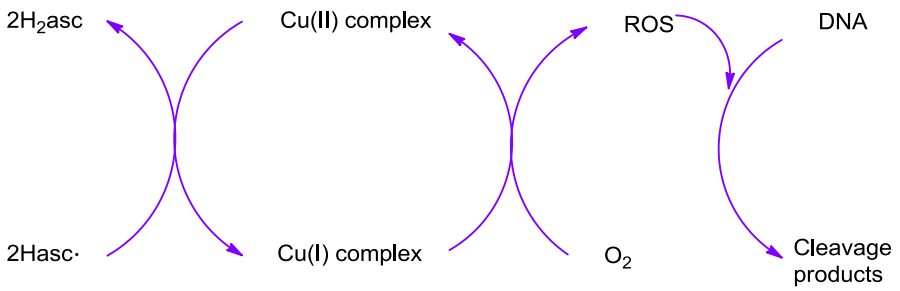

Figure 1.3.2: Formation of reactive oxygen species by copper(II) complexes in the presence of ascorbate (H_2asc) leading to DNA cleavage and tumour cell apoptosis.[21]

The highly reactive hydroxyl radical is able to interact with any biological molecule by taking the hydrogen from an amino bearing carbon to form a carbon-centred protein radical or from an unsaturated fatty acid to form a lipid radical. The electron deficient hydroxyl radicals can induce both single and double-stranded cleavage of the electron-rich DNA helix. The latter is particularly difficult for cellular regulatory systems to repair and is therefore an efficient method to control tumour cell growth.[21]

Previous work in the Akerman Research group has shown that copper(II) chelates can be effective chemotherapeutic agents. Shown below in Figure 1.3.3 are the structures of some of the chelates that the group has previously synthesised and screened against human tumour cell lines.

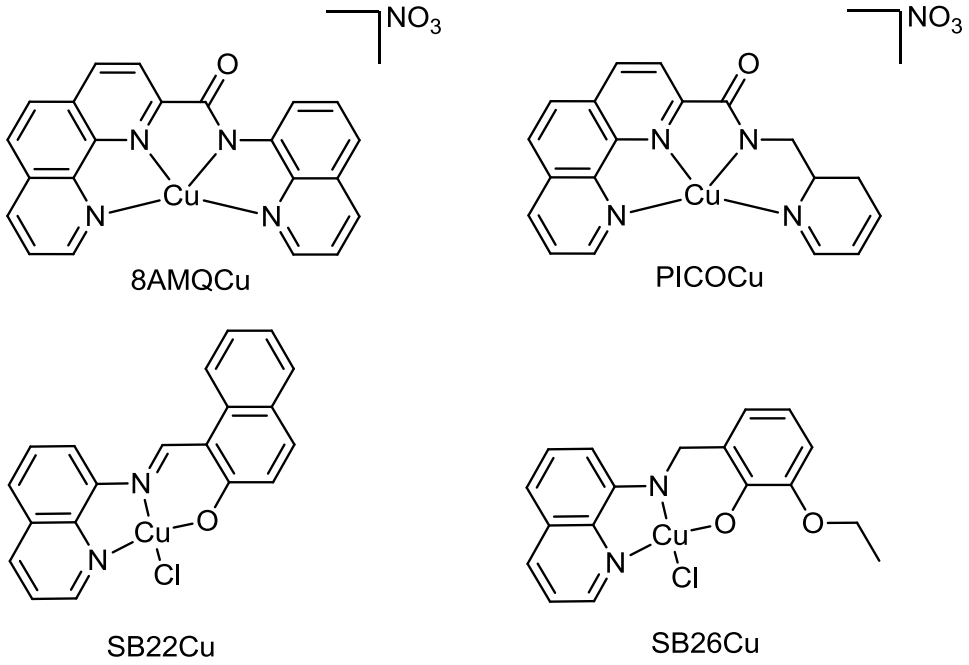

Figure 1.3.3: Previously synthesised Cu(II)-based chemotherapeutic agents.

These compounds have proven to be effective against a range of human tumour cell lines as shown in Table 1.3.1. It is interesting to note that the free ligands exhibited significantly less cytotoxicity towards the same tumour cell lines (IC_{50} > 100 μM). This difference in activity illustrates the importance of the copper(II) ion in the mechanism of action. The increased cytotoxicity was attributed to the copper(II) chelate's ability to catalyse the production of hydroxyl radicals *in vitro*. These radicals induce single and double-stranded DNA cleavage which would induce cell apoptosis. The ability of the above chelates to produce hydroxyl radicals in the presence of hydrogen peroxide was illustrated using a hydroxyl radical assay, during which the decay of rhodamine B by the electron deficient radicals was monitored spectroscopically as a function of time.

Table 1.3.1: IC_{50} values (μM) of various Cu(II) chelates against a range of human tumour cell lines.

Complex	A549[a]	HT-29[b]	U251[c]
8AMQCu	13.4 ± 2.7	21.0 ± 4.2	7.6 ± 1.0
PICOCu	26.04 ± 0.52	24.23 ± 1.14	11.02 ± 0.46
SB22Cu	7.65 ± 1.13	7.53 ± 2.55	5.28 ± 5.41
SB26Cu	21.46 ± 4.70	19.01 ± 2.52	10.77 ± 1.38

[a]Non-small cell lung tumor cell line.
[b]Human colon adenocarcinoma tumor cell line.
[c]Central nervous system tumor cell line.

Transition metal complexes may seem an odd choice for DNA molecular recognition agents. This is because, with few exceptions, biological transition metals are confined to coordination sites in proteins or cofactors, not in discrete, freestanding coordination complexes. Cells also generally employ organic moieties for the binding and recognition of DNA. Transition metal complexes, however, offer two singular advantages. Firstly, coordination complexes offer a uniquely modular system. The metal centre acts in essence as an anchor, holding in place a rigid, three-dimensional arrangement of ligands that can bear specific recognition elements. DNA-binding and recognition properties can thus be varied relatively easily with the facile interchange of ligands. Secondly, transition metal centres benefit from rich photophysical and electrochemical properties, thus extending their utility far beyond that of passive intercalation. In this case, the redox activity of the copper(II) centre is a critical aspect of the chemotherapeutic agent's design.[22]

Nuclease is an enzyme which has the ability to cleave the phosphodiester bonds between the nucleotide subunits of nucleic acids.[21] Extensive research has been done using transition metal complexes as artificial nucleases due to the reactivity and wide range of structural features of these complexes. Copper(II) complexes make efficient chemical nucleases because of their high affinity towards neucleobases as well as their biologically accessible redox potential. They intercalate efficiently with DNA base pairs and show considerable nuclease activity.[22] The above discussion clearly shows the potential of Cu(II) for the synthesis of novel chemotherapeutic agents and reaffirms the choice of metal ion for this project.

1.4 Positron Emission Tomography

X-ray, computed tomography (CT) and magnetic resonance imaging (MRI) are medical imaging techniques utilised for the visualisation of anatomical structures. In the diagnosis of certain diseases it is more useful to acquire images of physiological functions rather than of anatomical structures.[23] Imaging the decay of radioisotopes bound to molecules with known biological properties makes acquiring such images possible. These imaging techniques are more well known in nuclear medicine as positron emission tomography (PET).[24] Figure 1.4.1 highlights the production of the gamma rays used in PET imaging. PET is an imaging technique in which a computer-generated image of a radioactive tracer distributed in tissue is produced through the detection of annihilation photons. These photons are emitted when radionuclides are introduced into the body, decay and release positrons.[25]

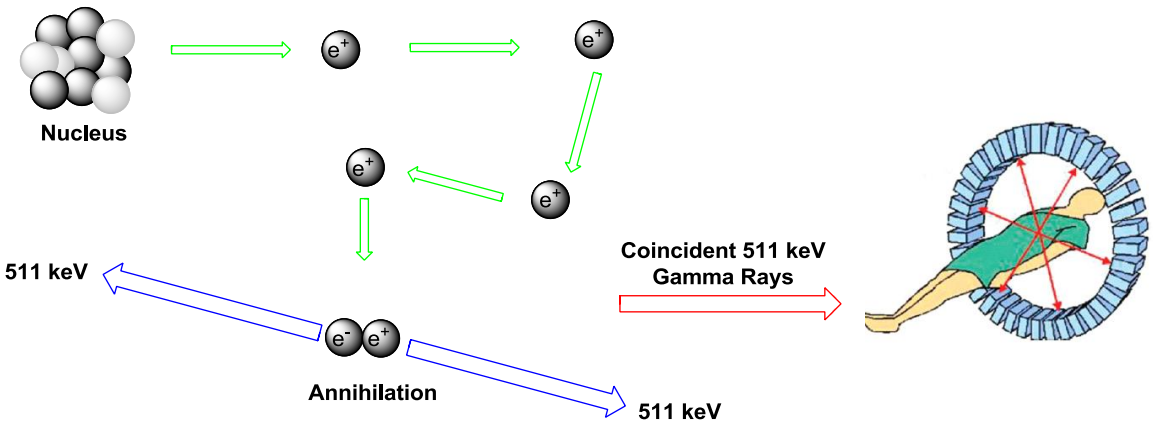

Figure 1.4.1: Tumour imaging with positron emission tomography (PET).[25]

PET is a favourably sensitive, non-invasive imaging technique that is well suited for pre-clinical and clinical imaging of cancerous regions in the body. The imaging of target molecules which are associated with cancer allows for earlier diagnosis and better management of oncology patients.[23] With recent advances in targeted drug therapy, it is now possible to design specific compounds to image diseased tissue in humans. PET is mostly used for the monitoring of cellular events in the course of a disease and during radiation or pharmacological therapy.[26]

In the past, the availability of PET had been limited to the use of cyclotron-produced isotopes such as fluorine-18. However, the high costs of maintaining and establishing cyclotron facilities has led to generator based isotopes such as gallium-68 which is a key isotope. Gallium-68 has a half-life of 68.3 minutes and β^+ = 1.89 MeV. These decay properties allowed departments with standard radiopharmaceutical equipment to make use of this advanced imaging technique. ^{68}Ga-DOTATATE, ^{68}Ga-DOTATOC and ^{68}Ga-DOTANOC, shown in Figure 1.4.2 , have been introduced into clinical practice.[27]

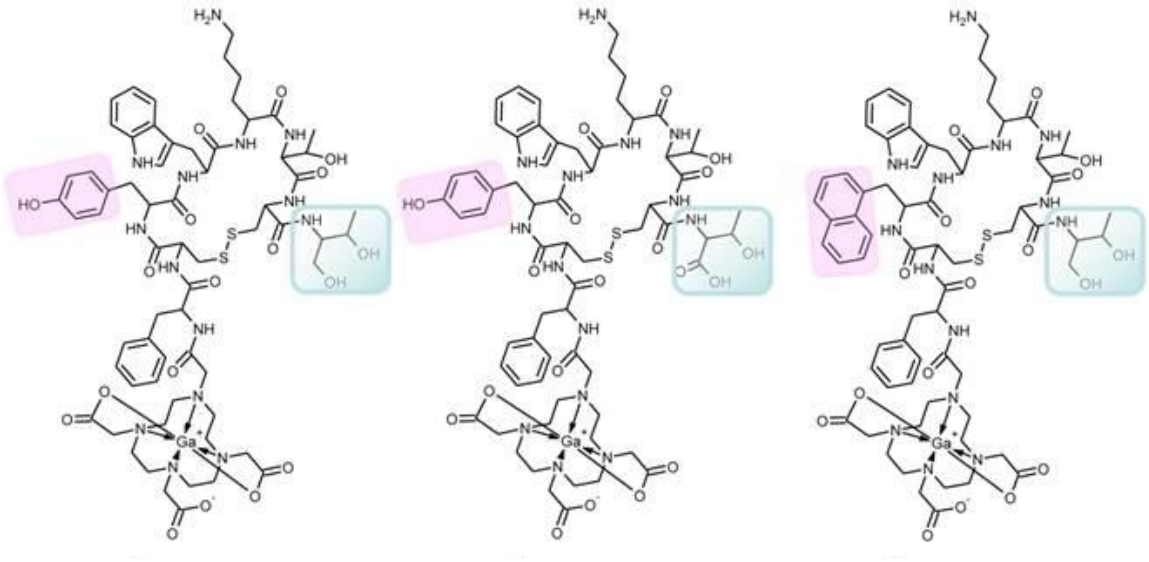

Figure 1.4.2: Chemical structures of (a) ^{68}Ga-DOTATOC, (b) ^{68}Ga-DOTATATE, (c) ^{68}Ga-DOTANOC. The highlighted substituents show where the variations between the three chelates lie. Image reproduced from Velikyan *et al*.[28]

The research and development of metal-based radiopharmaceuticals represents a dynamic and fast growing research area which requires a good understanding of ligand design and metal coordination chemistry.[23]

^{64}Cu ($t_{1/2}$ = 12.7 h; β^+ 0.653 MeV, (17.8 %), β^- 0.579 MeV (38.4%)) has drawn considerable interest in PET research owing to its commercial availability, short positron range, and reasonably long half-life.[29] The 12.7 hour half-life of ^{64}Cu provides the flexibility to image both small and large tumours. Due to the versatility of ^{64}Cu there has been an abundance of novel research, primarily in the area of PET imaging.[10]

Copper also has well-established coordination chemistry and a wide variety of chelator systems that can be linked to antibodies, proteins, peptides, and other biologically relevant molecules. These groups can help to increase the specificity of the copper chelates for tumour cells and improve their potential as PET imaging agents. ^{64}Cu(II) has to be bound to a thermodynamically stable and kinetically inert ligand, which requires tracer molecules, for example antibodies, to be equipped with a suitable chelating moiety.[26] By using radiolabelled tracers such as ^{64}Cu chelates with cell targeting groups which will lead to increased concentration in the tissue of interest, a series of three-dimensional images can be reconstructed to show the size and location of a tumour. The concept of targeted drug/imaging agent delivery is shown in Figure 1.4.3.

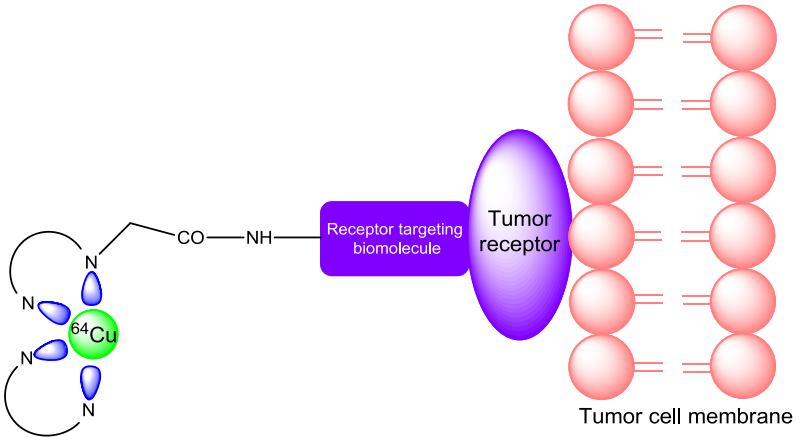

Figure 1.4.3: ^{64}Cu chelate with receptor biomolecule attaching to a tumour receptor.[24]

A recent study by Lux *et al.* reported the successful creation of the first metal-chelating nanogel imaging agent which incorporated ^{64}Cu to be used as a PET radiotracer. Polyacrylamide-based (PAA) nanogels were crosslinked with a range of different polydentate ligands. PAA was selected as the nanogel backbone because it is stable and non-toxic. Experiments in mouse serum indicated that NOTA-based (1,4,7-triazacyclononane-triacetic acid) nanogels retained ^{64}Cu most stably and were therefore, used along with DOTA-based (1,4,7,10-tetraazacyclododecane-1,4,7,10-tetraacetic acid) nanogels for *in vivo* PET imaging of tumour-bearing mice. Figure 1.4.4 shows the ^{64}Cu-chelated DOTA (PAA/2) and NOTA (PAA/3) nanogels which were injected into mice containing subcutaneous 4T1 murine mammary carcinoma tumours.[30]

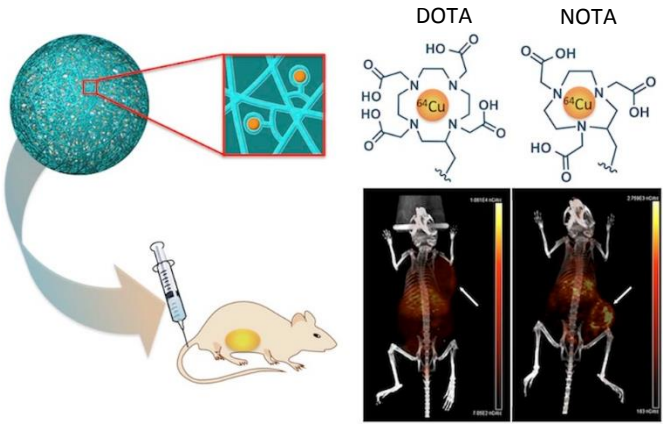

Figure 1.4.4: ^{64}Cu-chelated DOTA and NOTA nanogels injected into mice with resulting PET images. Image reproduced from Lux *et al.*[30]

A closer look at the PET images in Figure 1.4.5 show that after four hours, accumulation of PAA/3(^{64}Cu) was visible in the liver, heart and neck blood vessels, while a moderate amount of signal was visualised in the tumour. PAA/2(^{64}Cu) showed a similar pattern of uptake at four hours, but with a higher accumulation in the liver. Over the next 24 - 48 hours the uptake of PAA/3(^{64}Cu) continued to increase. PAA/2(^{64}Cu) showed similar trends, however, the overall uptake was lower than PAA/3(^{64}Cu) after 24 and 48 hours.[30] Free copper has the ability to be taken up by tumours *via* copper transporters. The study by Lux *et al.* also compared the tumour uptake of PAA/2(^{64}Cu) and PAA/3(^{64}Cu) to that of ^{64}Cu-acetate. The free copper within tumours remained steady throughout the experiment. The higher stability of the NOTA-based nanogels was confirmed by the greater uptake of PAA/3(^{64}Cu) than PAA/2(^{64}Cu).[30]

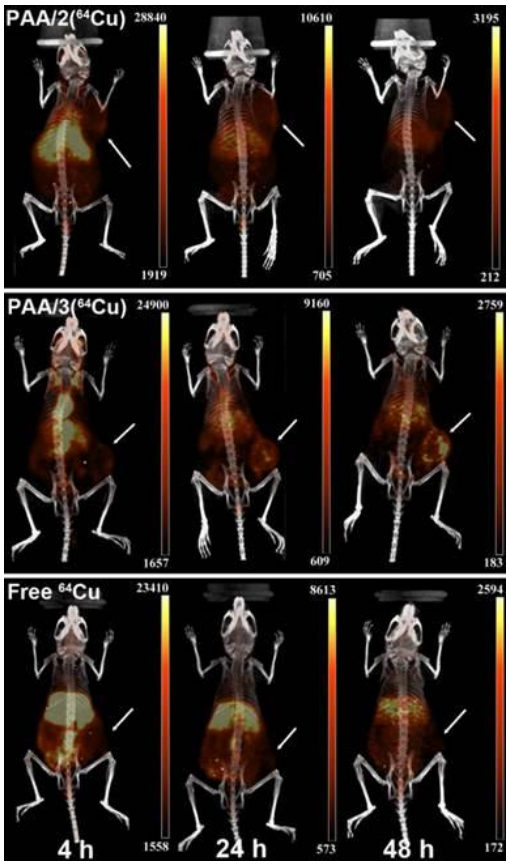

Figure 1.4.5: PET images comparing uptake of PAA/2(^{64}Cu) and PAA/3(^{64}Cu) nanogels to free ^{64}Cu in mice containing subcutaneous 4T1 murine mammary carcinoma tumours. Image reproduced from Lux *et al*.[30]

1.5 Targeted Drug Delivery

Taking into consideration the severe side effects of current cancer treatment, noting Cisplatin as an example, the main motive that continues to fuel cancer research is to improve therapeutic efficacy reducing the side-effects of treatment. Tumour cell-targeting systems have shown encouraging results in improving therapeutic efficiency.[31] Target-specific delivery can be achieved by adding a suitable targeting moiety to the complex. Many tumour cells over-express receptor sites for certain growth factors. By targeting these receptor sites the uptake of radiopharmaceuticals labelled with either ^{68}Ga or ^{64}Cu in neoplastic versus healthy tissue can be greatly enhanced.[31]

Cell-targeting moieties currently in use include peptides, vitamins, antibodies, folic acid and integrin. Vitamin H, more commonly known as biotin, has been used as a suitable targeting agent in recent research.[32] Biotin is a growth promoter and cancerous cells require biotin to sustain their rapid growth.[32] The over expression of biotin receptors on the surface of cancerous cells make these targeted drug delivery systems an efficient method for the treatment of tumors.[33] Previously, there has been poor overlap between the prevention, diagnosis and treatment of cancer which hindered efforts to effectively treat cancer. Current research is therefore aimed at developing a new treatment method that combines diagnosis and therapy.[32] The combination of cell targeting groups with chemotherapeutics and isotopes suitable for PET imaging is therefore a very attractive area of research.

Paclitaxel also known as Taxol, shown in Figure 1.5.1, is an effective chemotherapeutic used in the treatment of a wide range of cancers; however, the therapeutic effects of this drug are limited due to the lack of selectivity towards cancer cells and poor aqueous solubility. A recent study by Heo, *et al.* investigated the use of gold nanoparticles as a drug delivery system for paclitaxel; this improved the water solubility and selectivity towards cancer cells. Beta-cyclodextrin (a ring shaped structure with a hydrophobic inner cavity and a hydrophilic outer cavity) has also been successfully used to improve paclitaxel's aqueous solubility.[32] The study was designed to evaluate the effectiveness of diagnosis and treatment of three cancer cell lines using biotin-tagged gold nanoparticles as a drug delivery system for paclitaxel. The cancer cell lines tested were human lung (A549) carcinoma, human breast (HeLa) and human osteosarcoma (MG63). The impact on normal cells was determined by modified nanoparticles and compared to human fibroblast (NIH3T3) cell lines.[32]

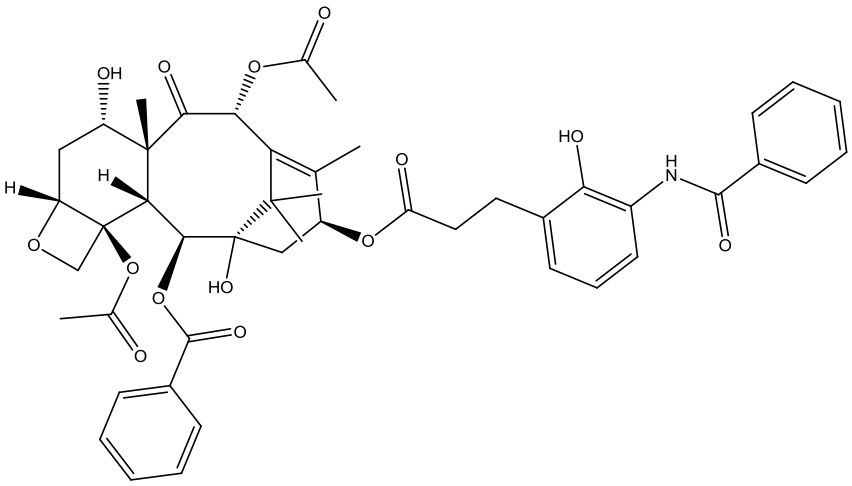

Figure 1.5.1: Chemical structure of Paclitaxel, more commonly known as Taxol. A highly cytotoxic compound whose application in chemotherapy has been improved by the addition of cell-targeting gold nanoparticles.

The intracellular uptake and cytotoxicity against the three cell lines was investigated. Dark-field microscopy analysis showed that the surface-modified gold particles had been taken into the cytoplasm of the cancer cell lines by biotin-receptor mediated endocytosis thus confirming that the biotin ligand can be used as a biomarker for cancer cell-targeted therapy. Evaluation of the nanoparticles anti-cancer effect *in vitro* showed paclitaxel has strong cytotoxic effects in both HeLa and NIH3T3 cells. It was noted that the mortality rate of HeLa cancer cells using the gold nanoparticles increased five-fold. These results confirm that gold nanoparticles surface-functionalised with a chemotherapeutic agent and biotin can be utilised as a carrier for targeted drug delivery, lessening the cytotoxic effects on healthy cells.[32]

By incorporating a cellular targeting moiety such as biotin into a ligand system coordinated to a radionuclide, the relative uptake of the ^{64}Cu complex in cancerous tissue compared to healthy cells can be enhanced allowing for both diagnosis and therapy. This would be regarded as a "theranostic" agent, one in which a combination of diagnostic and therapeutic capabilities exist in a single agent.[34]

1.6 Biological Activity of *N,N',O*-Tridentate Schiff Base Ligands

Schiff bases are one of the most widely used organic compounds in coordination chemistry finding application in the analytical, dye, food and catalysis industries.[35] They have also shown agrochemical, fungicidal and biological activities.[35] The C=N linkage in Schiff base derivatives has proven to be vital for biological activity.[35]

The chemotherapeutic properties of *N,N',O*-donor Schiff base complexes with various metals have been a topic of investigation in recent years.[36] In particular, copper(II) Schiff base complexes have shown encouraging results in anticancer research. This class of copper(II) complexes have the ability to catalytically cleave DNA and show promising cytotoxicity towards certain cancer cell lines. One such study investigated the DNA cleavage, DNA binding and cytotoxicity of the copper(II) *N,N',O* Schiff base complex, $[Cu^{II}(5\text{-Cl-pap})(OAc)(H_2O)]\cdot 2H_2O$, depicted in Figure 1.6.1.[36]

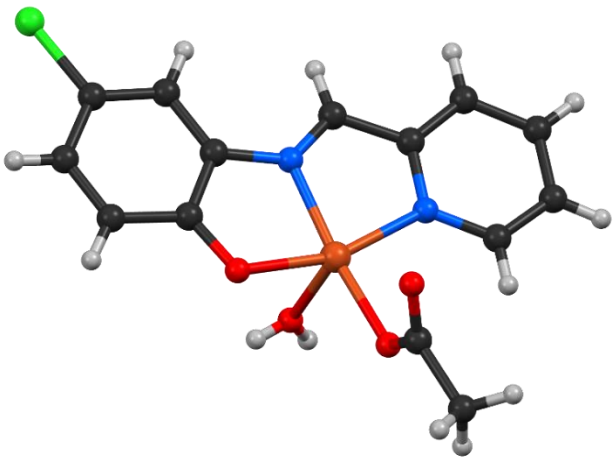

Figure 1.6.1: Structure of $[Cu^{II}(5\text{-Cl-pap})(OAc)(H_2O)]\cdot 2H_2O$ a cytotoxic copper(II)-based chemotherapeutic.[36]

The potential binding ability of $[Cu^{II}(5\text{-Cl-pap})(OAc)(H_2O)]\cdot 2H_2O$ to calf thymus DNA was measured by UV spectroscopy and confirmed DNA interactions. A strong apparent binding constant was calculated thus showing the potential of this class of copper(II) Schiff base chelates as chemotherapeutic agents.

It was also confirmed that the complex promoted DNA cleavage. Hydrogen peroxide, singlet oxygen-like species and hydroxyl radicals were determined to be the active species involved in the DNA cleavage process. High *in vitro* cytotoxic properties against human cervical carcinoma cells (HeLa) was also observed. An IC_{50} = 16.123 ± 1.207 µM was measured confirming that this complex deserves further investigation as a possible chemotherapeutic drug. These data show the chelate to have a greater cytotoxicity against these specific tumour cell lines than the industry standard metallodrug cisplatin.[36]

The induction of cell apoptosis and cytotoxicity of a copper(II) *N,N',O* Schiff base complex, [CuII(ClQP)(NO_3)(H_2O)], shown in Figure 1.6.2, has also been studied. The cytotoxicity of [CuII(ClQP)(NO_3)(H_2O)] was determined against the human tumour cell lines BEL-7404, HepG2,

NCI-H460, MGC80-3 and the normal liver cell line HL-7702. The quinoline-based Schiff base complex is shown to be five coordinate with the *N,N',O* tridentate ligand, one monodentate nitrate anion and a single H_2O ligand.[37]

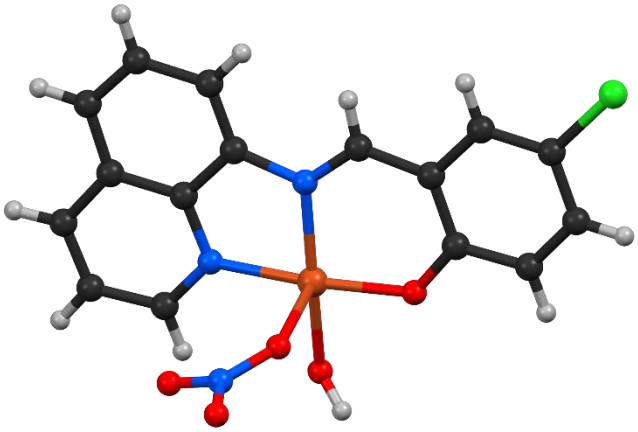

Figure 1.6.2: Structure of complex [CuII(ClQP)(NO_3)(H_2O)] a copper(II)-based chemotherapeutic agent.[37]

Table 1.6.1 shows that [CuII(ClQP)(NO_3)(H_2O)] displays promising growth inhibition properties against four cancer cell lines with IC_{50} values ranging from 6.5 to 23.6 µM. The highest sensitivity was observed against the cancer cell line HepG2. It is interesting to note that the complex did not show any cytotoxicity towards the normal cell line, possibly suggesting that the complex is selective towards cancer cells. This study reaffirms the potential applications for this class of complex as antitumor agents.[37]

Table 1.6.1: IC_{50} values against four cancer cell lines and one normal human liver cell line for [CuII(ClQP)(NO_3)(H_2O)] compared with Cisplatin.[31]

Compound	IC_{50} (µM)				
	HepG2	**NCI-H460**	**MGC80-3**	**BEL-7404**	**HL-7702**
[CuII(ClQP)(NO_3)(H_2O)]	6.5 ± 0.3	23.6 ± 0.2	10.7 ± 0.3	9.8 ± 0.2	>100
Cisplatin	8.3 ± 0.7	5.3 ± 0.4	>100	98.0 ± 17.4	80.6 ± 0.2

1.7 Heteroleptic Copper(II) Complexes

Heteroleptic complexes or mixed ligand complexes consist of transition metals with more than one type of ligand bound to the metal centre. This class of metal chelates has garnered considerable attention due to their wide range of applications in environmental, industrial and medicinal research.[38] The effect of one ligand on the co-ligand through the central metal atom in heteroleptic complexes has proven to be very important in coordination chemistry.[38] The

interactions between the two co-ligands can be observed in thermodynamic and kinetic aspects of chemical reactivity. In particular, copper(II) complexes with Schiff base ligands have shown increased bioactivity in the presence of bidentate nitrogen-donor heterocyclic ligands such as 1,10-phenanthroline (phen) and 2,2-bipyridyl (bpy). Several studies have investigated the versatile DNA cleavage capabilities, cytotoxicity and antioxidant activity of heteroleptic copper(II) Schiff base complexes.[38]

The antioxidant and DNA binding affinities were determined for a range of eight heteroleptic Schiff base complexes with phen and bpy as co-ligands.[39] The most biologically active complex $[CuL^2(phen)](ClO_4)_2$, shown in Figure 1.7.1, contained a hydrophobic methyl substituent. This is an interesting result as it has been shown in other studies that the lipophilicity of metal chelates, particularly those that exert their cytotoxicity through DNA binding, is a critical physico-chemical predictor for chemotherapeutic activity.[40] The antioxidant activity of $[CuL^2(phen)](ClO_4)_2$ against DPPH, which is a stable radical used for studying radical scavenging activity, showed antioxidant activity very similar to the industry standard antioxidant, vitamin C.[38]

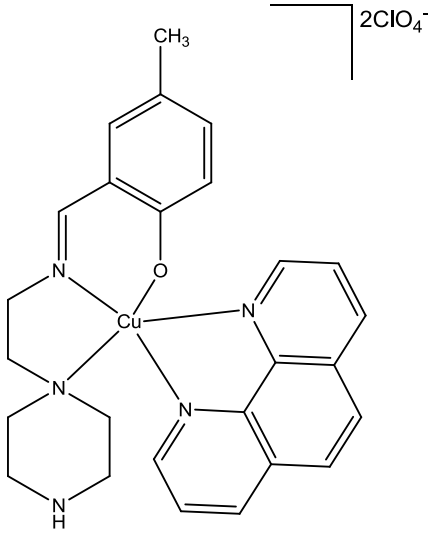

Figure 1.7.1: Heteroleptic complex $[CuL^2(phen)](ClO_4)_2$ which has shown antioxidant properties.[32]

DNA binding studies have showed the metal complex binds with nucleic acids through covalent and/or non-covalent interactions. Non-covalent interactions are most prevalent with heteroleptic complexes and can occur as electrostatic interactions, intercalation and groove (major or minor) binding. $[CuL^2(phen)](ClO_4)_2$ had a DNA binding constant of 3.63×10^4 M^{-1}. Due to the hydrophobic interactions of the methyl group with the hydrophobic DNA surface, the above complex showed higher binding affinity than complexes with other substituents.[38]

It has similarly been shown that an *N,N′,N″* tridentate, heteroleptic complex $[Cu(L1)(2,9\text{-dmp})](ClO_4)_2$, shown in Figure 1.7.2, exhibits favourable affinity towards calf thymus DNA as well as cytotoxic activity against MCF-7 breast cancer cells lines. The *N,N′,N″* ligand diethylenetriamine is expected to show various DNA binding interactions while the co-ligand 2,9-dimethyl-1,10-phenanthroline has been reported to be a copper dependant cytotoxic agent in *in vivo* studies against p388 murine lymphoma.[39]

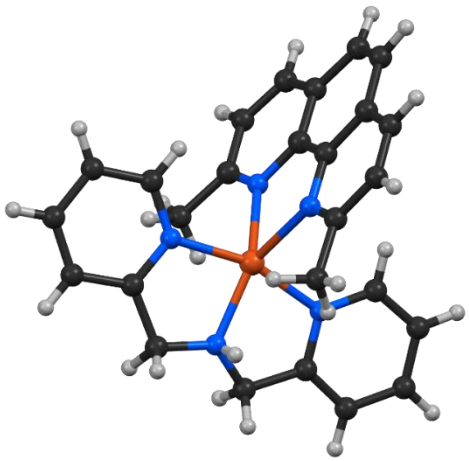

Figure 1.7.2: Structure of the tridentate, heteroleptic complex $[Cu(L1)(2,9\text{-dmp})](ClO_4)_2$ with 2,9-dimethyl-1,10-phenanthroline.[32]

$[Cu(L1)(2,9\text{-dmp})](ClO_4)_2$ has a DNA binding constant of $2.1 \times 10^4\ M^{-1}$ due to partitial insertion of the complex between DNA base pairs. It was proposed that $[Cu(L1)(2,9\text{-dmp})](ClO_4)_2$ had a higher binding constant compared to the other complexes in the study due to reduced steric hinderance of the primary ligand. Furthermore, strong hydrogen bonding of the NH_2 and NH groups of diethylenetriamine with phosphate groups or nucleobases of the DNA could stabilise the DNA/drug conjugate and contribute to the higher binding constant.[39]

Cell screening studies were carried out against MCF-7 breast cancer cell lines and a comparative study against the ubiquitous cisplatin was conducted. The complex $[Cu(L1)(2,9\text{-dmp})](ClO_4)_2$ had an IC_{50} value of 16.7 ± 1.5 µM after 24 hours and 11.3 ± 1.1 µM after 48 hours showing higher cytotoxicity than cisplatin. The enhanced hydrophobicity of the complex due to the co-ligand seemingly aids in the transport of the complex through cell membranes which leads to efficient apoptosis of the cells.[39]

1.8 DNA Binding Modes

As the primary pharmacological target of many antitumor drugs is DNA, DNA binding affinities of metal complexes are of paramount importance for the development of effective metallodrugs.[36] There exist a number of commonly encountered binding modes. Molecules can bind covalently to the DNA bases, as with cisplatin. Molecules also have the ability to bind to the sugar-phosphate backbone of DNA. Metalloinsertors contain an aromatic planar ligand which extends into the base stack upon DNA binding and ejects the bases of a single base-pair. The planar ligand of the chelate acts as π-stacking replacement in the DNA base stack. DNA intercalators are another DNA binding agent, which partially unwind the DNA and π-stack between two base pairs. Groove binding occurs when molecules bind into the major or minor grooves of the DNA by hydrophobic interactions or by partial intercalation.[22]

The three main DNA binding modes of metal chelates are groove binding, intercalation and insertion. All three binding modes are illustrated in Figure 1.8.1.

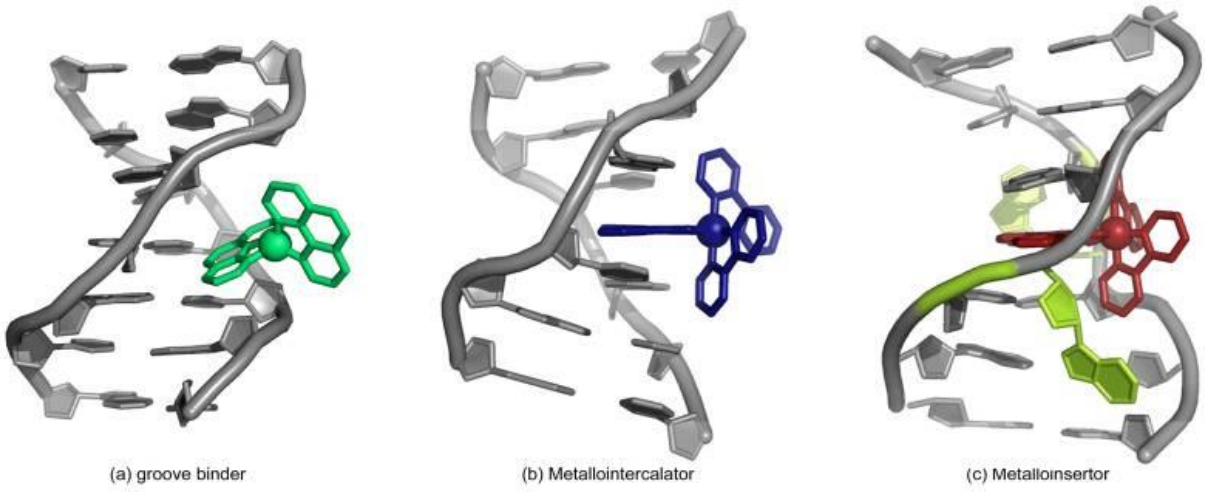

Figure 1.8.1: Illustration of DNA binding modes: insertion, intercalation and groove binding.[22]

The study of the interactions between transition metal complexes and DNA is a field that is still under investigation. Research on DNA cleavers is important since they can be used as chemotherapeutic agents and DNA structural probes.[38] In most cases DNA binding is a key step for DNA cleavage, highlighting the significance of research in this field.

DNA intercalators are usually small metal complexes or organic molecules which partially unwind the DNA helix. Metallointercalators are small metal chelates with at least one intercalating ligand. These ligands are positioned parallel to the base pairs and protrude away from the metal centre and can readily stack in the DNA helix. They enter the double helix via the major groove, with the intercalating ligand acting as a new base pair. This binding mode leads to minimal distortion of the tertiary structure of the DNA and is illustrated in Figure 1.8.2.[22]

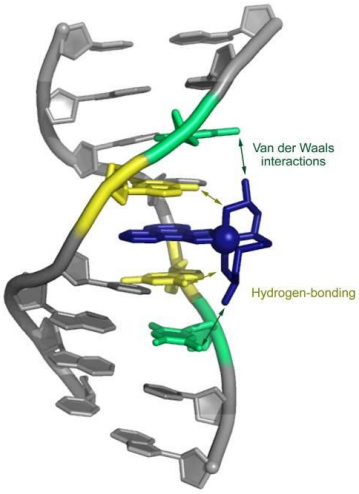

Figure 1.8.2: Crystal structure of a rhenium-based metallointercalator showing Van der Waals and hydrogen interactions.

Copper(II) complexes in particular interact with DNA *via* covalent bonding, electrostatic interaction, hydrogen bonding with ligands, intercalation and groove binding.[41] Copper(II) complexes have been known to bind and cleave double-stranded DNA with high reactivity and structural selectivity. Interactions of smaller compounds in the minor groove of DNA is different from those occurring in the major groove. This is due to steric hindrance and electrostatic potential due to the minor groove binder's narrow shape.[41]

Groove binding is an intermolecular interaction between the complex and DNA helix which does not alter the DNA structure in any way and to a large extent the structure of the metal compounds will determine whether the complex will favour the minor or major groove.

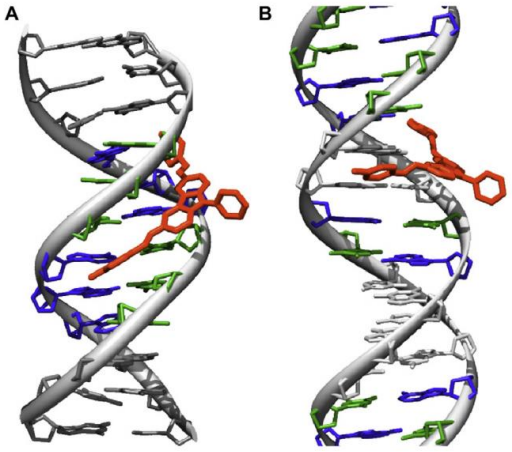

Figure 1.8.3: (A) A molecule docked into the minor groove and (B) into the major groove of the DNA helix.[42]

Copper(II) phenanthroline complexes are one of the most studied copper complexes in terms of biological activity.[43] Numerous studies on this class of complex suggest they non-covalently bind to the minor groove of double-stranded DNA. An example of a heteroleptic copper complex, $[CuL_2(phen)]$ with a phenanthroline co-ligand, which favours groove binding, is shown in Figure 1.8.2.[43]

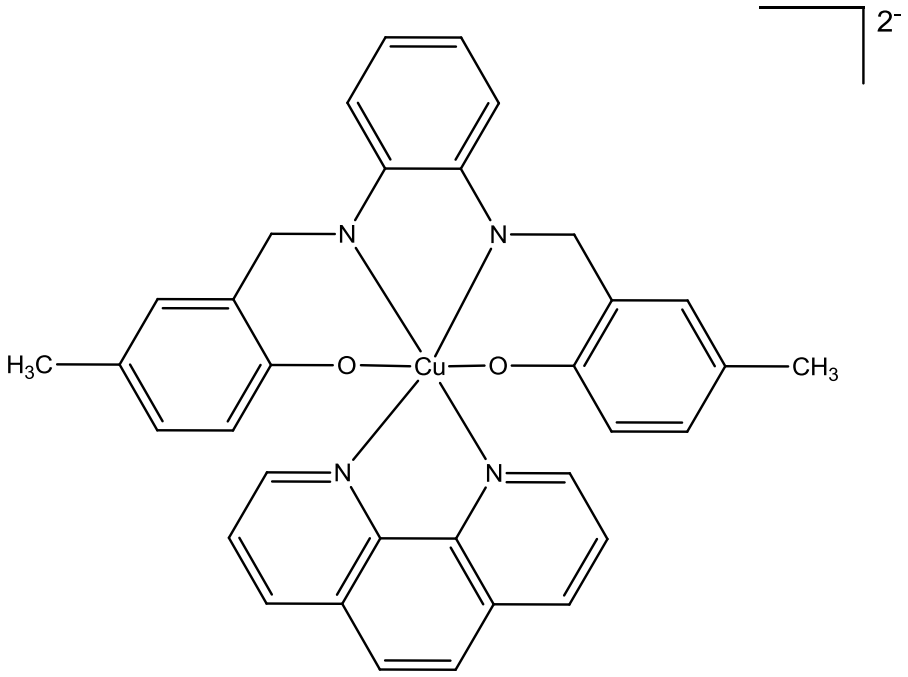

Figure 1.8.4: Structure of $[CuL_2(phen)]$: a known DNA groove binder.[35]

A less pronounced bathochromic shift in the UV absorption titration experiments of the above complex suggested the possibility of groove binding. Further studies to confirm the predicted binding mode were carried out using viscosity titrations. These titrations not only elucidate the binding mode, but also determine the affinity of the complex for calf-thymus DNA.

Intercalation involves the DNA double helix being "stretched out" to accommodate the binding ligands in between base pairs and results in an increase in viscosity. Partial intercalation results in the DNA bending thus shortening the helix and resulting in a reduced viscosity. Groove binding is confirmed by little to no change in the viscosity of the solutions since minimal changes occur to the double-stranded DNA helix. Viscosity measurements showed very slight changes suggesting partial intercalation and predominantly minor groove binding.[43]

1.9 Objectives

The aim of this project is to synthesise a series of single-ligand and heteroleptic copper(II) Schiff base chelates which are anticipated to be chemotherapeutic agents. Both *N,N',O* and *N,N',N''* Schiff base ligands were synthesised to investigate any variation in bioactivity. The addition of a co-ligand to the above mentioned complexes is used to investigate whether the heteroleptic copper(II) chelates show increased bioactivity compared to the single-ligand copper(II) chelates.

The following objectives for the project have been identified from the literature review:

The project will commence with the synthesis of the primary Schiff base ligands depicted in Figure 1.9.1. The ligands (where possible) will be characterised by ^{1}H and ^{13}C NMR experiments, FT-IR spectroscopy and mass spectrometry.

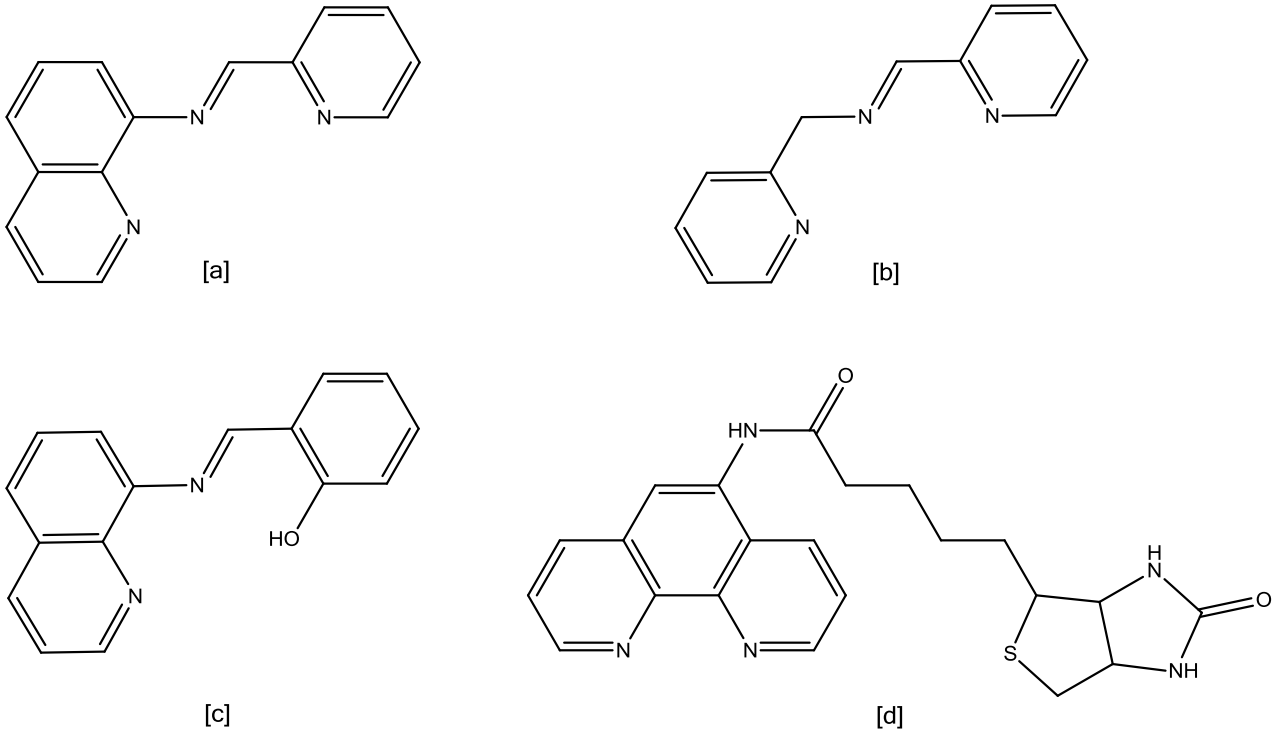

Figure 1.9.1: Proposed ligands to be chelated to copper(II) in this study.

Once the Schiff base ligands have been successfully synthesised and characterised, they will be coordinated to copper(II). The metal chelates will be characterised by UV/visible and FT-IR spectroscopy, mass spectrometry and, where possible, X-ray crystallography.

The copper(II) complex of the *N,N',O* Schiff base ligand will be further reacted with various co-ligands to form a range of heteroleptic complexes. The co-ligands used in the synthesis of the heteroleptic complexes include 2,2'-Bipyridyl, 1,10-Phenanthroline, 5-amino-1,10-phenanthroline and Phen-biotin the latter is illustrated in Figure 1.9.1 [d] . The proposed heteroleptic copper(II) complexes are shown in Figure 1.9.2.

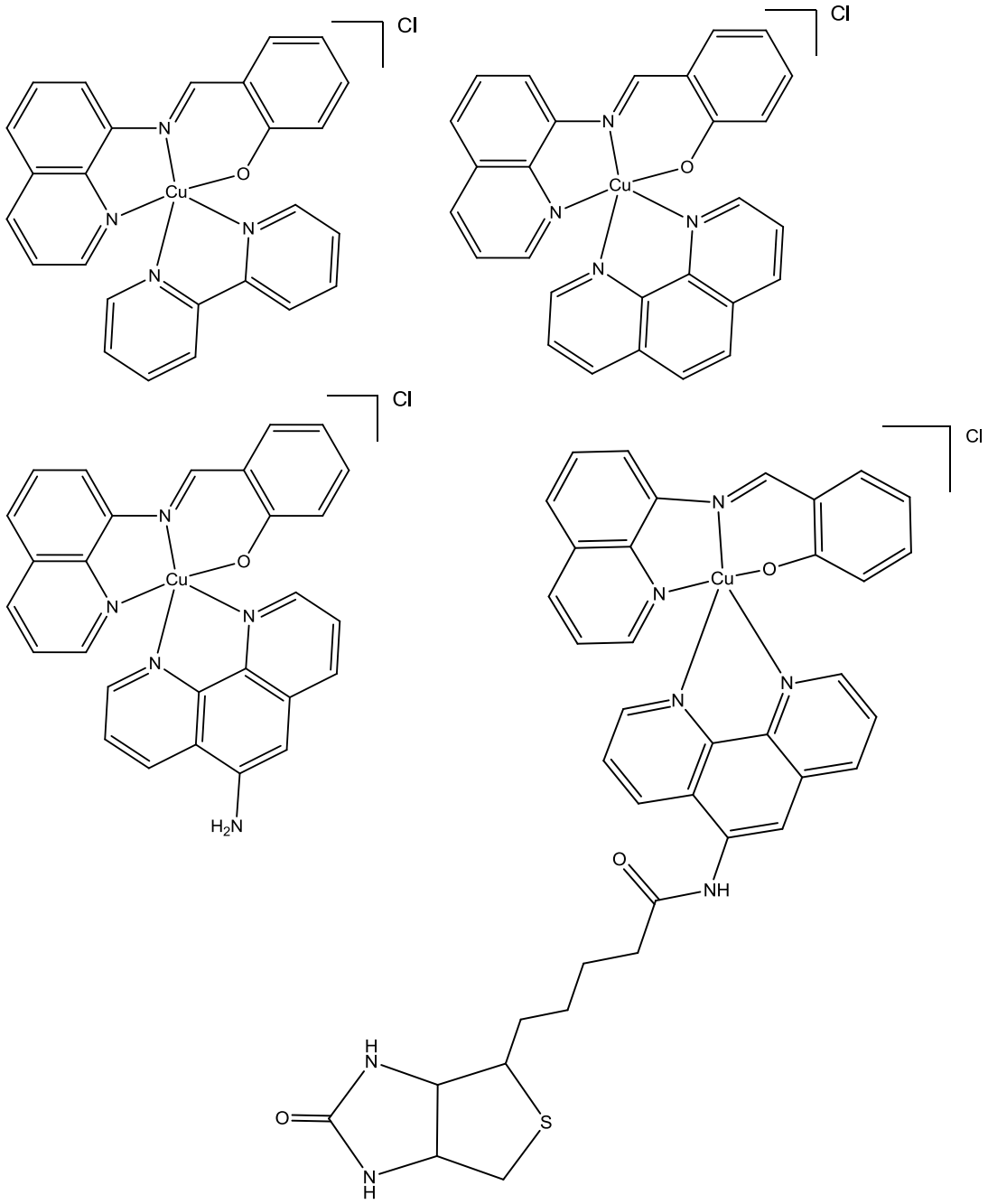

Figure 1.9.2: Proposed heteroleptic copper(II) complexes to be synthesised in this study.

Computational studies will be performed on all copper(II) metal chelates using Density Functional Theory. Comparisons will be drawn between the experimental and calculated data to expand the understanding of the experimental data.

The DNA binding affinities will be determined by a competitive titration with ethidium bromide. The cytotoxicity will be investigated by screening against a panel of four human tumour cell lines. The ability of the copper(II) complexes to catalyse the production of hydroxyl radicals will also be explored.

The anticipated outputs of this project include the synthesis of a range of anticancer agents. Incorporating biotin into the ligand design will allow for cell targeting potentially leading to an increase in the uptake of the metal chelates in neoplastic versus healthy cells. Radiolabelling the compounds with ^{64}Cu will have potential for PET imaging.

Chapter 2 | Experimental

2.1 General Methods and Instrumentation

All starting materials used in the syntheses were purchased from Sigma–Aldrich (Germany) and used as received. Organic solvents were purchased from Merck (South Africa) and were of analytical reagent (AR) grade. All solvents were dried using a Puresolv™ MD 7 purification system from Innovative Technologies prior to use. NMR spectra were recorded with a Bruker Avance III 400 MHz spectrometer equipped with a Bruker magnet (9.395 T) using a 5 mm TBIZ probe at frequencies of 400 MHz and 100 MHz for the ^{1}H and ^{13}C spectra, respectively. The spectra were recorded at 30 ^{0}C. All NMR experiments were conducted using Bruker Topspin 2.1, patch level 6. All proton and carbon chemical shifts are quoted relative to $CDCl_3$: ^{1}H, 7.26 ppm and ^{13}C, 77.16 ppm and DMSO-*d*6: ^{1}H, 2.50 ppm and ^{13}C, 39.52 ppm.

FTIR spectra were recorded using a Bruker Alpha FTIR spectrometer equipped with an ATR platinum Diamond 1 reflectance accessory. The machine acquired the information in 32 scans with a spectral resolution of 1.0 cm^{-1}. The abbreviations used in the text are as follows; br, broad; s, strong; m, medium and w, weak signals. Elemental analysis was carried out using a CHNS-O Flash 2000 Organic Elemental Analyser. Electronic spectra were recorded using a Shimadzu UVPC-1800 double beam UV–Vis scanning spectrometer (1.0 cm path length cuvette). Spectra were recorded from 800 to 200 nm. High resolution masses were determined with a Waters Acquity-LCT Premier coupled high performance liquid chromatograph–mass spectrometer (time-of-flight) using electrospray ionization in positive mode.

2.2 Synthesis of Ligands

2.2.1 Synthesis of 2-[(*E*)-(quinolin-8-ylimino)methyl]phenol (HL1)

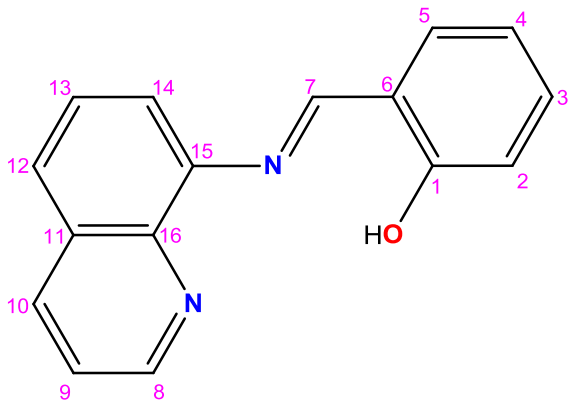

Figure 2.2.1: Structure of 2-[(*E*)-(quinolin-8-ylimino)methyl]phenol showing the atom numbering scheme.

HL1 was prepared by the condensation of salicylaldehyde with 8-aminoquinoline in ethanol. To a solution of 8-aminoquinoline (0.83 g, 5.78 mmol) in ethanol (30 mL) was added salicylaldehyde (0.61 mL, 5.78 mmol) and the solution heated to reflux for four hours. The solvent was removed from the orange reaction mixture under reduced pressure using rotary evaporation. The resulting orange oil was recrystallized from hexane to afford orange/red crystals. Yield (1.26 g, 87 %).

The following characterisation data were recorded:

^{1}H NMR (400 MHz, $CDCl_3$, 303K) [δ, ppm]: 13.93 (s, 1H, OH); 9.01 (dd, 1H, J_1 = 4.26 Hz, J_2 = 1.75 Hz, 8); 8.96 (s, 1H, 7); 8.21 (dd, 1H, J_1 = 8.26, J_2 = 1.72, 10); 7.74 (dd, 1H, J_1 = 8.18, J_2 = 1.27, 12); 7.33-7.62 (m, 5H, 3, 5, 9, 13, 14); 7.10 (d, 1H, 4); 6.97 (m, 1H, 2). **^{13}C NMR** (100 MHz, $CDCl_3$, 303 K) [δ, ppm]: 164.76 (C-1); 162.06 (C-7); 150.49 (C-15); 145.59 (C-8); 142.38 (C-16); 135.98 (C-10); 133.28 (C-3); 132.35 (C-5); 129.22 (C-11); 126.57 (C-13); 126.17 (C-14); 121.73 (C-12); 119.61 (C-6); 118.98 (C-9); 118.78 (C-4); 117.63 (C-2).

2.2.2 Synthesis of (*E*)-1-(pyridin-2-yl)-*N*-(quinolin-8-yl)methanimine (L2)

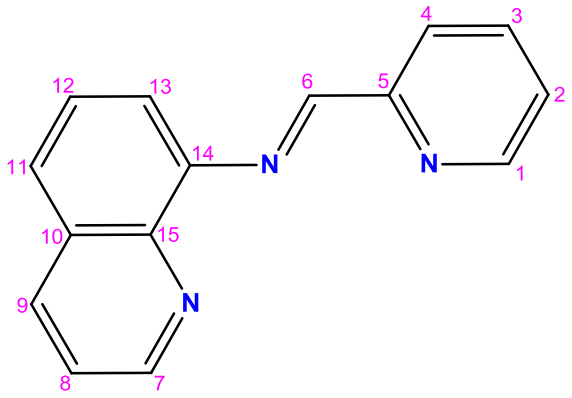

Figure 2.2.2: Structure of (*E*)-1-(pyridin-2-yl)-*N*-(quinolin-8-yl)methanimine showing the atom numbering scheme.

8-aminoquinoline (0.20 g, 1.39 mmol), pyridine-2-carboxaldehyde (0.15 g, 1.39 mmol) and a catalytic amount of piperidine (1 drop) were heated to reflux for two hours in ethanol (20 mL). The solvent was removed *via* rotary evaporation under reduced pressure, yielding an orange oil. Yield (0.32 g, 97%).

The following characterisation data were recorded:

^{1}H NMR (400 MHz, $CDCl_3$, 298 K) [δ, ppm]: 6.95 (m, 1H, 13); 7.17 (m, 1H, 8); 7.37, (m, 2H, 2, 12); 7.55 (m, 1H, 4); 7.90 (m, 1H, 3); 8.01 (m, 1H, 9); 8.10 (m, 1H, 1); 8.81 (m, 2H, 7, 11); 10.12 (s, 1H, 6). **^{13}C NMR** (100 MHz, $CDCl_3$, 303 K) [δ, ppm]: 150.24 (C-6); 147.43 (C-7); 143.97 (C-14); 138.47 (C-1); 137.47 (C-5); 137. 06 (C-15); 135.99 (C-4); 134.66 (C-9); 128.88 (C-3); 127.84 (C-10); 127.38 (C-12); 121.72 (C-2); 121.34 (C-13); 116.05 (C-11); 110.04 (C-8).

2.2.3 Synthesis of 5-(2-oxohexahydro-1*H*-thieno[3,4-*d*]imidazol-4-yl)-*N*-(1,10phenanthrolin-5-yl)pentanamide (L3).

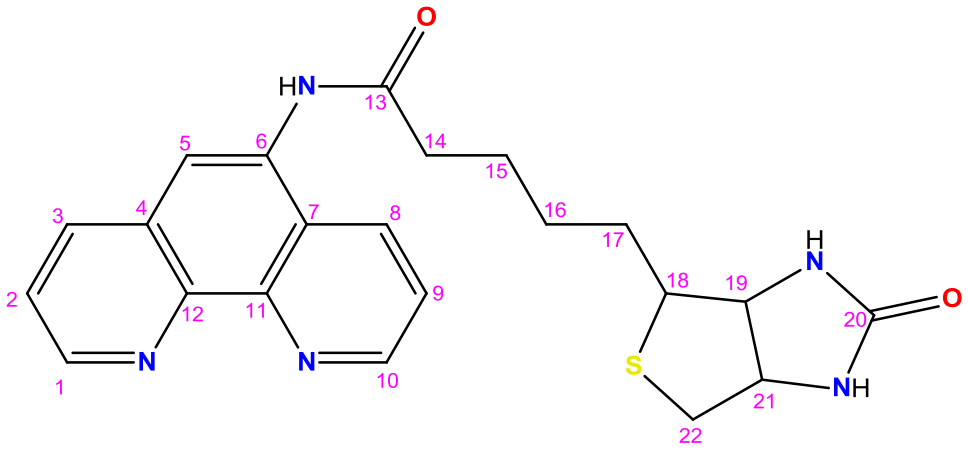

Figure 2.2.3: Structure of 5-(2-oxohexahydro-1*H*-thieno[3,4-*d*]imidazol-4-yl)-*N*-(1,10-phenanthrolin-5-yl) showing the atom numbering scheme.

Biotin (0.220 g, 0.90 mmol) was stirred in thionyl chloride (5 mL) in a flame-dried, two-neck round bottomed flask. The reaction was stirred for one hour, after which the thionyl chloride was removed *in vacuo*. The resulting yellow residue of biotin acyl chloride was redissolved in dry acetonitrile (10 mL). 5-amino-phenanthroline (0.195 g, 1.00 mmol) and DMAP (0.122 g, 1.00 mmol) were dissolved in dry acetonitrile (15 mL) in a separate flame-dried, two-neck round bottom flask. The biotin acyl chloride solution was added *via* cannula transfer to the amine solution and allowed to stir at room temperature overnight. An orange precipitate was collected *via* centrifugation and purified by column chromatography on neutral alumina using methanol as the eluent. The methanol was removed via rotary evaporation, yielding the final product. Yield (0.20 mg, 21%).

The following characterisation data were recorded:

^{1}H NMR (400 MHz, DMSO, 298 K) [δ, ppm]: 10.10 (s, 1H, N*H*); 9.15 (dd, 1H, J_1 = 4.32, J_2 = 1.63, 10); 9.05 (dd, 1H, J_1 = 4.27, J_2 = 1.69, 3); 8.63 (dd, 1H, J_1 = 8.45, J_2 = 1.51, 1); 8.48 (dd, 1H, J_1 = 8.26, J_2 = 1.53, 8); 8.20 (s, 1H, 5); 7.81 (dd, 1H, J_1 = 8.38, J_2 = 4.24, 9); 7.77 (dd, 1H J_1 = 8.15, J_2 = 4.39, 2); 6.42 (d, 1H, Biotin, N*H*), 6.35 (d, 1H, Biotin, N*H*), 4.32 (m, 1H, 21); 4.17 (m, 1H, 19); 3.12 (m, 1H, 18); 2.85 (m, 1H, 22); 2.61 (m, 1H, 22); 1.75 (m, 2H, 14); 1.65-1.27 (m, 6H, 15, 16, 17). **^{13}C NMR** (100 MHz, DMSO-d_6, 303 K) [δ, ppm]: 172.89 (C-13); 163.19 (C-20); 150.31 (C-11); 149.67 (C-10); 146.25 (C-1); 144.29 (C-6); 136.25 (C-3); 132.27 (C-8); 132.07 (C-4); 128.48 (C-12); 125.08 (C-5); 124.00 (C-9); 123.34 (C-7); 120.62 (C-2); 61.57 (C-19); 61.50 (C-21); 59.76 (C-18); 55.87 (C-22); 28.81 (C-14); 28.60 (C-16); 25.95 (C-15); 25.45 (C-17). **ES+**: 444.0945 *m/z* $(M+Na)^+$

2.2.4 Synthesis of *N*-(1,10-phenanthrolin-5-yl)propionamide (L4)

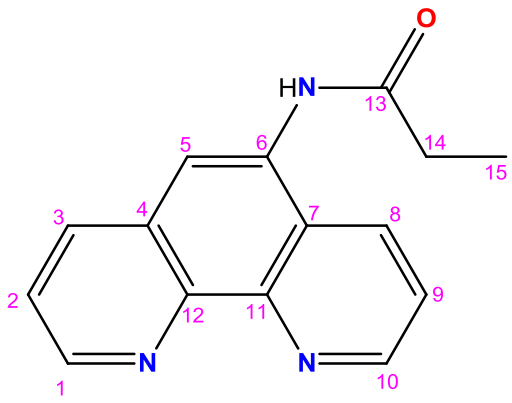

Figure 2.2.4: Structure of *N*-(1,10-phenanthrolin-5-yl)propionamide ligand showing the atom numbering scheme.

Propionic acid (0.11 mL, 1.5 mmol) and thionyl chloride (0.07 mL, 1.0 mmol) in anhydrous dichloromethane (5 mL) were stirred for one hour under an inert atmosphere in a two-necked round bottom flask. In parallel, 5-amino-phenanthroline (0.20 g, 1.0 mmol) and DMAP (0.13 g, 1.0 mmol) were stirred in anhydrous dichloromethane under nitrogen for one hour in a two-necked round bottom flask. The propionic acid reaction mixture was slowly added by cannula transfer to the phenanthroline amine solution and the resulting reaction mixture stirred under nitrogen overnight. An orange precipitate was collected *via* centrifugation and purified by column chromatography on neutral alumina eluted with methanol. The methanol was removed via rotary evaporation, yielding the final product. Yield (0.32 mg, 29%).

The following characterisation data were recorded:

^{1}H NMR (500 MHz, DMSO, 298 K) [δ, ppm]: 10.08 (s, 1H, NH); 9.13 (dd, 1H, J_1 = 4.32, J_2 = 1.63, 10); 9.03 (dd, 1H, J_1 = 5.66 J_2 = 2.67, 3); 8.62 (d, 1H, 1); 8.44 (d, 1H, 8); 8.18 (s, 1H, 5); 7.83 (dd, 1H, J_1 = 12.65, J_2 = 4.26, 9); 7.74 (dd, 1H, J_1 = 12.51, J_2 = 3.81, 2); 2.56 (m, 2H, 14); 1.20 (t, 3H, 15). **^{13}C NMR** (100 MHz, DMSO-d_6, 303 K) [δ, ppm]: 173.62 (C-13); 150.36 (C-11); 149.72 (C-10); 146.33 (C-1); 144.24 (C-6); 136.25 (C-3); 132.32 (C-8); 132.17 (C-4); 128.58 (C-12); 125.18 (C-5); 123.99 (C-7); 123.28 (C-9); 120.44 (C-2); 29.61 (C-14); 10.31 (C-15). **ES+**: 250.0815 *m/z* (M+).

2.3 Synthesis of Copper(II) Complexes

2.3.1 Synthesis of dichloro-(*E*)-1-(1,6-dihydropyridin-2-yl)-*N*-(1,2dihydropyridin-2-ylmethyl) methanimine copper(II) [Cu(L)(Cl_2)]

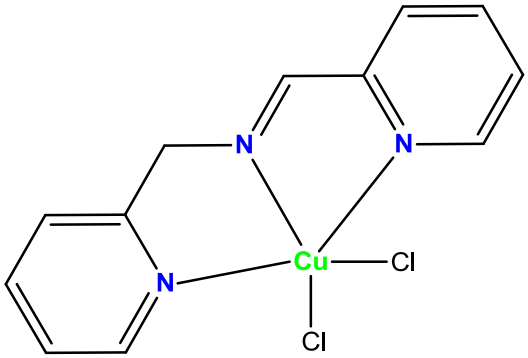

Figure 2.3.1: Structure of dichloro-(*E*)-1-(1,6-dihydropyridin-2-yl)-*N*-(1,2-dihydropyridin-2-ylmethyl)methanimine copper(II).

This complex was synthesised *via* a templating reaction. Picolylamine (0.20 g, 1.85 mmol) was dissolved in ethanol (15 mL) and stirred. To this solution copper(II) chloride dihydrate (0.32 g, 1.85 mmol) dissolved in ethanol (5 mL) was added dropwise resulting in a deep blue precipitate. Pyridine-2-carboxaldehyde (0.20 g, 1.85 mmol) was dissolved in ethanol (5 mL) and added dropwise to the reaction solution. The resulting mixture was stirred at room temperature for two hours yielding a deep green precipitate. The final product was collected *via* vacuum filtration and washed with cold ethanol. Yield (0.34 g, 56%).

The following characterisation data were recorded:

FT-IR (cm^{-1}): 765 ν(C-H), 1346 υ(C=C), 1597 ν(C=N), 3072 ν(C-H). **UV** (λ_{max}, ε) [nm, M^{-1} cm^{-1}]: 273, 14026. **ES+**: 288.9830 *m/z* $(M + Na)^+$. **Elemental analysis**: Calculated for $C_{12}H_{11}Cl_2CuN_3 \cdot 0.5EtOH$: C, 44.01; H, 3.98; N, 11.85. (Found: C, 44.43; H, 3.87; N, 11.97.)

2.3.2 Synthesis of dichloro-(*E*)-1-(pyridin-2-yl)-*N*-(quinolin-8-yl)-methanimine copper(II) [Cu(L2)(Cl_2)]

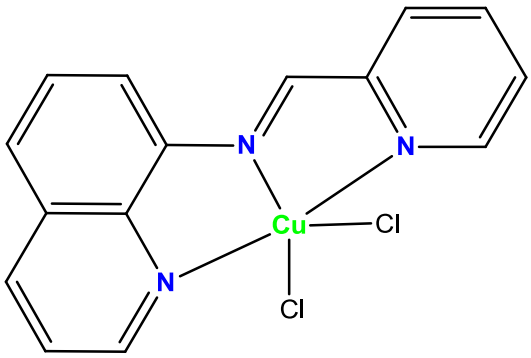

Figure 2.3.2: Structure of dichloro-(*E*)-1-(pyridin-2-yl)-*N*-(quinolin-8-yl)-methanimine copper(II) [Cu(L2)(Cl_2)].

The ligand L2 (0.32 g, 1.39 mmol) was dissolved in ethanol and copper(II) chloride dihydrate (0.24 g, 1.39 mmol) dissolved in a minimum volume of ethanol was added. The reaction mixture was heated to reflux for two hours yielding a green precipitate which was collected by gravity filtration. The complex was re-crystallised from methanol/diethyl ether. Yield (0.49 g, 95%).

The following characterisation data were recorded:

FT-IR (cm^{-1}): 767 ν(C-H), 1496, ν(C=C), 1598 ν(C=N), 2994 ν(C-H). **UV** (λ_{max}, ε) [nm, M^{-1} cm^{-1}]: 232, 17991; 354, 46402; 369, 19917. **ES+**: 331.0052 m/z $(M\text{-}Cl)^+$. **Elemental analysis**: Calculated for $C_{15}H_{11}Cl_2CuN_3 \cdot 0.5H_2O$: C, 47.99; H, 3.52; N, 11.43. (Found: C, 47.45; H, 3.78; N, 11.52.)

2.3.3 Synthesis of (chloro)-(1-(((quinolin-8-yl)imino)methyl)-2-naphtholato) copper(II) [Cu(L1)(Cl)]

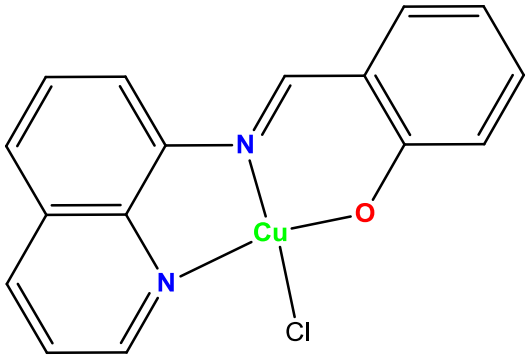

Figure 2.3.3: Structure of (chloro)-(1-(((quinolin-8-yl)imino)methyl)-2-naphtholato) copper(II), [Cu(L1)(Cl)].

To a solution of HL1 (1.26 g, 5.07 mmol) dissolved in ethanol (40 mL) was added a solution of $CuCl_2 \cdot 2H_2O$ (0.86 g, 5.07 mmol) dissolved in ethanol (20 mL) and the mixture heated to reflux for three hours. The solution was cooled to room temperature and the dark green semi-crystalline precipitate collected *via* gravity filtration and washed with cold ethanol (20 mL). Yield (1.63 g, 93 %).

The following characterisation data were recorded:

FT-IR (cm^{-1}): 1605 ν(C=N), 1204 ν(C=C), 1435 ν(C=C), 823 ν(C-H), 746 ν(C-H). **UV** (λ_{max}, ε) [nm, M^{-1} cm^{-1}]: 228, 34040; 330, 12710; 420, 10342. **ES+**: 310.0118 m/z $(M^{-}Cl)^{+}$ **Elemental analysis**: Calculated for $C_{16}H_{11}ClCuN_2O \cdot H_2O$: C, 52.75; H, 3.60; N, 7.69. (Found: C, 53.49; H, 3.12; N, 7.65).

2.3.4 Synthesis of (2,2'-Bipyridine)-(2-(((quinolin-8-yl)imino)methyl)phenolato) copper(II) chloride [Cu(L1)(Bpy)](Cl)

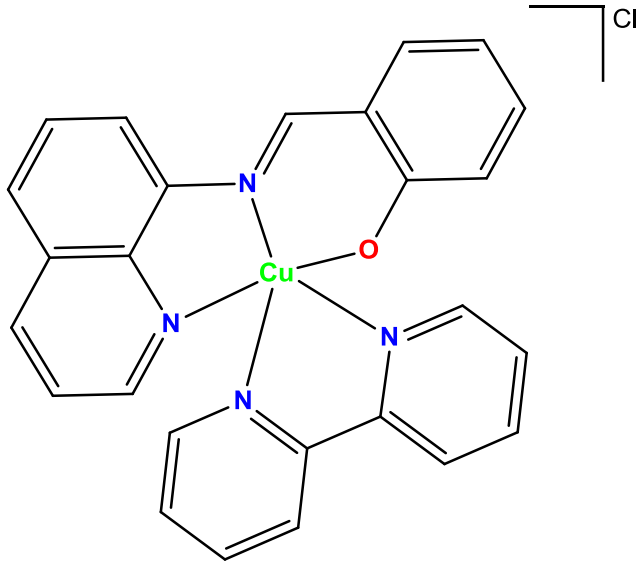

Figure 2.3.4: Structure of (2,2'-Bipyridine)-(2-(((quinolin-8-yl)imino)methyl)phenolato) copper(II)chloride [Cu(L1)(Bpy)(Cl)].

To a solution of [Cu(L1)(Cl)] (0.10 g, 0.29 mmol) dissolved in 5:1 THF/H_20 (25 mL) was added a solution of 2,2'-bipyridyl (45 mg, 0.29 mmol) in THF (15 mL) and the mixture heated to reflux for three hours followed by stirring at room temperature overnight. The solution was then left undisturbed and over two days dark green crystals formed. Yield (0.11 g, 76%).

The following characterisation data were recorded:

FT-IR (cm^{-1}): 1602 ν(C=N) ; 1437 ν(C=N); 1149 ν(C=C); 759 ν(C-H). **UV** (λ_{max}, ε) [nm, M^{-1} cm^{-1}]: 228, 42595; 283, 17308; 330, 12429; 420, 9977. **ES+**: 466.0814 *m/z* (M^+). **Elemental analysis:** Calculated for $C_{26}H_{19}ClCuN_4O.4H_20$: C, 54.36; H, 4.74; N, 9.75. (Found: C, 54.12; H, 3.99; N, 9.81).

2.3.5 Synthesis of (1,10-phenanthroline)-(2-(((quinolin-8-yl)imino)methyl) phenolato) copper(II) chloride [Cu(L1)(Phen)](Cl)

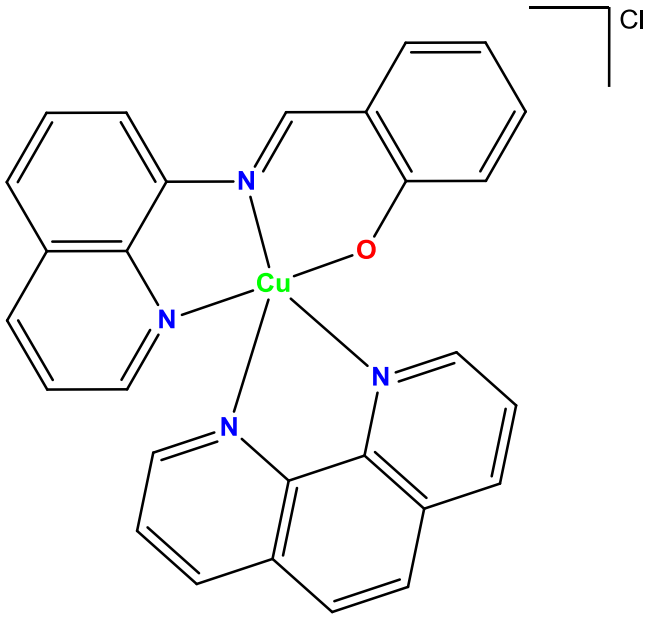

Figure 2.3.5: Structure of (1,10-phenanthroline)-(2-(((quinolin-8-yl)imino)methyl)phenolato) copper(II) chloride [Cu(L1)(Phen)(Cl)].

To a solution of [Cu(L1)(Cl)] (0.10 g, 0.29 mmol) dissolved in 5:1 THF/H_20 (25 mL) was added a solution of 1,10-phenanthroline (52 mg, 0.29 mmol) in THF (15 mL) and the mixture heated to reflux for three hours and then allowed to stir at room temperature overnight. The solvent was removed *in vacuo* yielding a dark green precipitate. The complex was crystalised from water *via* slow evaporation and the dark green crystals were collected by gravity filtration. Yield (0.12 g, 79%).

The following characterisation data were recorded:

FT-IR (cm^{-1}): 1603 ν(C=N); 902 ν(C-H); 836 ν(C=C); 723 ν(C=C). **ES+:** 489.9890 *m/z* (M^+). **UV** (λ_{max}, ε) [nm, M^{-1} cm^{-1}]: 226, 67497; 269, 37222; 330, 13970; 420, 10751. **Elemental analysis**: Calculated for $C_{28}H_{19}ClCuN_4O{\cdot}3H_2O$: C, 57.93; H, 4.43; N, 9.65. (Found: C, 57.55; H, 3.25; N 9.57).

2.3.6 Synthesis of (1,10-phenanthroline-5amine)-(2-(((quinolin-8-yl)imino) methyl)phenolato) copper(II) chloride [Cu(L1)(Phen-NH_2)](Cl)

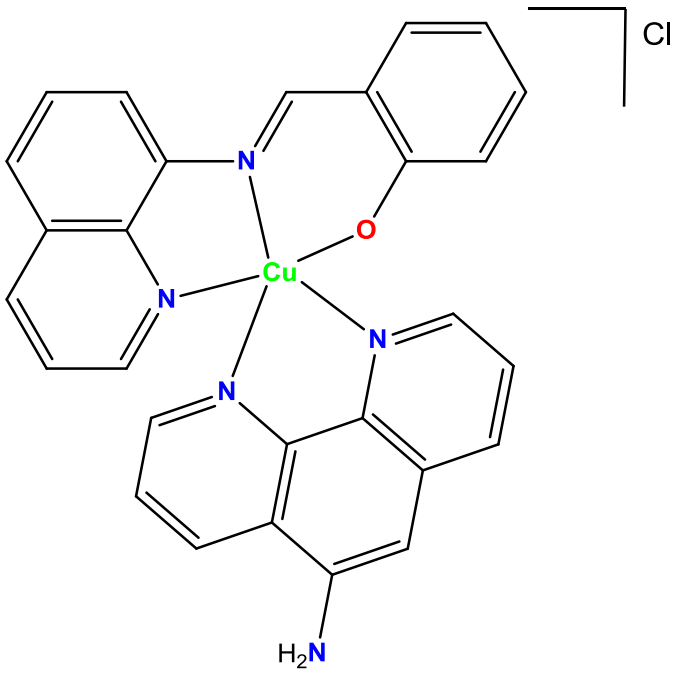

Figure 2.3.6: Structure of (1,10-phenanthroline-5-amine)-(2-(((quinolin-8-yl)imino)methyl) phenolato)-copper(II) chloride [Cu(L1)(Phen-NH2)](Cl).

To a solution of [Cu(L1)(Cl)] (0.10 g, 0.29 mmol) in 5:1 THF/H_20 (25 mL) was added a solution of 1,10-phenanthroline-5-amine (52 mg, 0.29 mmol) in THF (15 mL) and the mixture heated to reflux for three hours and then allowed to stir at room temperature overnight. The solvent was removed in vacuo yielding a dark green precipitate. The complex was crystalised from water *via* slow evaporation and the dark green crystals collected by gravity filtration and washed with cold THF. Yield (99 mg, 79%).

The following characterisation data were recorded:

FT-IR (cm^{-1}): 1600 ν(C=N) ; 1460 ν(C-H); 1401 ν(C-H); 832 ν(C=C). **ES+**: 504.9900 *m/z* (M^+). **UV** (λ_{max}, ε) [nm, M^{-1} cm^{-1}]: 226, 54180; 250, 35670; 287, 27722; 332; 15982; 418, 9734. **Elemental analysis**: Calculated for $C_{28}H_{20}ClCuN_5O{\cdot}H_2O$: C, 60.11; H, 3.96; N, 12.52. (Found: C, 59.75; H, 3.78; N, 11.95).

Chapter 3 | Synthesis

3.1 Synthesis of Schiff Base Ligands

A common feature in many of the ligands synthesised in this work is imine bonds. Imines are formed by a reaction between a ketone or aldehyde with a primary amine and are characterised by a carbon-nitrogen double bond. The imine formed by the reaction of a carbonyl and primary amine is often referred to as a Schiff base.[44] A general scheme for the synthesis of a Schiff base is shown in Figure 3.1.1.

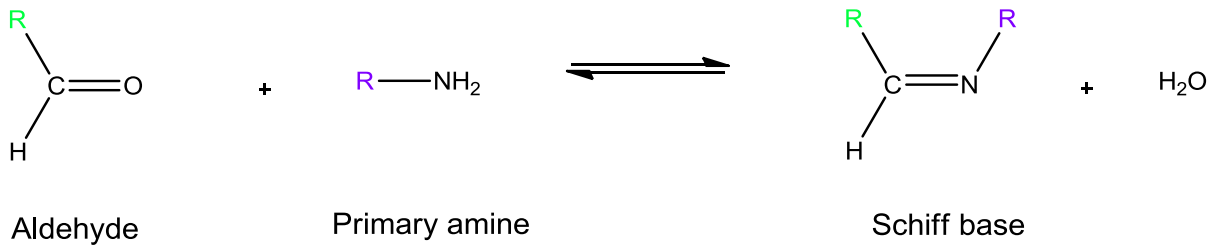

Figure 3.1.1: General reaction scheme for Schiff base formation.[44]

The first step in the mechanism for Schiff base formation involves attack of the carbonyl carbon by the nitrogen of the amine. This is followed by proton transfer from the ammonium ion to the alkoxide group. This forms a neutral tetrahedral intermediate, called a carbinolamine, which exists is equilibrium with two protonated forms. Protonation can take place on either the oxygen or nitrogen atom. Water is eliminated from the oxygen-protonated intermediate resulting in a protonated imine which then loses a proton forming a double bond between the nitrogen and carbon.[44] This reaction mechanism is depicted in Figure 3.1.2 using ligand HL1 as a representative example.

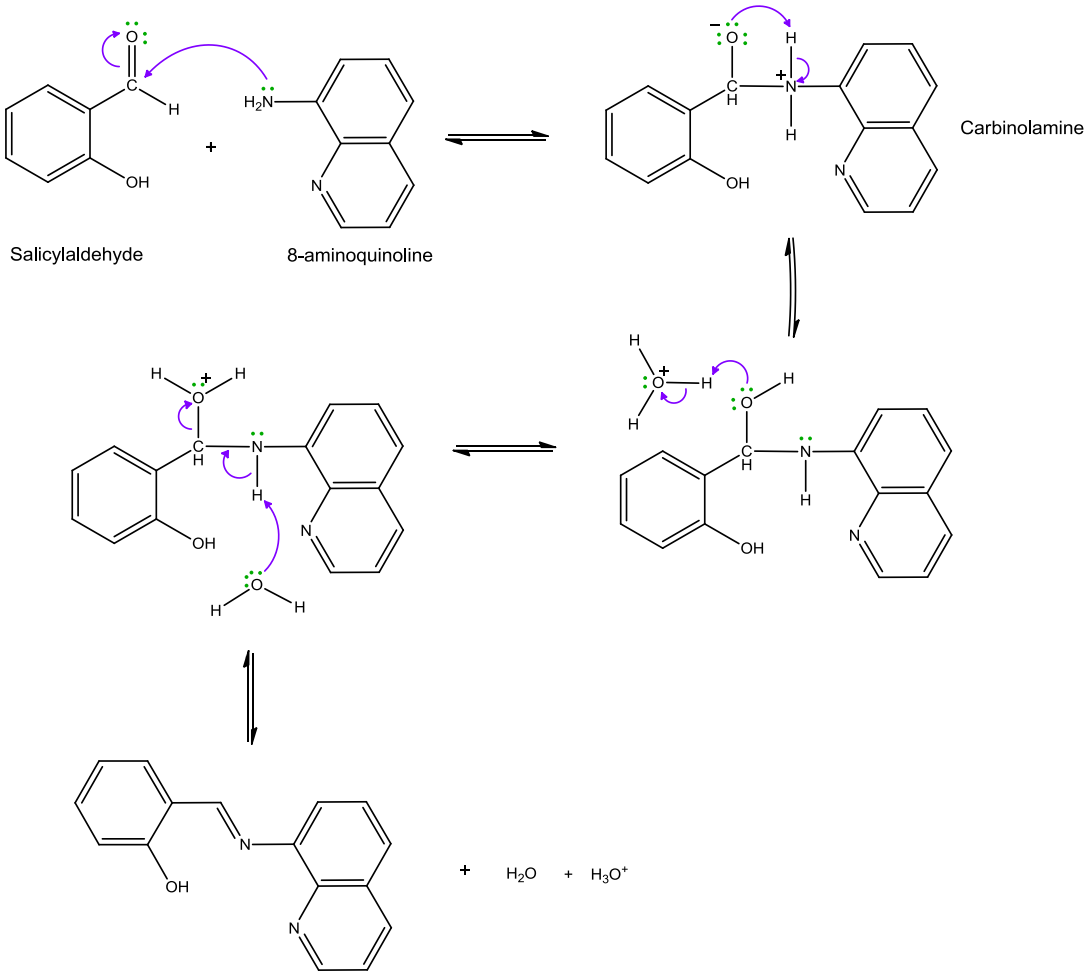

Figure 3.1.2: Reaction mechanism for the acid-catalysed synthesis of (*E*)-2-((quinolin-8-ylimino)methyl)phenol.

3.2 Biotin Acyl Chloride Formation

Of the numerous classes of carbonyl compounds, carboxylic acids are one of the most commonly available and inexpensive acids both in biological systems and in the laboratory.[44] A drawback of carboxylic acids is that they are relatively unreactive towards nucleophilic acyl substitution reactions. This is due to the carboxylic acid's OH group being a poor leaving group as it is a strong base.[44] As a result of this decreased reactivity, chemists need to activate the carboxylic acids to promote nucleophilic acyl substitution reactions. Considering all carboxylic derivatives, acyl halides are the most reactive. Carboxylic acids can be converted to acyl chlorides by reaction with phosphorus trichloride (PCl_3), thionyl chloride ($SOCl_2$), oxalyl chloride $(COCl)_2$, phosphorus oxychloride ($POCl_3$) or phosphorus pentachloride ($POCl_5$).[45] A general scheme for the conversion of a carboxylic acid to an acyl chloride using thionyl chloride is shown in Figure 3.2.1.

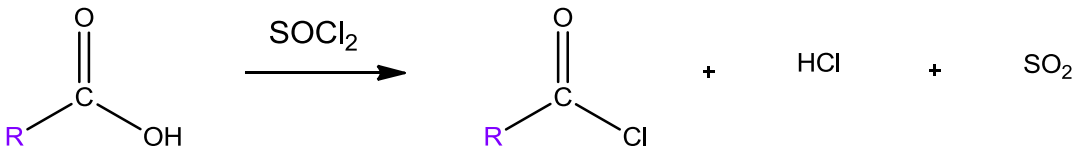

Figure 3.2.1: General reaction scheme for acyl chloride formation from a carboxylic acid using thionyl chloride.[44]

In the above reaction, thionyl chloride acts as both the solvent and reagent in the conversion of the carboxylic acid to acyl chloride. In the presence of moisture, the acyl chloride is very susceptible to hydrolysis back to the carboxylic acid.[44] Therefore, the product of this reaction was not isolated and characterised due to its high sensitivity and was used directly in the next step. This procedure was used to activate the carboxylic acid group of biotin (Figure 3.2.2) to allow for coupling to an amine group to form a co-ligand with tumour cell targeting abilities.

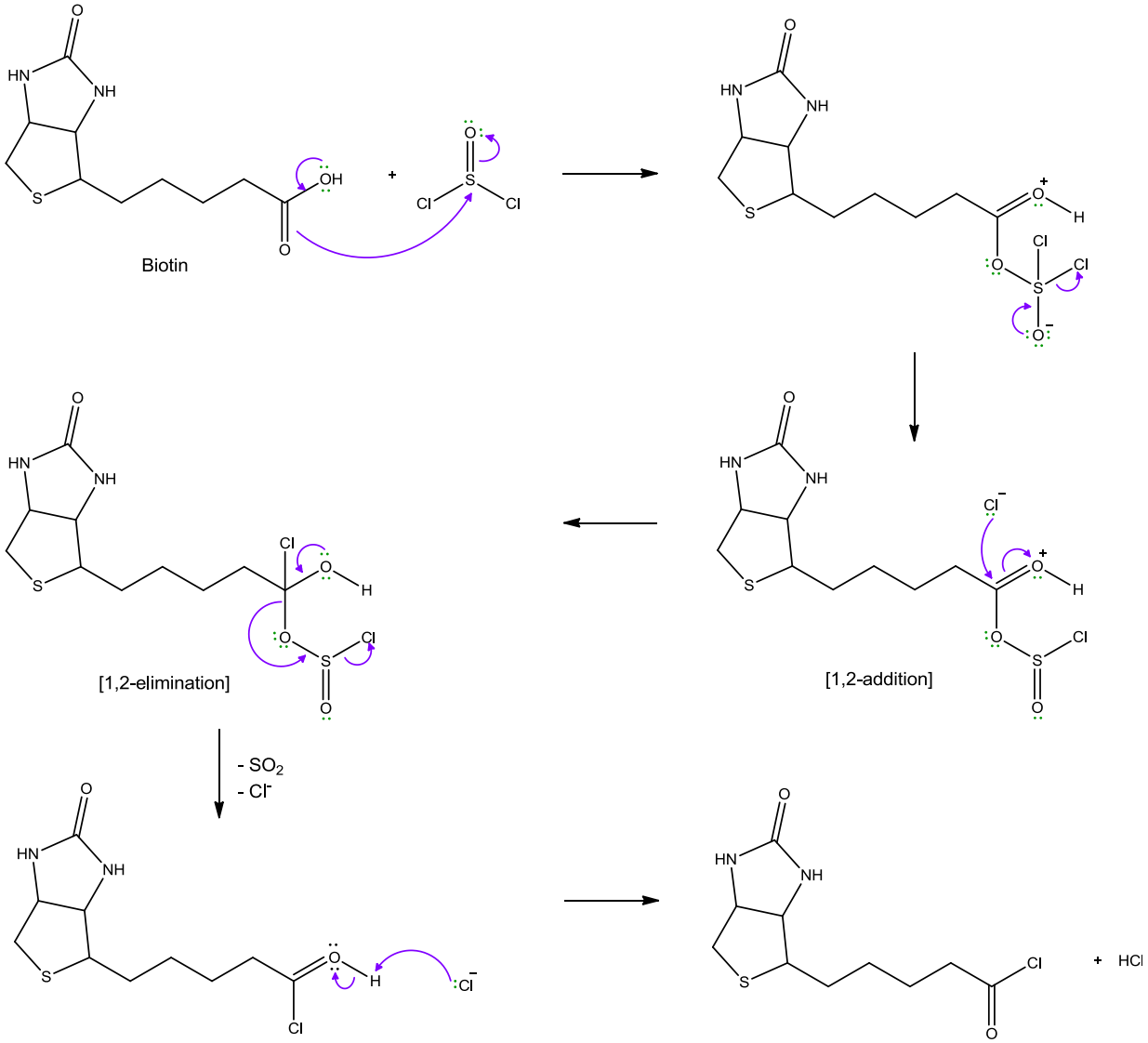

Figure 3.2.2: Reaction mechanism for the formation of 5-(2-oxohexahydro-1*H*-thieno[3,4-*d*]imidazol-4-yl) pentanoylchloride.[46]

The conversion of biotin to the biotin acyl chloride derivative proceeds through a [1,2]-addition reaction of the chloride ion to the carbonyl carbon followed by a [1,2]-elimination reaction which yields the acyl chloride, HCl and SO_2. The reaction proceeds by a nucleophilic attack on thionyl chloride by the carbonyl group of the carboxylic acid. This is followed by the removal of a chloride (the leaving group) resulting in a chlorosulfite species. The carbonyl group then undergoes nucleophilic attack by the chloride ion. SO_2 and a chloride ion are removed in the next step and lastly deprotonation forms HCl and leaves the biotin acyl chloride derivative.[44, 46]

3.3 Amide Bond Formation

Amides are common compounds featured in both small and complex, natural and synthetic molecules.[47] According to the Comprehensive Medicinal Chemistry Database, the carboxamide functional group is found in more than 25% of known drugs.[47] This is due to favorable properties of amides such as being stable under physiological conditions, they are neutral and they possess both hydrogen-bond accepting and donating properties which can potentially stabilise drug/target conjugates. The formation of an amide bond can be achieved using various methods. In this work it is a result of reacting the desired amine and an acyl chloride. A base, such as 4-dimethylaminopyridine (DMAP), is required to firstly trap the HCl formed and to accelerate the reaction. The HCl must be trapped to prevent the conversion of the amine into its unreactive hydrochloride salt.[45] A general scheme for the synthesis of an amide from an acyl chloride and primary amine is shown in Figure 3.3.1.

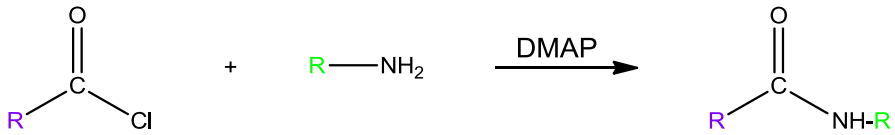

Figure 3.3.1: General reaction scheme for amide formation from acyl chloride.[44]

The mechanism for the formation of the biotin-tagged co-ligand which features an amide bond is illustrated in Figure 3.3.2.

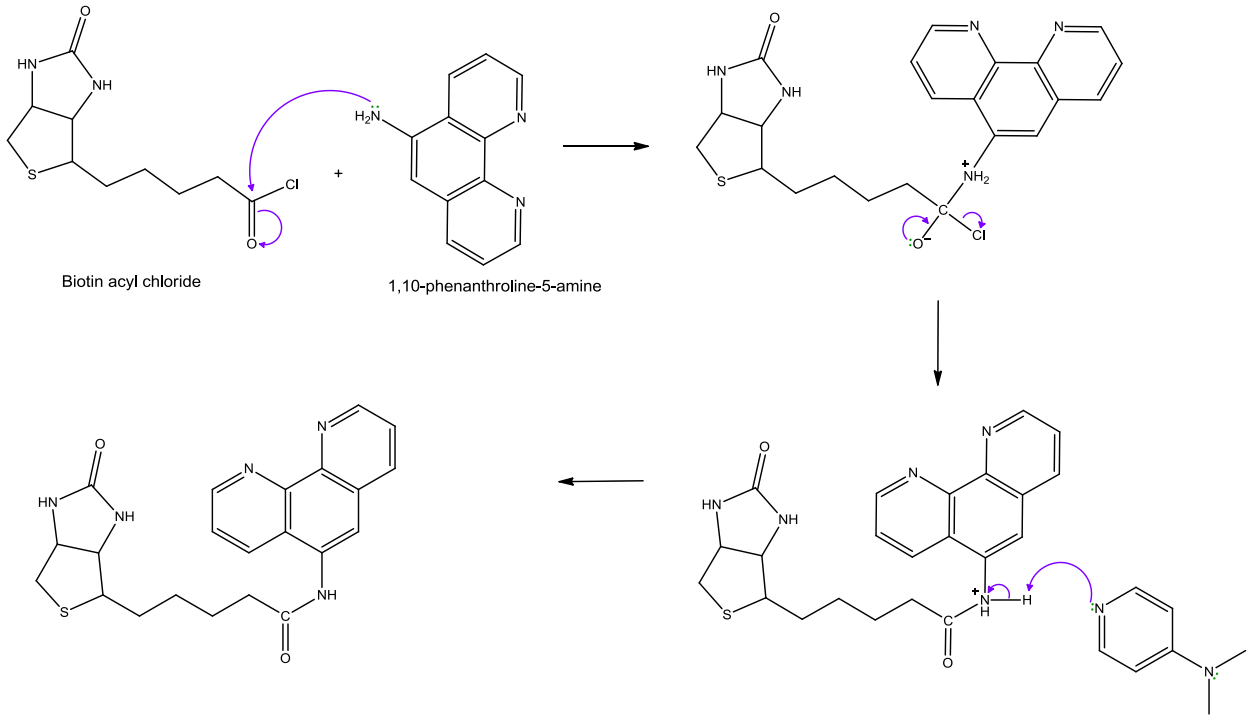

Figure 3.3.2: Reaction mechanism indicating amide bond synthesis in the formation of 5-(2-oxohexahydro-1*H*-thieno[3,4-*d*]imidazol-4-yl)-*N*-(1,10-phenanthrolin-5-yl)pentanamide.[44, 45]

The reaction between the acyl chloride and amine was carried out at room temperature due to the high reactivity of the acyl chloride and proceeded *via* the following mechanism: the reaction firstly undergoes an addition step followed by an elimination. The carbonyl carbon on the acyl chloride undergoes nucleophilic attack by the amine nitrogen atom forming a tetrahedral ammonium species. The elimination stage occurs in a two-step process, firstly the carbon-oxygen double bond reforms and the chloride ion is eliminated. This is followed by the elimination of the proton from the ammonium ion which can be removed by either the chloride ion (producing HCl) or by a second amine (DMAP in this context) forming an ammonium chloride species.[45]

3.4 Synthesis of Metal Chelates

The metal chelates synthesised in this project comprise three single-ligand Schiff base complexes and three heteroleptic Schiff base complexes. All complexes were coordinated to copper(II) chloride. The metalation procedure involved refluxing the Schiff base ligands with the copper(II) metal salt in a 1:1 mole ratio in a polar solvent. The reaction mechanisms in Figure 3.4.1 illustrates the formation of the single-ligand complexes.

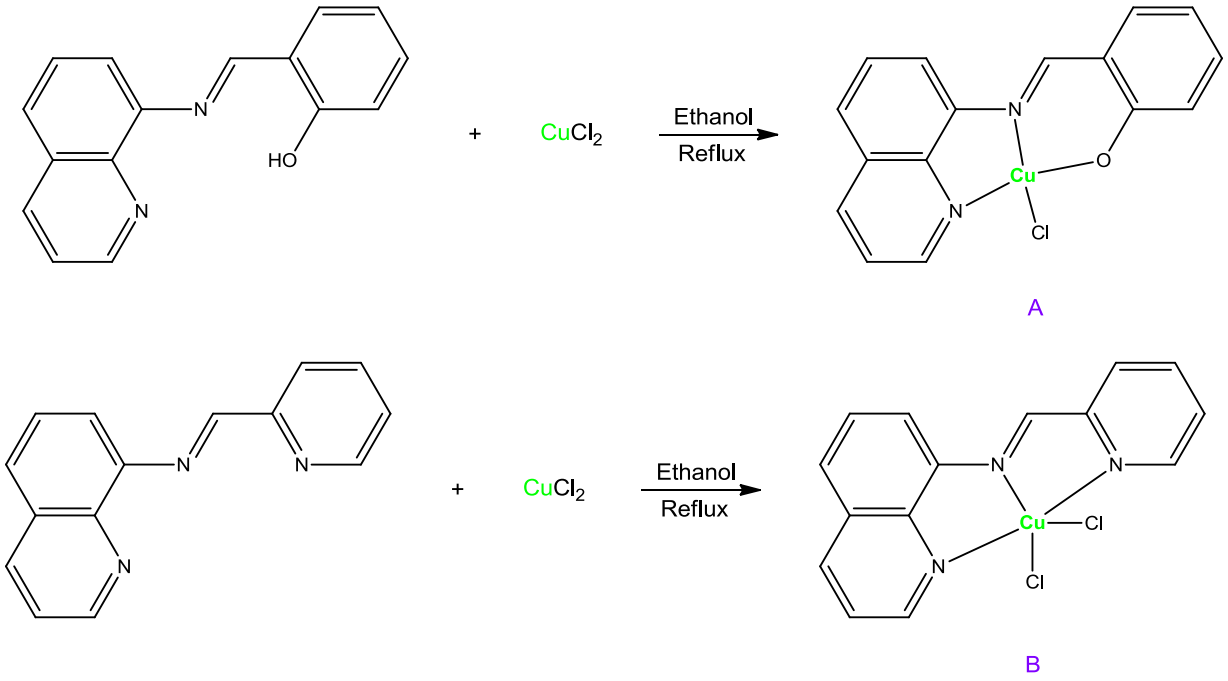

Figure 3.4.1: Reaction illustrating the general synthetic method used for metalation of the Schiff base ligands in this work.

Reaction of the neutral tridentate Schiff base ligands with copper(II) chloride yields a square pyramidal complex with the coordination sites occupied by the tridentate ligand and two monodentate chloride ligands. The coordination of the monoanionic tridentate ligand leads to a neutral square planar complex with the coordination sites occupied by the tridentate ligand and a single chloride ligand.

The three heteroleptic complexes were then synthesized by adding a stoichiometric amount of the desired co-ligand to the square planar copper(II) chelate (designated A in Figure 3.4.1) in a 1:1 mole ratio in a 5:1 THF/H_20 solvent system. In this process, the inner sphere chloride ligand is displaced by a neutral bidentate ligand leading to a square pyramidal cationic chelate. This chelate is isolated as the chloride salt. The general reaction procedure for formation of the heteroleptic complexes is shown in Figure 3.4.2. The three co-ligands used were 2,2'-bipyridyl, 1,10-phenanthroline and 1,10-phenanthroline-5-amine.

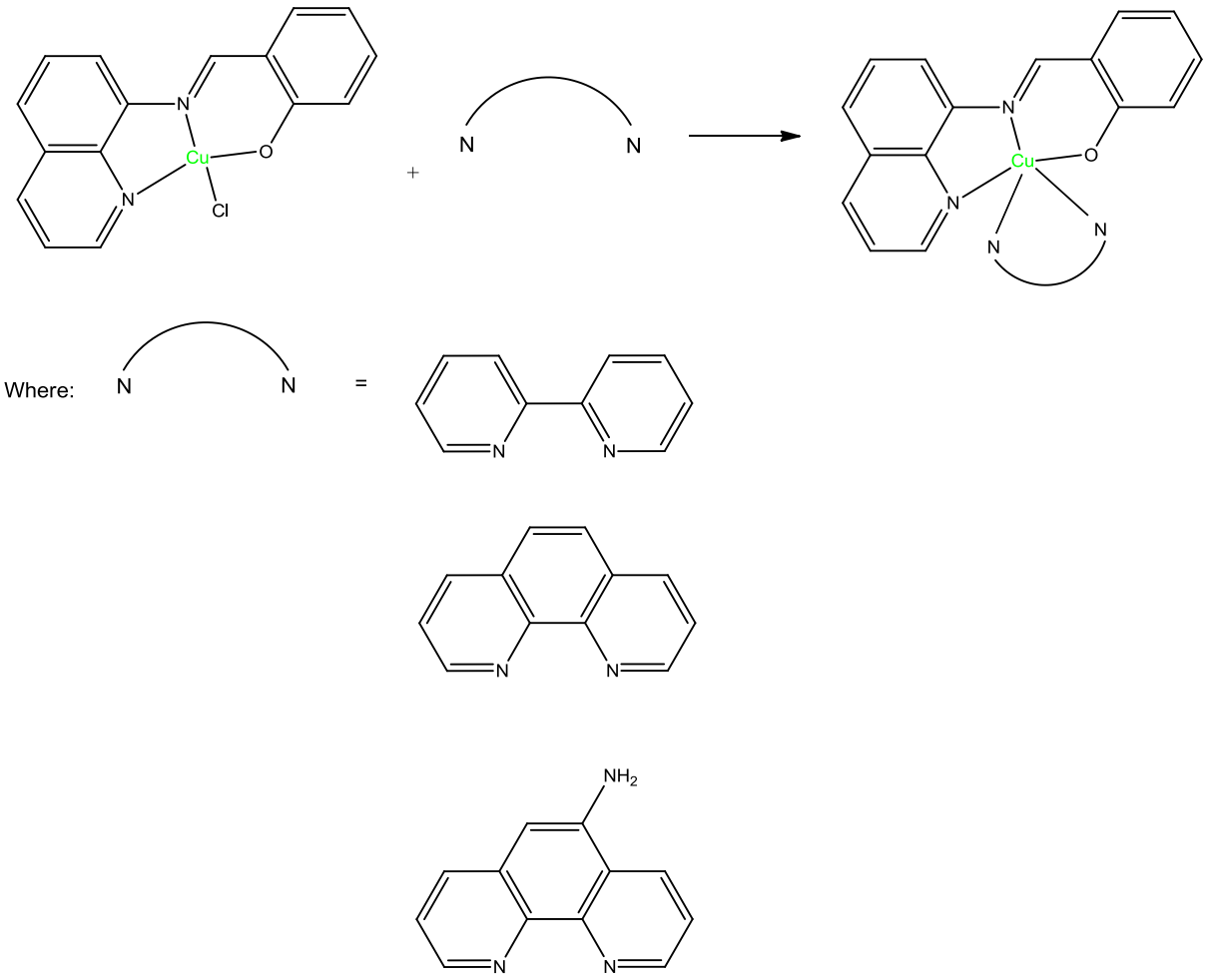

Figure 3.4.2: Reaction mechanism for the synthesis of the heteroleptic copper(II) complexes.

All complexes in this study are water soluble and were recrystallized either from water, methanol or THF. The solvent system of 5:1 THF/H_20 was used due to complex A only being partially soluble in methanol and THF. This resulted a mixture of products and the reaction not going to completion. The solvent system 5:1 THF/H_20 produced the desired complexes in good yields and high purity.

Chapter 4 | Spectroscopy

4.1 The Electromagnetic Spectrum

Spectroscopy refers to a branch of science which investigates the spectra produced when atoms, molecules or ions interact with or emit electromagnetic radiation. Energy is exchanged when electromagnetic radiation interacts with matter. Atoms and molecules may absorb this energy. When these atoms and molecules return to their normal, more stable energy states, they emit radiation in various parts of the electromagnetic spectrum. Both the absorbed and emitted radiation can give insight into the structure of molecules and atoms. The electromagnetic spectrum extends from high-frequency (short wavelength) gamma rays of 10^{20} Hz to low-frequency (long wavelength) radio waves of 10^{8} Hz.[48] Table 4.1.1 shows the various regions of the electromagnetic spectrum which are of interest in chemical analysis.

Table 4.1.1: Regions of the electromagnetic spectrum of interest in chemical analysis.[49]

Radiation	Use in chemistry
Gamma rays	Emitted in radioactive decay
X-rays	Diffraction of X-rays used to determine molecular structures.
Ultraviolet	Absorption spectra used for molecule electronic structure determination.
Visible	Emission and absorption spectra used for quantitative and qualitative identification of elements.
Infrared	Absorption spectra used for structure determination.
Radiowaves	Absorption at accurately measured frequencies used to determine molecule structure (NMR, EPR).

Gamma and X-rays interact with electrons and atomic nuclei of molecules while visible light and ultraviolet radiation interact with the electrons of a compound. Infrared energy is absorbed and increases the motion of atoms in a molecule relative to each other and radiowaves interact with the electronic spin of the electrons in a compound. Figure 4.1.1 shows a summary of the electromagnetic spectrum's wavelengths and how they interact with matter.

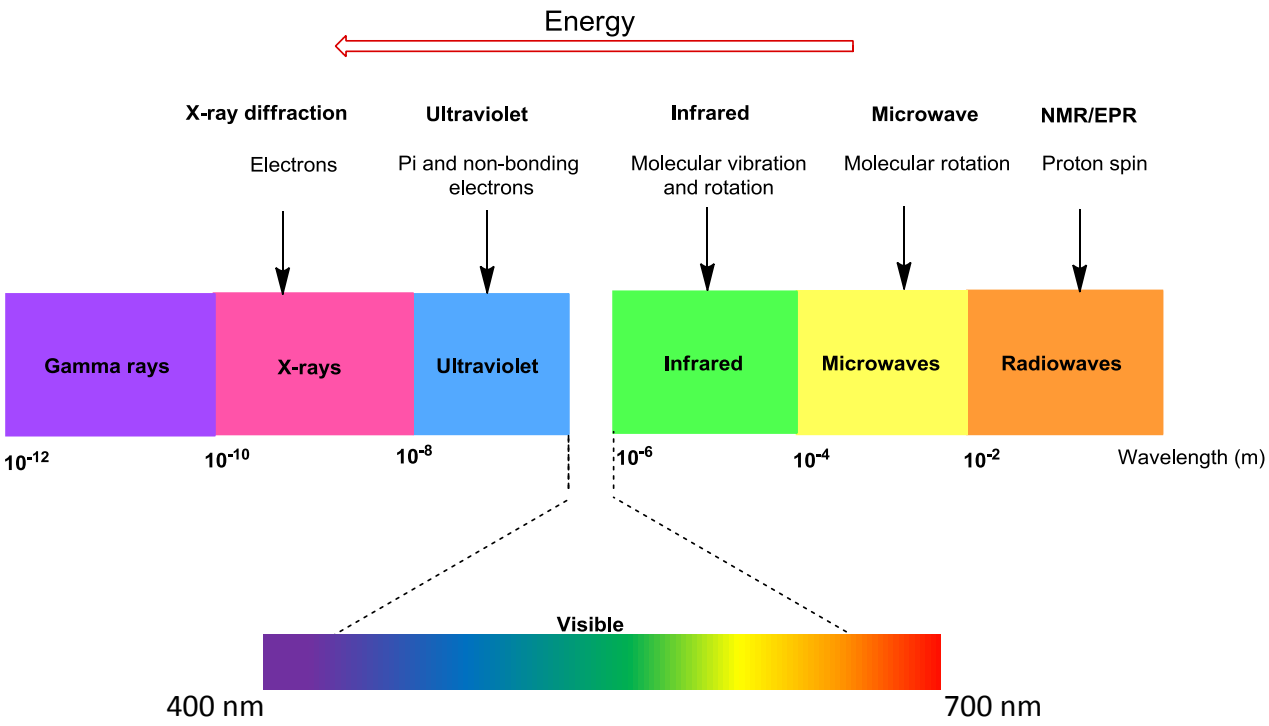

Figure 4.1.1: Summary of wavelengths of the electromagnetic spectrum and their applications in molecular spectroscopy.

In this study, a range of spectroscopic techniques were used to characterise and study the metal chelates and free ligands. The techniques include X-ray crystallography, UV/vis absorption, infrared, Nuclear Magnetic Resonance (NMR) and fluorescence spectroscopy as well as mass spectrometry.

4.2 Infrared (IR) Spectroscopy

4.2.1 Introduction

Infrared radiation is lower in frequency than that of visible light. The IR radiation of most interest in chemical analysis ranges in wavenumbers from 400-4000 cm^{-1}. It is wellknown that the atoms in a molecule are constantly moving with the bonds bending and stretching. Each bending and stretching vibration in a molecule proceeds with a characteristic frequency. When a molecule is radiated with photons of a frequency that correlates with the frequency of a vibration or bending mode of a certain bond, the molecule will absorb energy which will intensify the bending and stretching. This yields an IR spectrum. By measuring the wavenumbers of the absorbed energy, it is possible to determine what kind of bonds or functional groups exist in a given compound.[49, 50]

The vibrational frequency of a particular bond is characteristic of the two bonded atoms. It is also influenced by the surrounding bonds of that molecule. The IR spectra of any given compound therefore gives information about what functional groups are present in that molecule along with how these functional groups are positioned relative to one another. Rotations in a compound, elemental vibrations and electron movements within a compound can all be detected with IR spectroscopy.[48]

4.2.2 Results and Discussion

In this study of heteroleptic complexes, IR spectroscopy was employed to firstly investigate the shifts in peaks of the co-ligands after chelation to copper(II) and secondly the C=N stretching and C-H aromatic bending of the primary ligand. The peaks of interest are associated with the C-N stretching mode in 2,2'-bipyridyl, 1,10-phenathroline and 1,10-phenanthroline-5-amine. Table 4.2.1 compares the frequencies of the ν(C-N) stretch of the free co-ligand with the co-ligand frequencies after chelation to form the heteroleptic complexes.

Table 4.2.1: Comparison of ν(C-N) IR frequencies of co-ligands with their respective heteroleptic complexes.

Co-ligand	Frequency (cm^{-1})	Frequency in heteroleptic complex (cm^{-1})
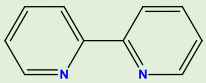	1555	1502
	1577	1526
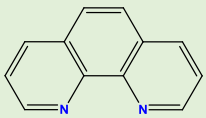	1501	1461
	1586	1507
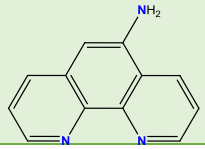	1487	1491
	1454	1461

Table 4.2.1 highlights an interesting trend for the 2,2'-bipyridyl and 1,10-phenathroline co-ligands and their respective copper(II) complexes. The free ligands have medium peaks for the C-N stretch in the region of 1500-1600 cm^{-1}. The heteroleptic complexes all showed a decrease in frequency for the same bond stretch which is attributed to the electron withdrawing nature of the copper(II) metal center. Oxidised metal ions are electron deficient and will remove electron density from the ligands which will result in a weakening of the bonds

in the region of the coordination sphere. This manifests as a decrease in the frequencies of the ν(C-N) stretching mode for the complexes.

There is a noticeable decrease in the ν(C-N) frequency for 1,10-phenanthroline-5-amine compared to the 2,2'-bipyridyl and 1,10-phenathroline co-ligands. The ligand is seen to have stretching frequencies in the region of 1454 and 1487 cm^{-1} while the other two ligands have shifts at higher frequencies, in the order of 1500 cm^{-1}. This decrease is attributed to the electron withdrawing effect of the NH_2 group which reduces electron density over the fused aromatic rings. This lowers the bond order and leads to lower stretching frequencies.

Figure 4.2.1 shows an overlay of the IR spectra of the co-ligand 2,2'-bipyridyl with that of the heteroleptic copper(II) complex, [Cu(L1)(Bpy)](Cl). The peaks of interest at 1555 and 1577 cm^{-1} for 2,2'-bipyridyl are the C=N stretching frequencies. These bands are shifted to lower wave numbers (1526 and 1502 cm^{-1}, respectively) once chelated to the copper(II) metal center. Another peak of interest in the chelate spectrum occurs at 1602 cm^{-1}, which is not seen in the co-ligand spectrum. This strong peak is caused by the C=N double bond of the Schiff base ligand thus confirming the coordination of both ligands to the copper(II) metal center. The imine bond stretching frequency of the metal chelate is also noted to be at lower wavenumbers for comparable free ligands. In a study by Akerman *et. al.* three similar free ligands were noted to have imine bond stretching frequencies ranging from 1632.18 cm^{-1} – 1643.67 cm^{-1}.[51] The imine bond stretching frequency of the metal chelate is also lower than the literature value of 1680 cm^{-1} for an uncoordinated bond. This shift to lower energy is a result of the electron withdrawing nature of the metal ion.

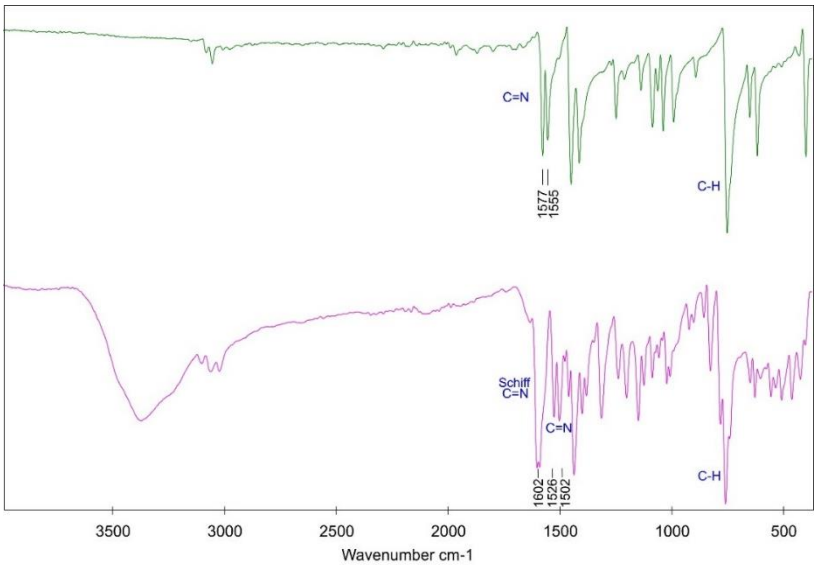

Figure 4.2.1: IR spectrum overlay of 2,2'-bipyridyl (green) with the corresponding heteroleptic complex [Cu(L1)(Bpy)](Cl) (purple).

4.3 Nuclear Magnetic Resonance (NMR) Spectroscopy

4.3.1 Introduction

NMR spectroscopy is mostly used to identify and confirm the carbon-hydrogen framework of organic and inorganic molecules.[50] Nuclei of atoms such as ^{1}H, ^{13}C, ^{15}N, ^{19}F and ^{31}P, all possess spin, caused by an odd number of protons or neutrons, which are detected by NMR. It is this spin property that allows certain atoms to be studied by NMR spectroscopy. Due to the charge and spin, these nuclei have magnetic moments. These magnetic moments are randomly orientated in the absence of an externally applied magnetic field. However, in the presence of a strong magnetic field the magnetic moments align either with (lower energy α-spin state) or against (higher energy β-spin state) the applied magnetic field.[50] This process is illustrated in Figure 4.3.1 below.

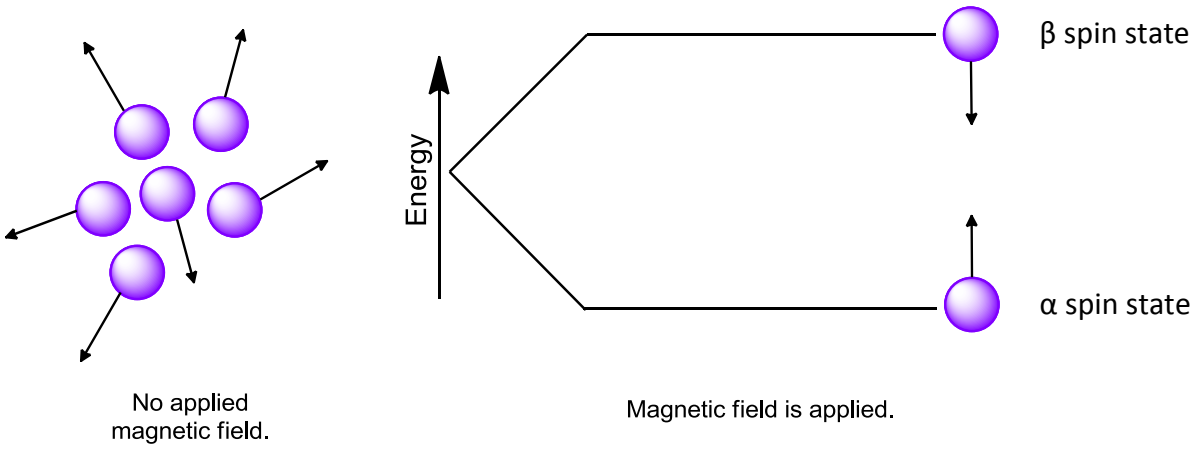

Figure 4.3.1: Magnetic moment behaviour of nuclei with and without an applied magnetic field.[3]

When the nuclei absorb radio frequency radiation, they flip their spin from an α-spin state to a β-spin state. When the nuclei flip back down to the lower energy α-spin state, the spin flipping of the nuclei generates a signal whose frequency correlates to the energy difference between the α and β spin states. The NMR spectrometer detects and analyses these signals and displays them as an NMR spectrum which is a plot of signal frequency vs intensity.[50]

In this study ^{1}H and ^{13}C NMR spectroscopy were used as a characterisation and structural elucidation tool for all ligands. The copper(II) chelates could not be studied by NMR spectroscopy due to an unpaired electron in the d^9 electronic configuration of the copper(II) centre, thus making the complexes paramagnetic and NMR inactive.

4.3.2 Results and Discussion

Figure 4.3.2 shows the hydrogen numbering scheme used for 1,10-phenanthroline-5-amine (phen-amine).

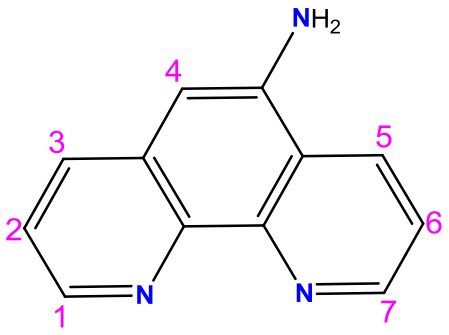

Figure 4.3.2: Structure of 1,10-phenanthroline-5-amine showing hydrogen numbering scheme.

1,10-phenanthroline-5-amine is used as a ligand and building block for a further two ligands as the amine group is an ideal site for functionalisation. The ligands L3 and L4 containing biotin and propionic acid substituents, respectively were synthesised from phen-amine. L3 will be used as a representative example for both L3 and L4 in further discussion. Figure 4.3.3 shows the ^{1}H NMR spectrum of phen-amine as well as the downfield region of the NMR spectrum of L3. ^{1}H and ^{13}C NMR spectra for all ligands are fully assigned in the experimental section (Chapter 2). The respective ^{1}H and ^{13}C NMR spectra for each ligand available in Appendix A2.

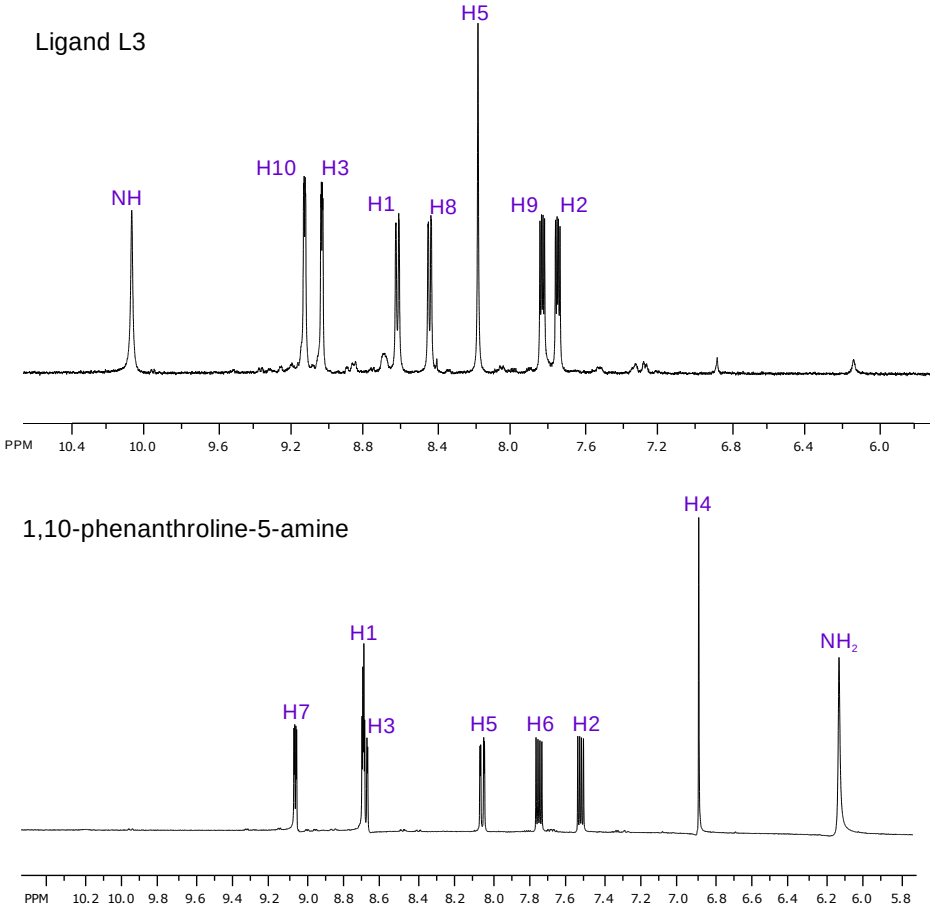

Figure 4.3.3: ^{1}H NMR spectra of the aromatic (downfield) region of L3 and phen-amine.

Amine NH chemical shifts can occur anywhere between 1.0 ppm – 6.0 ppm depending on the surrounding substituents, concentrations and hydrogen bonding in solution. The ^{1}H NMR spectrum for phen-amine shows a very distinctive, singlet amine peak at 6.12 ppm. After the coupling of biotin, the NMR spectrum illustrates the disappearance of the amine peak and the appearance of an amide peak at 10.13 ppm, which is not present in the phen-amine spectrum. Amide chemical shifts are commonly observed between 5.0 ppm – 9.0 ppm and may vary due to surrounding atoms. Hydrogen bonding could be attributed to the peak lying slightly outside of the designated range for amide chemical shifts. Similar changes indicative of a successful coupling reaction and amide bond formation are noted for L4.

Figure 4.3.4 shows fully assigned ^{1}H NMR spectrum of L3, this is followed by the fully labelled ^{13}C NMR spectrum of L3 in Figure 4.3.5. Both spectra were assigned using additional structural information obtained from the two-dimensional HSQC and COSY NMR experiments.

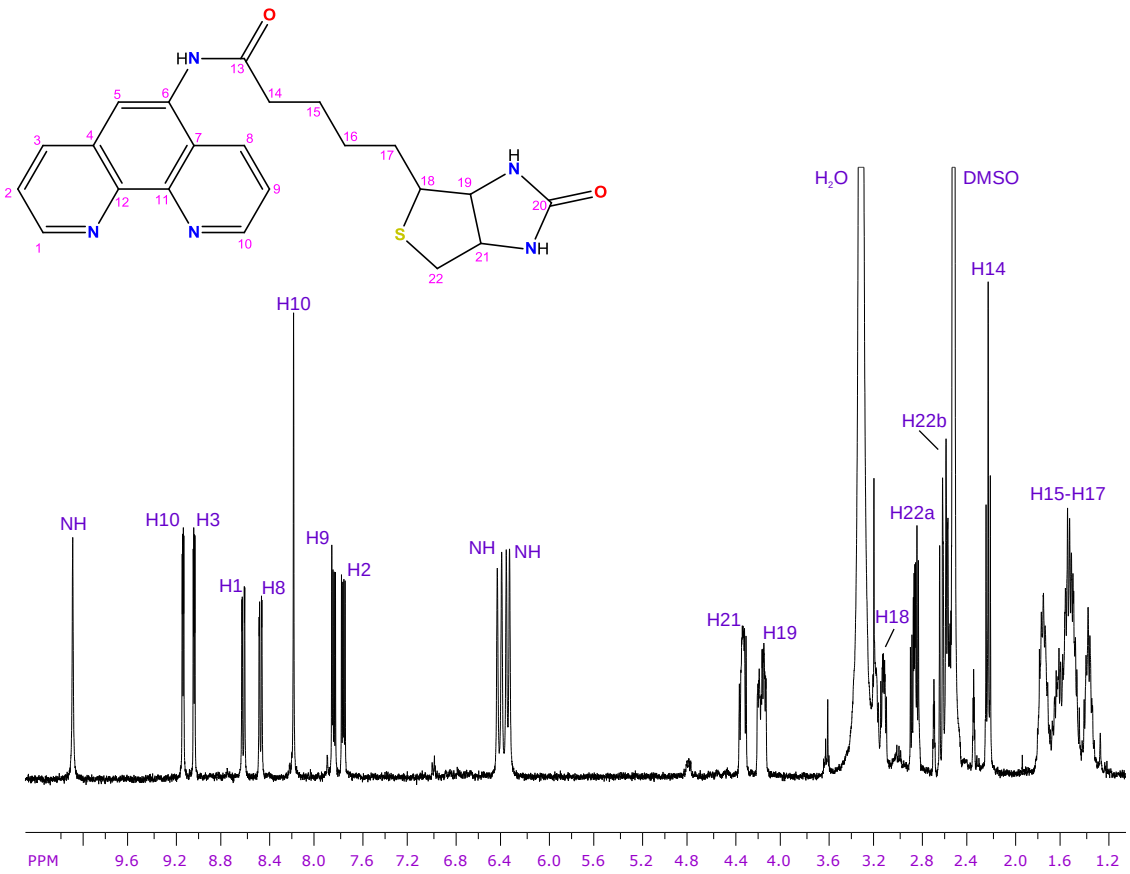

Figure 4.3.4: Fully assigned ^{1}H NMR spectrum of L3.

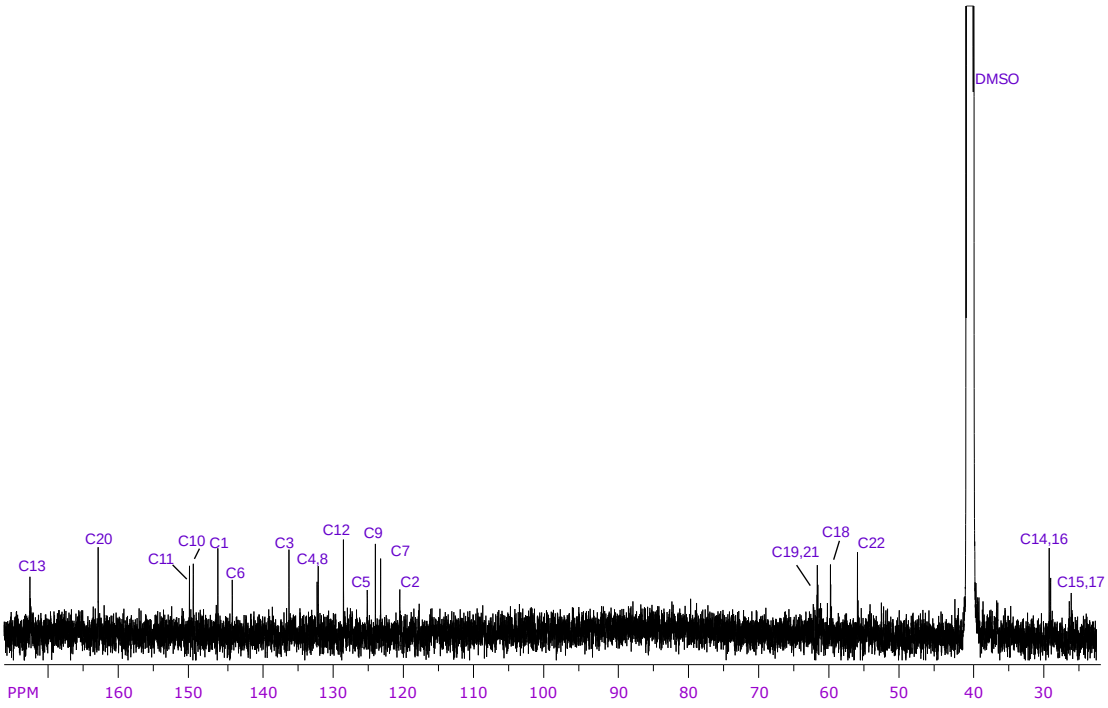

Figure 4.3.5: Fully assigned ^{13}C NMR spectrum of ligand L3.

The ^{13}C NMR spectrum highlights the wide range of carbon nuclei found within the ligand. Both the ^{1}H and ^{13}C NMR spectra confirm the successful synthesis and purity of ligand L3. The biotin portion of the ligand has chemical shifts which occur at lower frequencies between 1.20 ppm – 4.40 ppm in the ^{1}H NMR spectrum. The region of 1.20 to 2.40 ppm of the ^{1}H NMR spectrum of L3 is dominated by multiplet signals. These are ascribed to the numerous alkyl protons. These protons are present upfield due to the electron dense environments which shield the protons, resulting in a reduced effective magnetic field.

4.4 Uv/visible Spectroscopy

4.4.1 Introduction

UV/vis spectroscopy provides valuable information for compounds that have conjugated π systems. UV light has wavelengths ranging from 180 – 400 nm while visible light has wavelengths ranging from 380-780 nm. Both UV and visible light have sufficient energy to cause electronic transitions, promoting electrons from lower energy molecular orbitals (MOs) to higher energy MOs. The presence of electrons in the lowest energy MOs is referred to as the ground state electronic configuration. When a molecule absorbs light with an appropriate amount of energy, an electron is promoted to a higher energy MO. The molecule is now in the excited state. The absorption is detected and a spectrum is produced. Figure 4.4.1 shows the relative energies of antibonding, bonding and non-bonding MOs and the possible transitions.

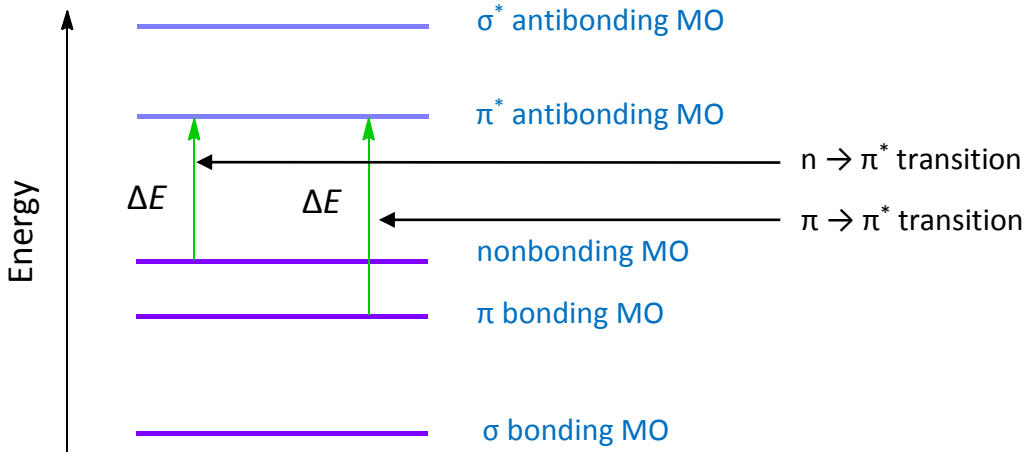

Figure 4.4.1: Relative energies of antibonding, bonding and non-bonding molecular orbitals showing possible electronic transitions.

Only two electronic transitions are commonly observed in UV/vis spectroscopy as shown in Figure 4.4.1. A non-bonding electron (n) promoted into a π^* antibonding MO is an electronic transition requiring a lower energy photon ($n \rightarrow \pi^*$ transition). An electron promoted from a π bonding MO into a π^* antibonding MO is an electronic transition of higher energy ($\pi \rightarrow \pi^*$ transition). Therefore only compounds that contain π electrons can absorb UV/visible radiation, generating a spectrum. In general the molar absorptivity of n-π^* transitions is significantly lower than that of π-π^* transitions.

Using the Beer-Lambert Law, $A = \varepsilon cl$, the molar absorptivity or molar extinction coefficient (ε) of a compound can be determined from a plot of absorbance versus concentration. The molar absorptivity is a constant that is characteristic of a compound at a given wavelength.

4.4.2 Results and Discussion

Absorption spectroscopy was used to investigate the electronic structure of all complexes within this study. UV/vis spectra for all complexes are available in Appendix A-3. The complex [Cu(L1)(Cl)] exhibits a high intensity peak at 228 nm which is attributed to a $\pi \rightarrow \pi^*$ transition (refer to Figure 4.4.2). The less intense peak at 420 nm is a metal-to-ligand charge transfer (MLCT) band. A superposition plot with [Cu(L1)(Phen-NH_2)](Cl), shows the same high intensity peak at 226 nm; similarly the result of $\pi \rightarrow \pi^*$transitions. However, at 287 nm an additional peak is noted as a result of $\pi \rightarrow \pi^*$ transition centered on the co-ligand 1,10-phenanthroline-5-amine. The MLCT transition at approximately 420 nm is largely unchanged in both spectra, confirming that both ligands have coordinated to the metal centre forming a heteroleptic complex.

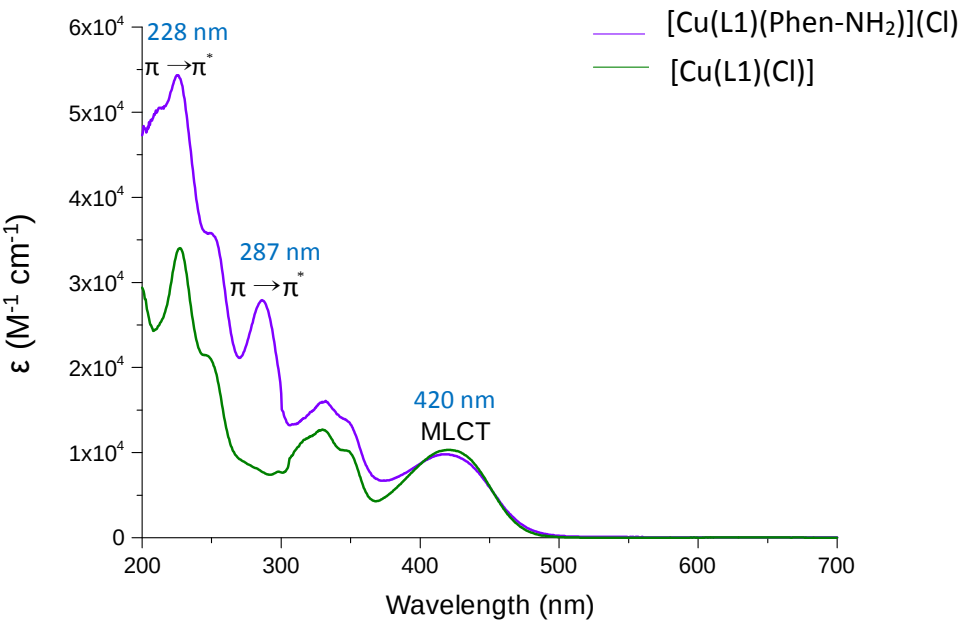

Figure 4.4.2: Overlay of the UV/visible spectra of [Cu(L1)(Cl)] (green) and [Cu(L1)(phen-NH_2)](Cl) (purple) highlighting the additional peak at 282 nm as a result of the phen-amine co-ligand. The peak at 228 nm is attributed to the Schiff base ligand.

An offset plot of [Cu(L1)(Cl)], [Cu(L1)(Bpy)](Cl) and [Cu(L1)(Phen)](Cl) illustrates that as the conjugation increases by adding the co-ligand 2,2'-bipyridyl to [Cu(L1)(Cl)], the spectra gains a $\pi \rightarrow \pi^*$ transition band between 260 - 300 nm. Substituting 2,2'-bipyridyl with 1,10-phenanthroline, shows that as conjugation of the co-ligand increases, an additional $\pi \rightarrow \pi^*$ transition between 240 -280 nm is observed. The MLCT band at approximately 420 nm is ubiquitous confirming that that the copper(II) metal centre is present in all cases and has a consistent coordination geometry.

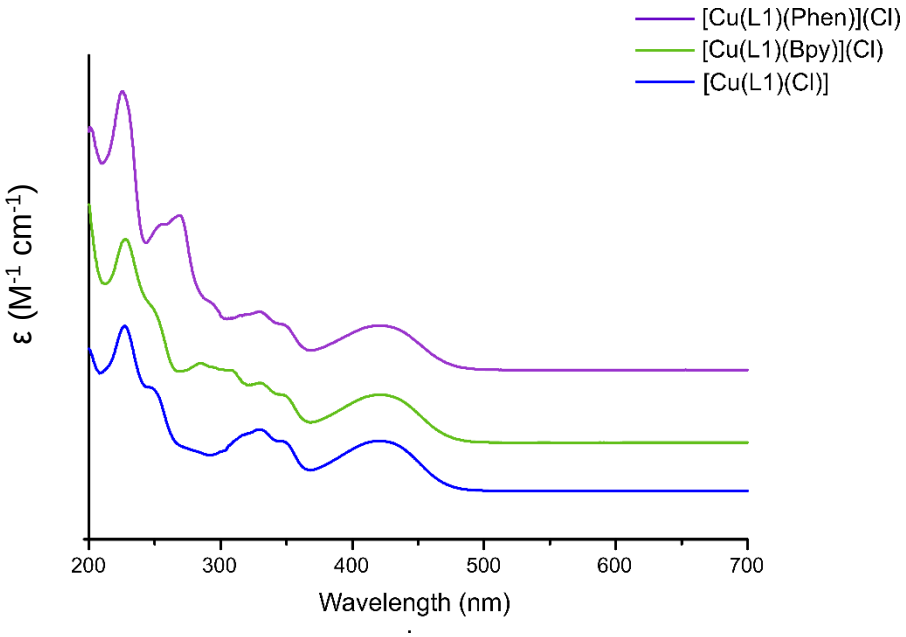

Figure 4.4.3: Offset overlay of [Cu(L1)(Cl)] (blue), [Cu(L1)(Bpy)](Cl) (green) and [Cu(L1)(Phen)](Cl) (purple) highlighting the influence of increased conjugation of the co-ligand on the UV-visible spectra.

Table 4.4.1 summarises the extinction coefficients at the corresponding wavelengths (λ_{max}) for the absorption bands for all copper(II) metal chelates reported in this study.

Table 4.4.1: A summary of the wavelengths (λ_{max}) and extinction coefficient (ε) for the copper(II) complexes.

Complex	λ_{max} / nm ε / M^{-1} cm^{-1}	λ_{max} / nm ε / M^{-1} cm^{1}	λ_{max} / nm ε / M^{-1} cm^{-1}	λ_{max} / nm ε / M^{-1} cm^{-1}
[Cu(L)(Cl)$_2$]	273 14 026	-	-	-
[Cu(L1)(Cl)]	228 34 040	330 12 710	420 10 342	-
[Cu(L2)(Cl)$_2$]	232 17 991	354 46 402	369 19 117	-
[Cu(L1)(Bpy)](Cl)	228 42 595	283 17 308	330 12 429	420 9 977
[Cu(L1)(Phen)](Cl)	226 67 497	269 37 222	330 13 970	420 10 751
[Cu(L1)(Phen-NH$_2$)](Cl)	226 54 180	250 35 670	332 15 982	418 9 733

4.5 DNA Binding Studies

4.5.1 Introduction

Deoxyribonucleic acid (DNA) is a crucial genetic biomolecule which encompasses all genetic information for the development and functioning of living organisms. Its ability to carry hereditary information as well as aid in the synthesis of enzymes and proteins highlights its significance as a biomolecule. It thus has become a vital cellular target for antiviral, antibacterial and anti-cancer drugs.[52] The interaction of transition metals such as copper with DNA have been under investigation for decades acting as structural probes and chemotherapeutic agents.[53] The copper(II) complexes in this study are predicted to exert their cytotoxicity through DNA binding and hydroxyl radical-induced DNA cleavage. Previous research suggests that this class of complexes bind to the DNA *via* two distinctive modes. Firstly, by hydrophobic interactions in DNA's minor groove followed by partial intercalation of the co-ligand into the major groove.[22]

DNA interactions with drugs have been investigated widely through numerous techniques such as DNA melting curves, viscosity measurements, gel electrophoresis, molecular docking, UV/vis spectroscopic methods and fluorescence measurements.[54] In this study, the technique of fluorescence competitive DNA binding titrations was used to determine the apparent binding affinity of the copper(II) complexes to calf thymus DNA (ctDNA).

Ethidium bromide (EB) is a planar, aromatic dye which readily intercalates between the base pairs of ctDNA. It is used as a fluorescent probe to investigate the competitive binding properties of other compounds with ctDNA. EB and ctDNA both have weak fluorescence properties, however, once the EB has intercalated the DNA the EB-ctDNA complex produces strong fluorescence emission. The conjugate exhibits an intense peak at approximately 614 nm in the emission spectrum after excitation at 500 nm. The increased emission intensity of the EB/DNA conjugate compared to either free species is attributed to two factors. Firstly, ctDNA's nucleic acids absorb UV light at 260 nm and then transfer this energy to EB. Secondly, when intercalated EB absorbs energy in the range of 300-360 nm. This energy excites EB to emit fluorescence with a wavelength of 587 nm.[54] The addition of a second DNA intercalator (in this case the copper(II) chelate) will quench the fluorescence emission of EB/ctDNA conjugate by replacing the EB in the double helix of the DNA molecule.

In the course of the DNA titrations, the EB is displaced by the copper(II) chelate. Therefore, the binding affinity of the EB must be determined to calculate the binding constant of the metal complex. The binding constant of the EB is determined *via* direct UV/vis spectroscopic titrations which involve monitoring the decrease in absorption of EB in solution as a function of ctDNA concentration. A decrease in the intensity of the EB absorption band in the 650-350 nm region is indicative of DNA intercalation as the intercalation reduces the effective concentration of the EB, reducing the absorbance. Compounds with an apparent binding constant (K_{app}) higher than the binding constant of EB would generally be regarded as effective DNA intercalators.

4.5.2 Experimental

The ctDNA utilised for both the direct and competitive DNA binding studies was purchased from Sigma Aldrich as the highly polymerised sodium salt and was used to prepare a ctDNA stock solution in 25 mM Tris-HCl buffer. The buffer was prepared with ultrapure water (resistivity = 18 MΩ) and adjusted to a pH of 7.0 using 1 M HCl. The exact concentration of the ctDNA stock solution was determined using the Beer-Lambert law by measuring the absorption at 260 nm and using the extinction coefficient of 13 200 M^{-1} cm^{-1}.

The EB stock solution used in the DNA titrations had a concentration of 9.60×10^{-5} M in TrisHCl buffer (pH 7.0) solution at 25 ^{o}C in a 1.0 cm path length quartz cuvette. The ctDNA stock solution (2.79×10^{-3} M concentration) was added to the EB solution in small aliquots followed by a ten minute incubation period after each addition. This incubation period was to ensure that the intercalation process was complete and equilibrium was established before the spectra were recorded. The absorption spectra were recorded in the range 800-200 nm.[55] The following equation was used to determine the DNA binding constant of EB:

Equation 4.5.1:

$$\left(\frac{\varepsilon_a - \varepsilon_f}{\varepsilon_b - \varepsilon_f}\right) = \left(b - \left(\frac{b^2 - 2K_b^2 C_t[DNA]}{s}\right)^{\frac{1}{2}}\right)/2K_b C_t$$

Where

$$b = 1 + K_b C_t + \frac{K_b[DNA]}{2s}$$

ε_a = Extinction coefficient of EB band at given [ctDNA]

ε_f = Extinction coefficient of free EB

ε_b = Extinction coefficient of fully intercalated EB

K_b = Equilibrium constant in M^{-1}

C_t = Total Concentration of ctDNA

s = Binding site size (number of nucleotides per EB)

The competitive binding studies to determine the binding affinities of the metal chelates were performed as follows. Aliquots of copper(II) chelate stock solutions (concentration range 1.42 – 1.90 mM dissolved in ultra pure water) were added to a solution containing 15 µM ctDNA and 15 µM EB in 25 mM Tris-HCl Buffer at ten minute intervals and the solution emission spectra were then recorded. The samples were excited at 500 nm and the emission was recorded between 530 and 800 nm. The apparent binding constant, K_{app}, for each metal chelate was calculated using Equation 4.5.2.

Equation 4.5.2:

$$K_{app}[Complex] = K_{EB}[EB]$$

Where:

K_{EB} = ctDNA binding constant of EB

[EB] = EB molar concentration

[Complex] = Concentration of the chelate that caused a 50% reduction in the initial fluorescence intensity

The quenching of the EB-ctDNA fluorescence can be confirmed by a plot fitted with the linear Stern-Volmer equation:

Equation 4.5.3:

$$I_0/I = 1 + kr$$

Where:

I_o = Emission intensity of EB-ctDNA complex

I = Emission intensity of the quenched EB-ctDNA complex

r = ratio of total concentration of metal chelate to DNA concentration

k = Stern Volmer constant

4.5.3 Results and Discussion

Competitive DNA binding studies were carried out on ctDNA by varying the concentrations of the copper(II) chelates and monitoring the impact on emission intensity. The enhanced fluorescence of the EB-ctDNA complex is quenched by the addition of the metal chelate which replaces the EB, thus causing a diminishing emission intensity of the solution. All six complexes within this study showed the characteristic quenching of the EB-ctDNA solution; indicative of DNA binding. As a representative example, [Cu(L1)(Phen-NH_2)](Cl) will be discussed in detail. The emission spectra as well as the Stern-Volmer plots of the remaining complexes are available in Appendix A-4.

To calculate K_{app} from Equation 4.5.2, the binding constant of EB (K_{EB}) to ctDNA is required. This was determined in an independent study by performing a direct DNA titration with EB and ctDNA. EB's decreasing absorbance (hypochroism) as well as the bathochromic shift of the absorption band with increasing concentration of ctDNA is indicative of intercalation between the base pairs of the DNA double helix.[55]

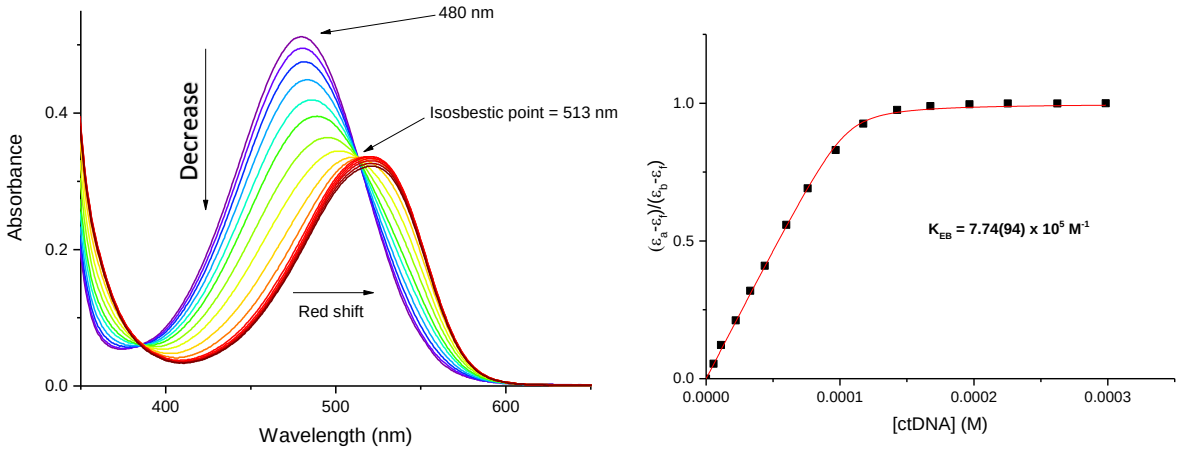

Figure 4.5.1: (Left) Absorption spectra of EB in the presence of increasing concentrations of ctDNA. (Right) Non-linear fit of EB titration with ctDNA at 480 nm to determine K_{EB}.

The absorption spectra in Figure 4.5.1 illustrate the hypochromic and the bathochromic shifts which are characteristic of the DNA intercalation process.[55] The ethidium bromide binding constant (K_{EB}) was determined using Equation 4.5.4 to be 7.74 × 10^5 M^{-1}.The fluorescence quenching of the EB/ctDNA conjugate by the metal chelates confirm that the metal chelates displace the EB, indicating DNA binding.

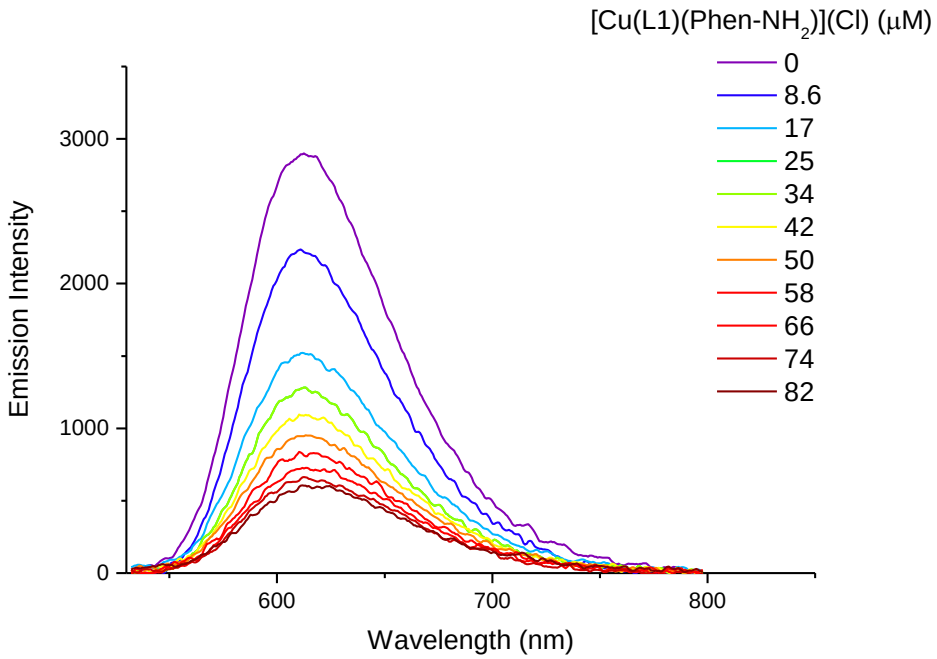

Figure 4.5.2: Decreasing emission intensity caused by the displacement of DNA-intercalated EB by [Cu(L1)(Phen-NH_2)](Cl).

Figure 4.5.2 shows that the copper(II) complexes compete with EB for binding sites on the ctDNA helix and displace the strongly intercalated EB; this proves DNA binding. Equation 4.5.2 was used to determine the apparent binding constant (K_{app}) for each of the metal chelates. The complex concentration (3.38×10^{-5} M) at which a 50% reduction of the fluorescence intensity of EB occurred was determined by a non-linear fit of the change in emission intensity at 611 nm as a function of increasing chelate concentration. Figure 4.5.3 shows both the non-linear as well as the Stern-Volmer plots.

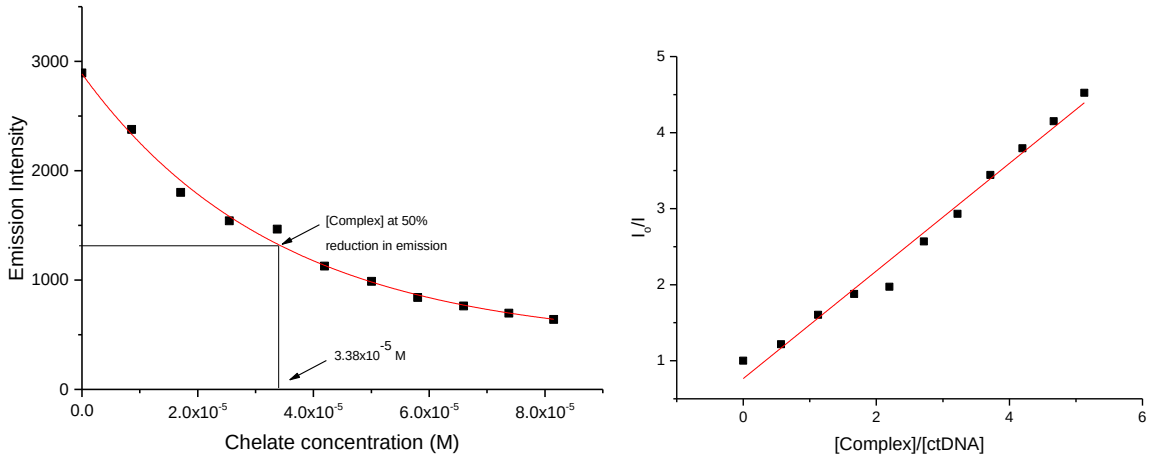

Figure 4.5.3: (Left) Least-squares fit of the emission intensity at 611 nm with increasing metal chelate concentration. (Right) Stern-Volmer plot for [Cu(L1)(Phen-NH_2)](Cl).

The K_{app} values for the remaining metal chelates are summarised in Table 4.5.1. EB is considered to be a strong DNA intercalator (binding constant of 7.74×10^5 M^{-1}) and a comparison of the copper(II) chelates with EB, suggests that the chelates presented in this study have a similarly high ctDNA binding affinity.

Table 4.5.1: Summary of K_{app} values for the copper(II) chelates determined by competitive DNA binding studies.

Compound	K_{app} ($\times 10^5$ M^{-1})
[Cu(L1)(Cl)]	8.7(2)
[Cu(L1)(Bpy)](Cl)	2.9(2)
[Cu(L1)(Phen)](Cl)	3.5(2)
[Cu(L1)(Phen-NH_2)](Cl)	3.4(2)
[Cu(L2)(Cl_2)]	1.2(2)
[Cu(L)(Cl_2)]	1.8(2)

The data in Table 4.5.1 clearly show there is a relationship between the structure of the copper(II) chelates and their DNA binding affinity. [Cu(L1)(Cl)] has the highest apparent binding constant due to the planar nature of the complex, aiding in it's ability to bind to the ctDNA. This complex is used as the building block in the heteroleptic complexes; its high binding affinity shows that it is an ideal choice for this purpose. A decrease in binding constants is noted for the three heteroleptic complexes [Cu(L1)(Bpy)](Cl), [Cu(L1)(Phen)](Cl) and [Cu(L1)(Phen-NH_2)](Cl) as was expected, due to the added co-ligand hindering the intercalation process. Even though a decrease in the binding affinity is observed, the binding constants are still of the same order of magnitude as EB; an encouraging result.

Taking a closer look at only the three heteroleptic complexes, predicted binding patterns were confirmed. As the ring number on the co-ligand increases from [Cu(L1)(Bpy)](Cl) to [Cu(L1)(Phen)](Cl), an increase in the DNA binding constant is observed. The greater the extended aromaticity, the more efficiently a complex is able to interact with the aromatic base pairs of the DNA helix. Additional aromaticity leads to favourable π···π interactions between the chelates and the aromatic DNA base pairs. These attractive forces increase the stability of the DNA/drug conjugate which manifests as a higher DNA binding constant.

The binding constants of both phenanthroline-based complexes are comparable, suggesting that the added NH_2 group has no significant role in DNA interactions. This is an unexpected result as the hydrogen bonding ability of the NH_2 group is expected to further stabilise the DNA/drug conjugate. [Cu(L2)(Cl_2)] and [Cu(L)(Cl_2)] contain *N,N'N''* donor atom sets and possess the lowest binding constants. X-ray crystallography of [Cu(L2)(Cl_2)] (*vida infra*) shows the complex to be in a square pyramidal geometry with one chloride ion approximately perpendicular to the rest of the complex. The position of this chloride ion diminishes the planarity of the complex thus decreasing its ability to effectively interact with the DNA helix. As it has been shown that the planarity of the co-ligands has an influence on the DNA binding affinity, increasing this factor could have favourable results. This could be achieved using ligands such as DPQ and DPPZ. It is also important to note that DNA binding is more complex than mere planarity of the complexes. The majority of the chelates developed in this study carry an overall positive charge. This serves to stabilise the DNA/drug conjugate through favourable electrostatic interactions with the negatively charged phosphate backbone of the DNA helix. The lipophilicity of the complex can also play a role in DNA binding as more

lipophilic complexes interact more strongly with the lipophilic core of the DNA helix.[40] This could explain why the more polar [Cu(L1)(Phen-NH2)](Cl) complex had a lower binding affinity than [Cu(L1)(Phen)](Cl).

Table 4.5.2 summarises the K_{app} values of comparable previously reported copper(II) chelates.

Table 4.5.2: Structures and K_{app} values of previously reported copper(II) chelates and complexes of this study.

Complexes from literature	K_{app} (M^{-1})	Complexes from this study	K_{app} (M^{-1})
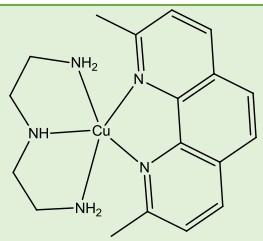 Ganeshpandian, *et al.*[39]	2.05×10^5	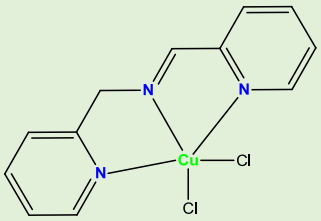	$1.8(2) \times 10^5$
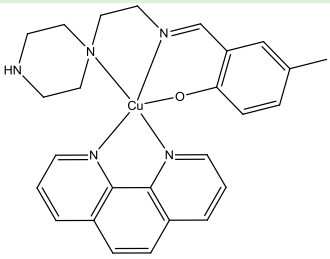 Ravichandran, *et al.*[38]	3.63×10^4	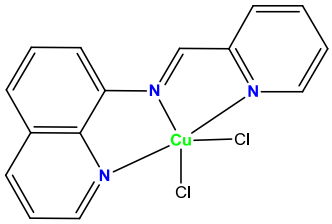	$1.2(2) \times 10^5$
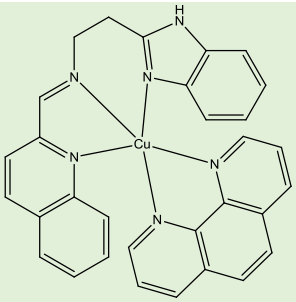 Rajarajeswari, *et al.*[56]	3.00×10^4	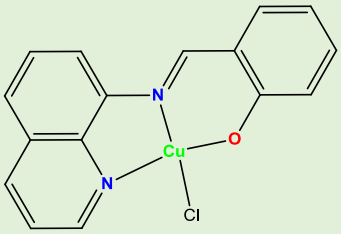	$8.7(2) \times 10^5$
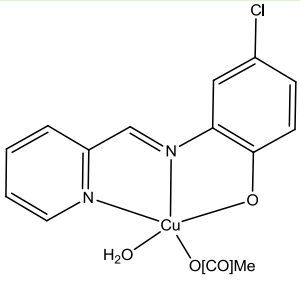 Qiao, *et al.*[36]	6.40×10^5	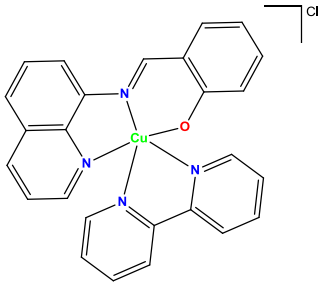	$2.9(2) \times 10^5$

Table 5.4.2 continued…

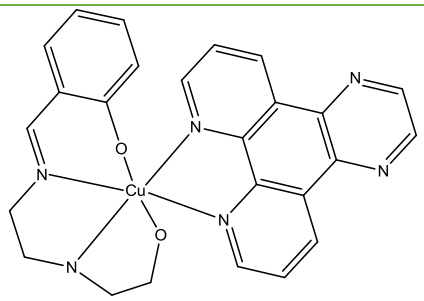 Rajendiran, *et al*.[57]	2.50×10^6	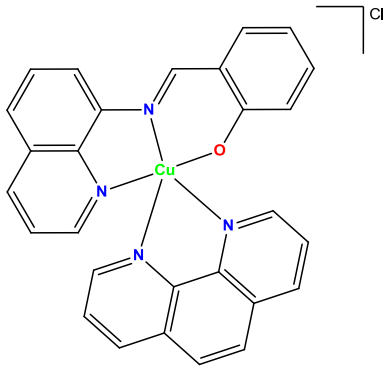	$3.5(2) \times 10^5$
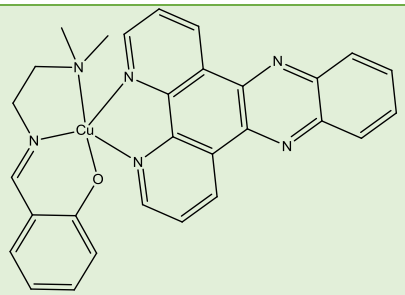 Jaividhya, *et al*.[58]	3.90×10^5	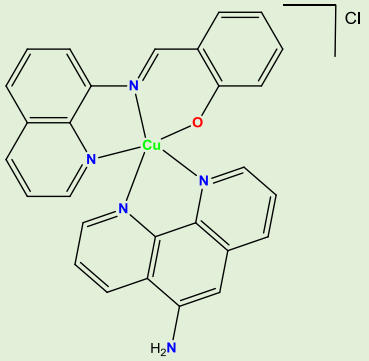	3.43×10^5

There are a number of structural similarities between the copper(II) chelates in Table 4.5.2 and those in this work. Firstly, the donor atoms are either *N,N',N''* or *N,N',O* and secondly, similar co-ligands were used. The copper(II) chelates in the studies of Ganeshpandian, *et al.*[39], Ravichandran, *et al*.[38] and Rajarajeswari, *et al*.[56] have 1,10-phenanthroline-based co-ligands and the K_{app} values are lower than that of [Cu(L1)(Phen)](Cl). The copper(II) chelate by Qiao, *et al*.[36] contains *N,N',O* donor atoms, is a single-ligand chelate and is comparable to [Cu(L1)(Cl)]. The K_{app} of 6.40×10^5 M^{-1} is comparable, though slightly lower, than that of [Cu(L1)(Cl)] which was measured to be 8.65×10^5 M^{-1}. The copper(II) chelates by Rajendiran, *et al*.[57] and Jaividhya, *et al*.[58] have DPQ and DPPZ co-ligands, respectively. These copper(II) chelates have high binding affinities compared to the other reported structures and those of this work. Increasing the aromaticity of the co-ligand seemingly plays a significant role in the interactions with the DNA helix leading to increased binding affinities. The table highlights that varying the donor atoms and changing the co-ligand can have a significant influence on the

interactions of the chelates with DNA. The link between ctDNA binding constants and cytotoxicity will be explored in Chapter 6.

4.6 Hydroxyl Radical Assay

4.6.1 Introduction

One of the key attributes of copper toxicity comes from its ability to participate in oxidation and reduction reactions and therefore catalyse the formation of reactive oxygen species (ROS) in a biological environment. In the presence of reducing agents, such as ascorbic acid, Cu^{2+} is reduced to Cu^{+} which can generate hydroxyl radicals from hydrogen peroxide *via* the Haber-Weiss reaction.[59] Scheme 4.6.1 shows the production of hydroxyl radicals catalysed by copper(II) which induce DNA cleavage.

$$HS\text{-}R\text{-}S^{-} + Cu^{2+} \rightarrow HS\text{-}R\text{-}S^{\cdot} + Cu^{+}$$

$$HS\text{-}R\text{-}S^{\cdot} + O_2 \rightarrow S\text{-}S\text{-}R + H^{+} + O_2^{-\cdot}$$

$$2O_2^{-\cdot} + 2H^{+} \rightarrow H_2O_2 + O_2$$

$$Cu^{+} + H_2O_2 \rightarrow OH^{\cdot} + OH^{-} + Cu^{2+}$$

$$OH^{\cdot} + DNA \rightarrow Fragments$$

Scheme 4.6.1: The reaction equations for the formation of hydroxyl radicals for DNA degradation catalysed by copper(II).

Hydroxyl radicals are one of the most powerful oxidising agents found in biological systems. Oxidative damage can occur when OH· abstracts an electron from an amino-bearing carbon, producing a carbon-centered protein radical or from unsaturated fatty acids to form a lipid radical. The electron deficient radicals can also attack the aromatic DNA base pairs, inducing single and double-stranded DNA cleavage.[59] The process for the generation of ROS leading to DNA cleavage is depicted in Figure 1.3.2 in the introduction.

To investigate this process, hydroxyl radical assays were carried out using Rhodamine B dye (Figure 4.6.1) which acts as spectrophotometric indicator. Rhodamine B is highly conjugated with four *N*-ethyl groups at either side of the xanthene ring system. As the electron deficient radicals are produced, they attack the electron-rich π-system of the dye causing degradation. The loss of extended conjugation in the dye leads to a decrease in the intensity of the

absorption of rhodamine B. Rhodamine B therefore acts as an analogue of the electron-rich DNA base pairs which will be equally susceptible to attack by the hydroxyl radicals.[60]

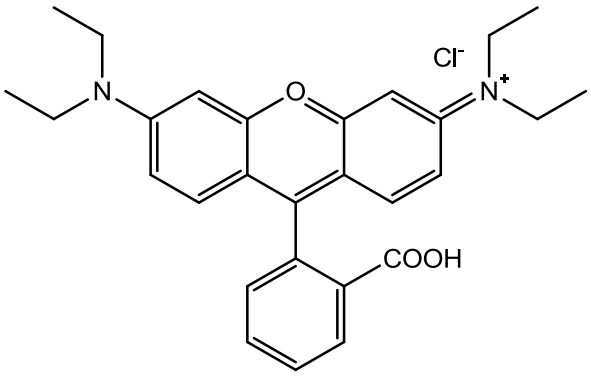

Figure 4.6.1: Chemical structure of Rhodamine B dye.[15]

4.6.2 Experimental

To generate the hydroxyl radicals a number of cellular reagents are required; Table 4.6.1 shows the required stock solutions with the respective concentrations used in the hydroxyl radical assay. Sodium ascorbate is used to represent the thiols present in the human body. Hydrogen peroxide is also present in cells as a result of various cellular processes.[61]

Table 4.6.1: Concentrations of stock solutions used for the hydroxyl radical assay.

Stock solution	Concentration (M)
Rhodamine B	3.60×10^{-5}
Metal Chelate	$1.44 – 1.89 \times 10^{-3}$
Hydrogen peroxide	2.70×10^{-2}
Sodium ascorbate	2.61×10^{-3}

4.6.3 Results and Discussion

A hydroxyl radical assay was conducted on all copper(II) chelates to determine whether the complexes can generate hydroxyl radicals (which have the ability to damage DNA) under pseudo cellular conditions. The graph in Figure 4.6.2 illustrates the kinetic traces for [Cu(L1)(Bpy)](Cl) along with a control run using distilled water. This is a representative example of the bulk of the metal chelates. The control run was used to prove that in the

absence of a copper(II) chelate, the reagents alone do not produce hydroxyl radicals. This was confirmed by the kinetic graph for water which remains constant throughout the kinetic scan.

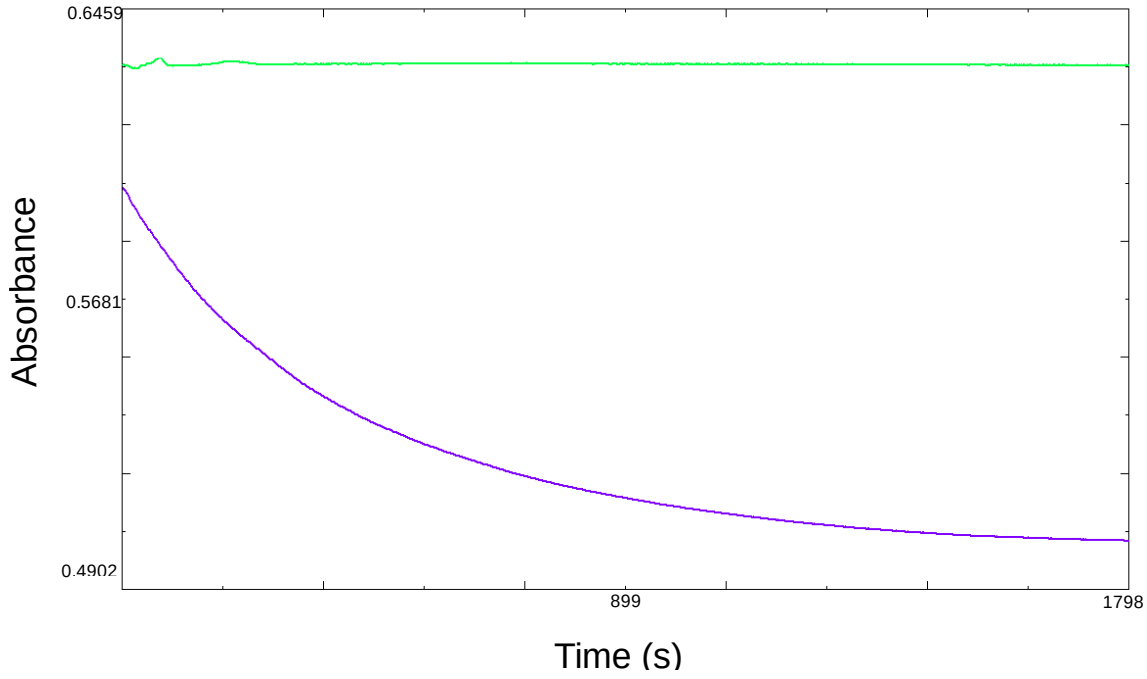

Figure 4.6.2: Kinetic curve of [Cu(L1)(Bpy)](Cl) illustraing the decrease in absorbance of rhodamine B at 553 nm. This decrease in absorbance is a result of degradation of the dye by hydroxyl radicals.

All six metal chelates showed a similar decreasing absorbance at 553 nm, indicative of the production of hydroxyl radicals and decay of the dye. This assay confirms that the copper(II) chelates catalyse the production of hydroxyl radicals. This same process is likely a vital step in the cytotoxicity of the copper(II) chelates (*vida infra*).

Chapter 5 | X-Ray Crystallography

5.1 Introduction

5.1.1 General

Single crystal X-ray diffraction experiments were utilised to investigate the solid state structures of the copper(II) chelates synthesised in this study. These experiments will provide valuable information on the solid state interactions of the chelates and contribute to the current body of knowledge regarding single-ligand and heteroleptic copper(II) chelate crystal data. A survey of the Cambridge Structural Database[62] (CSD) showed X-ray structures of similar chelates to those presented in this work. These will be briefly reviewed as an introduction to this chapter followed by a discussion of the experimental X-ray data obtained in this study.

5.1.2 Previously reported Schiff base ligand

Condensation of 8-aminoquinoline with salicylaldehyde affords 2-*N*-(quinoline-8-yl)iminomethylphenol (HL1) which is the *N,N',O* Schiff base ligand used as the primary ligand in the heteroleptic complexes in this work. HL1 has been previously synthesised, characterised and coordinated to a range of various transition metals including zinc, cobalt, iron and silicon.[63, 64, 65, 66] A search of the CSD showed the crystal structure of the free ligand has been elucidated. NEZQAL (CSD Reference code for ligand structure) contains four molecules is the unit cell and crystallises in the monoclinic space group $P2_1/n$. The asymmetric unit is shown in Figure 5.1.

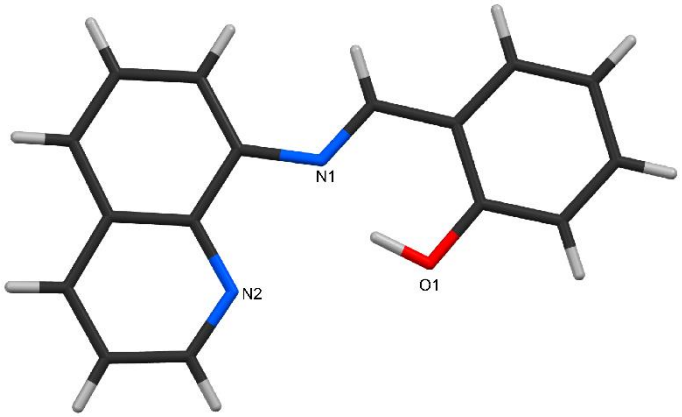

Figure 5.1: Partially labelled X-ray crystal structure of NEZQAL.[66]

The structure of NEZQAL shows that the quinoline heterocyclic ring system is almost coplanar with the π-ring system of the salicylideneimine moiety (the salicylic ring system including the imine bond). The angle between the two mean planes measures 3.81(1)°. Figure 5.2 shows the planes of the two moieties.[66]

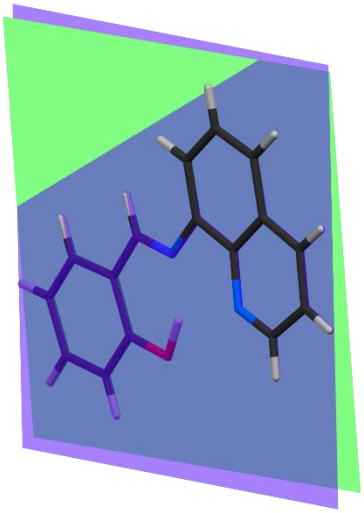

Figure 5.2: Mean planes of the quinoxaline and salicylide moieties showing the almost coplanar nature of the ligand NEZQAL. The quinoline ring system lies in the purple plane, while the salicylic ring system lies in the green plane.[66]

NEZQAL exhibits a bifurcated intramolecular hydrogen bond with the phenolic OH acting as a hydrogen bond donor to both the imine and quinoxaline nitrogen atoms (hydrogen bond acceptors).[66] This is shown in Figure 5.3 (a) below. The hydrogen bond parameters are summarised in Table 5.1. The lattice is stabilised by π···π interactions between the aromatic phenol and quinoxaline moieties of adjacent molecules. This leads to a one-dimensional column co-linear with the *b*-axis Figure 5.3 (b).[66]

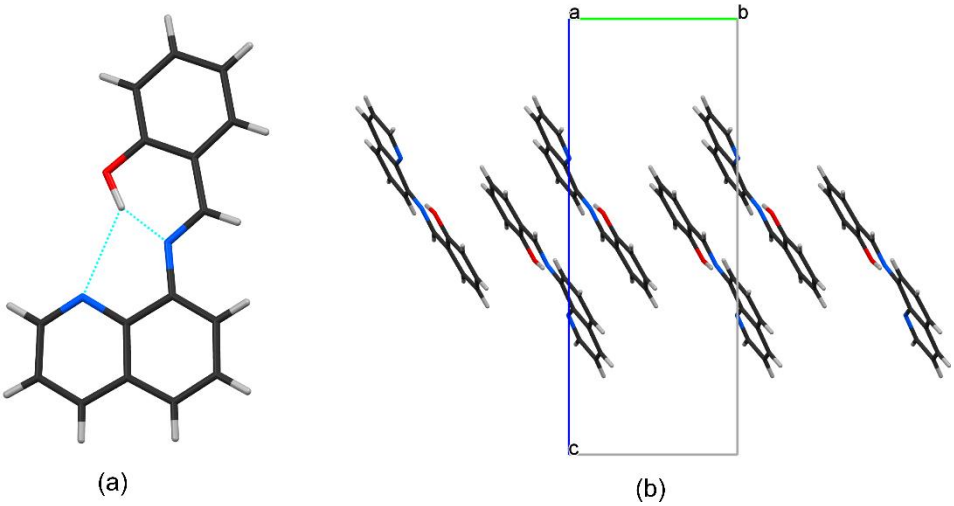

Figure 5.3: (a) Bifurcated hydrogen bonding exhibited by NEZQAL in the solid state. (b) One-dimensional π-stacked columns of NEZQAL viewed down the *a*-axis.[66]

Table 5.1: Hydrogen bond parameters (Å, °) of NEZQAL.[66]

Hydrogen Bond	D–H	H···A	D···A	D–H···A
O–H···N$_{imine}$	1.01(2)	1.59(2)	2.526(2)	152(1)
O–H···N$_{quinoxaline}$	1.01(2)	2.59(2)	3.356(2)	133(1)

The π-stacked columns are cross-linked by weak C–H···π interactions. This leads to a herringbone pattern in the crystal lattice. This packing pattern is illustrated in Figure 5.4.

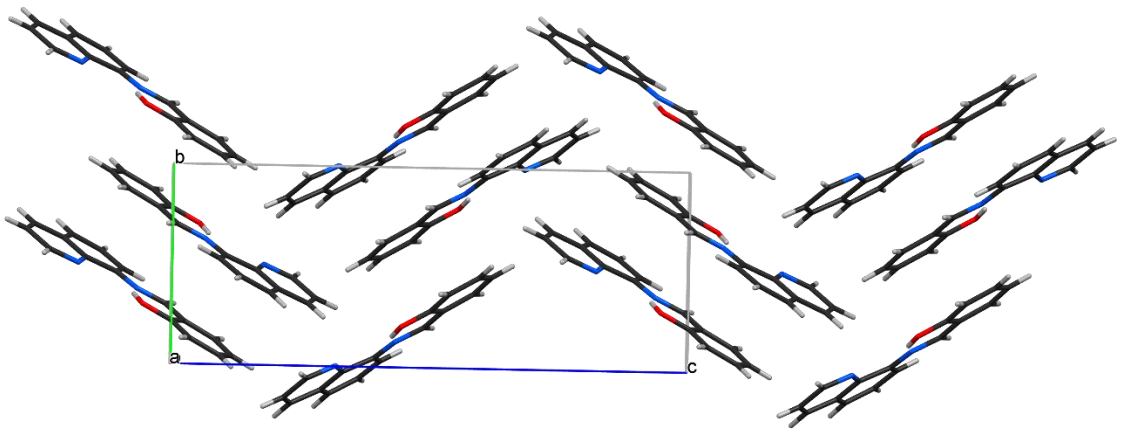

Figure 5.4: Herringbone pattern of NEZQAL viewed down the a-axis. This supramolecular structure is stabilised by both π···π interactions and C–H···π interactions.[66]

5.1.3 Previously reported copper chelates

In this study a total of six copper(II) metal chelates were synthesised, of which three were heteroleptic and three were single-ligand complexes. From the synthesised complexes, six crystal structures were obtained encompassing five of the metal chelates. One complex, [Cu(L2)(Cl)$_2$], was isolated as two pseudo-polymorph crystals. A search of the CSD[62] showed numerous metal chelates which are structurally comparable to those of this study. A selection of the most pertinent structures will be discussed within this chapter. Table 5.2 provides a summary of relevant metal chelates followed by Figure 5.5 which shows the structures of the chelates listed in Table 5.2.

Table 5.2: Previously reported X-ray crystal structures of relevant metal chelates.

CSD Ref. Code	Compound Name	Lit. Reference
CIMMOB	(*E*)-2-methyl-N-((6-methylpyridin-2-yl)methylene) quinolin-8-amine]dichloronickel(II)	67
CIMMUH	[2-*i*-Pr-*N*-((6-methylpyridin-2-yl)methylene)quinolin-8-amine]dichloronickel(II)	67
MEHGAJ	(*E*)-2-*tert*-butyl-6[(quinoline-8-ylimino)methyl] phenolate-titanium(III)	68
QITROB	(*E*)-1-(pyridin-2-yl)-*N*-(pyridin-2-ylmethylene) methanamine-zinc(II)	69

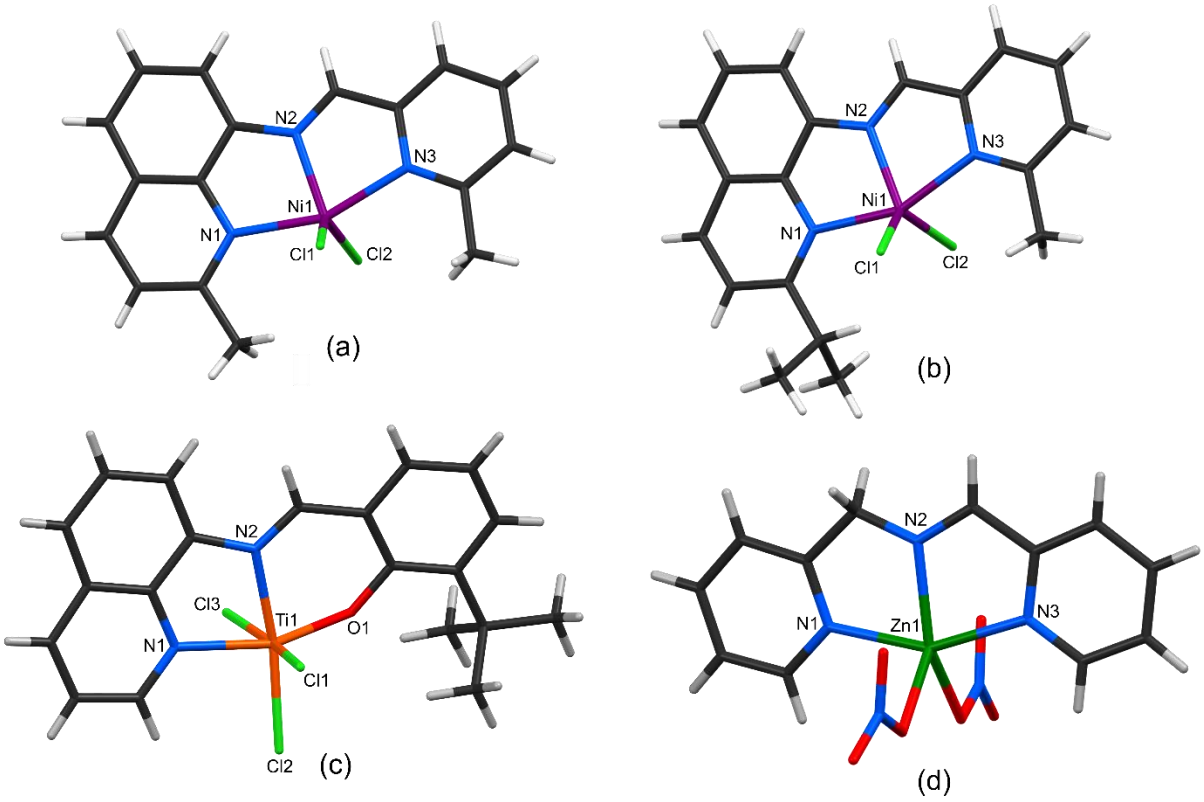

Figure 5.5: X-ray crystal structures of (a) CIMMOB[67], (b) CIMMUH[67], (c) MEHGAJ[68] and (d) QITROB[69].

The chelates CIMMOB[67] and CIMMUH[67] both comprise derivatives of ligand L1 with methyl and isopropyl substituents, respectively. The ligands have been coordinated to nickel(II) chloride; both chelates display a distorted trigonal-bipyramidal geometries. MEHGAJ[68] contains a titanium metal centre bonded to the tridentate ligand (a derivative of HL1) through two neutral nitrogen atoms and an anionic phenolic oxygen atom. The remaining three coordination sites are occupied by chloride ligands resulting in distorted octahedral geometry.

QITROB[69] is coordinated to zinc(II) and displays a square-pyramidal geometry. The ligand of QITROB is structurally similar the single-ligand chelate $[Cu(L)(Cl)_2]$ of this work.

The average bond lengths and angles for these reported complexes are given in Table 5.3 where the letter 'M' represents the different metal centres for the reported complexes. As expected, all bond lengths are comparable with only a slight deviation in the $C=N_{imine}$ bond length of QITROB, which is slightly longer than the rest. Bond angles also lie within a reasonable range of each other. However, the bond angle for N2-M-O1 of MEHGAJ is larger than the corresponding N2-M-N3 angle of the other three reported structures. This can be attributed to the latter forming a six-membered chelation ring as opposed to the five membered rings formed in the former.

Table 5.3: Average bond lengths and bond angles for previously reported metal chelates where M represents metal centre.

	CIMMOB	**CIMMUH**	**MEHGAJ**	**QITROB**
		Bond Length (Å)		
N1 - M	2.110(4)	2.147(2)	2.191(5)	2.116(2)
N2 - M	1.982(3)	2.000(3)	2.168(5)	2.085(3)
N3 - M	2.132(4)	2.167(3)	-	2.108(2)
C = N_{imine}	1.274(5)	1.279(4)	1.300(8)	1.366(3)
O1 - M	-	-	1.797(4)	-
		Bond Angles (°)		
N1 - M - N2	79.7(1)	79.0(1)	74.6(2)	76.93(7)
N2 - M - N3	78.5(1)	78.4(1)	-	77.16(8)
N2 - M - O1	-	-	84.1(2)	-

A wide range of heteroleptic metal chelates with either the same or slight variations in the co-ligands have also been reported. The most relevant structures will be further discussed in detail. A common characteristic in the following structures is the *N,N',O* donor atoms on the primary ligand which is in keeping with the heteroleptic complexes of this study. Variations of the structures in Figure 5.6 include functionalisation of the primary ligands containing *N,N',O* donor atoms, as well as an increase in the number of rings of the co-ligands. Table 5.4 provides a summary of the relevant chelates.

Table 5.4: Reported X-ray structures of most relevant copper(II) chelates.

CSD Ref. Code	Compound Name	Lit. Reference
DAYMUN	Aqua-(1,10-phenanthroline)-(*N*'-(pyridin-2-ylmethylidene)benzohydrazide)-copper(II) dinitrate	[70]
DAYNAU	Aqua-(2,2'-bipyridine)-(*N*'-(pyridin-2-ylmethylidene)benzohydrazide)-copper(II) nitrate perchlorate monohydrate	[70]
KUPDEF	(2,4-Di-*t-butyl*-6-((((pyridin-2-yl)methyl)imino)methyl)phenolato)-(pyrazino[2,3-f][1,10]phenanthroline)-copper(II) perchlorate	[71]
NOYHAM	(2,4-bis(2-Phenylpropan-2-yl)-6-(((quinolin-8-yl)imino)methyl)phenolato)-(dipyrido[3,2-a:2',3'-c]phenazine)-copper(II) perchlorate	[72]
NOYHIU	(2,4-Di-*t-butyl*-6-(((quinolin-8-yl)imino)methyl)phenolato)-(pyrazino[2,3-f][1,10]phenanthroline)-copper(II) perchlorate	[72]
NOYHOA	(1,10-Phenanthroline)-(2-(((quinolin-8-yl)imino)methyl)phenolato)-copper(II) perchlorate	[72]
QEFCOV	(2,2'-Bipyridine)-(2-(((2-(dimethylamino)ethyl)imino)methyl)phenolato)-copper(II) perchlorate	[73]
QEFCUB	(2,2'-Bipyridine)-(2-(((2-(dimethylamino)ethyl)imino)methyl)-4-methoxyphenolato)-copper(II) perchlorate	[73]
QEFDAI	(2,2'-Bipyridine)-(4-methoxy-2-(((quinolin-8-yl)imino)methyl)phenolato)-copper(II) perchlorate	[73]

Closely related copper chelates such as DAYMUN[70], DAYNAU[70], KUPDEF[71], QEFCOV[73] and QEFCUB[73] all contain *N,N',O* donor atoms, with similar co-ligands to those of this study. These complexes, however, display variation in the geometry around the metal centre. Figure 5.6 show the solid state structures for the closely related copper chelates.

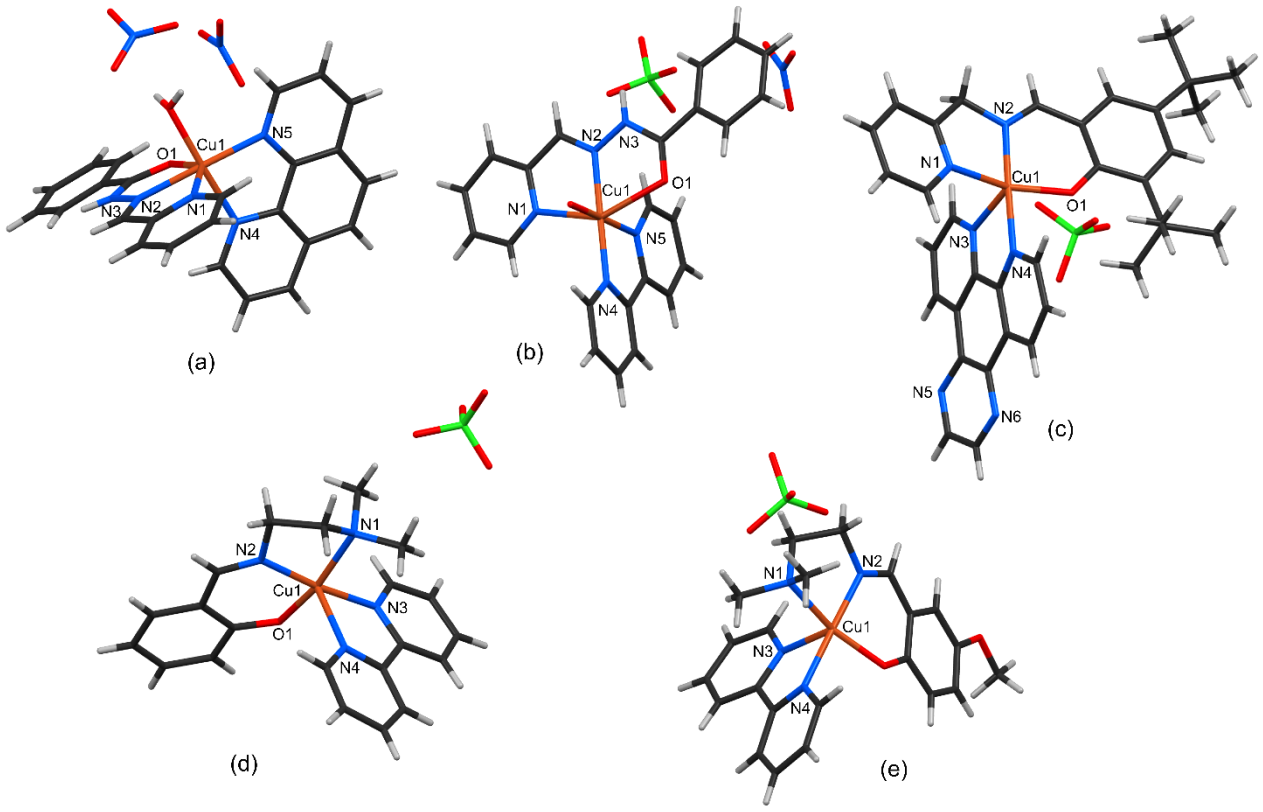

Figure 5.6: X-ray crystal structures of the heteroleptic copper(II) chelates(a) DAYMUN[70], (b) DAYNAU[70] (c) KUPDEF[71], (d) QEFCOV[73] and (e) QEFCUB[73].

The coordination geometry around the copper centres of both DAYMUN and DAYNAU can be described as a distorted octahedron while KUPDEF exhibits a square pyramidal geometry. QEFCOV and QEFCUB both consist a penta-coordinated complex, similarly displaying a distorted square pyramidal geometry.

Looking more closely at DAYMUN and DAYNAU, each complex shows a single neutral tridentate ligand which is coordinated meridonial with the remaining three coordination sites occupied by a bidentate ligand (Phen and Bpy, respectively) and a monodentate aqua ligand. The Cu-N bond distances in DAYMUN (average 2.0976 Å) lie within good correlation with the Cu-N distances for other closely related copper(II) complexes.[70, 74] Conventional hydrogen bonding is observed for these structures where O-H···O and N-H···O intramolecular and intermolecular hydrogen bonding stabilise the complex supramolecular structures.[70]

The geometry of the metal chelate KUPDEF is square pyramidal with the two DPQ nitrogen atoms of the co-ligand positioned respectively at the apex and base of the pyramid. This is confirmed by a shorter Cu1-N1 distance (2.028 Å) and a longer Cu1-N4 distance (2.254 Å) which is attributed to Jahn-Teller distortion.[71]

The X-ray structures of QEFCOV and QEFCUB display the same structural features as KUPDEF, which includes O1, N1 and N2 of the tridentate Schiff base ligand and N3 of the 2,2'-bipyridyl co-ligand all occupying the square base of QEFCOV. O1-N1-N2-N3 are observed to be almost co-planar with a mean deviation from the square pyramidal base plane of 0.0755 Å for QEFCOV and 0.1197 Å for QEFCUB. All Cu-N and Cu-O distances lie within the range of previously reported structures.[70, 71, 73] A deviation from this is noted with the bond length of Cu1-N4 (2.241(2) Å) being longer than the other Cu-N distances. This is due to N4 being the axial nitrogen in the square pyramidal geometry.[71]

The structures most closely related to those of this study are NOYHAM[72], NOYHIU[72], NOYHOA[72] and QEFDAI[73], since all contain the primary ligand (*E*)-2-((quinolin-8-ylimino)methyl)phenol, HL1 of this study, with various substituents on the salicylaldehyde ring. Additionally, the above mentioned complexes all have bidentate co-ligands with nitrogen donor atoms such as 2,2'-bipyridine, 1,10-phenanthroline, pyrazino[2,3-f][1,10]phenanthroline (DPQ) and dipyrido[3,2-a:2',3'-c]phenazine (DPPZ).

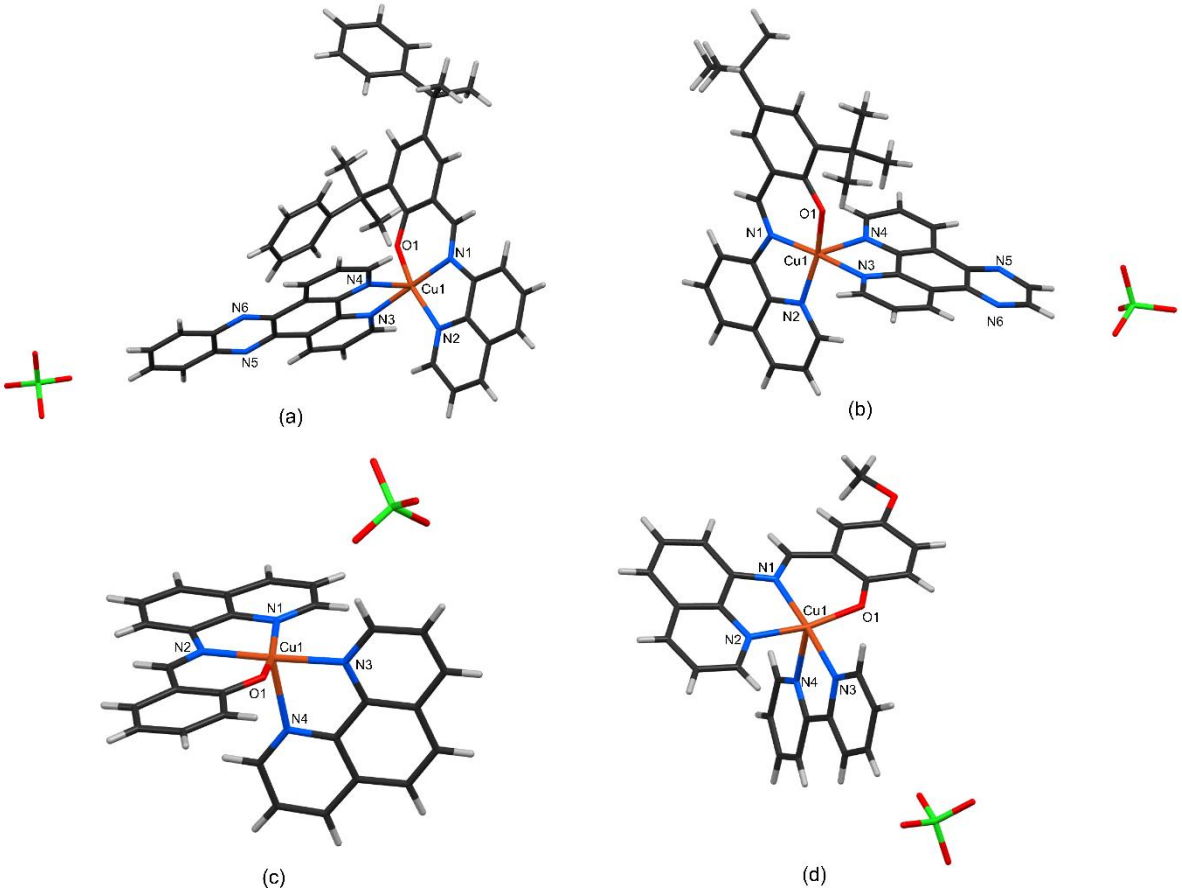

Figure 5.7: X-ray crystal structures of (a) NOYHAM[72], (b) NOYHIU[72], (c) NOYHOA[72] and (d) QEFDAI[73]. The chelates feature derivatives of HL1 as their primary ligands and bidentate *N*-donor co-ligands.

All four X-ray structures illustrated in Figure 5.7 are mononuclear chelates with a penta-coordinated copper(II) centre, each containing one six- and two five-membered chelate rings. The copper(II) centre is penta-coordinated by the *N,N',O* tridentate primary ligand and two nitrogen atoms on the co-ligand. All four chelates also display distorted square pyramidal geometry with the tridentate ligand and a single donor atom of the bidentate ligand forming the basal plane and the second N-atom of the co-ligand in the axial position. The bond parameters describing the coordination sphere of the copper(II) chelates are summarised in Table 5.5 and Table 5.6.

Table 5.5: Average bond lengths (Å) for previously reported copper(II) chelates with square pyramidal coordination geometries.

	NOYHAM[72]	NOYHIU[72]	NOYHOA[72]	QEFDAI[73]
N1 – Cu1	1.951(2)	1.948(2)	1.959(2)	1.949(2)
N2 – Cu1	2.016(2)	2.014(2)	2.010(3)	2.055(2)
N3 – Cu1	2.031(2)	2.033(2)	2.029(2)	2.027(2)
N4 – Cu1	2.245(2)	2.261(2)	2.259(3)	2.246(3)
O1 – Cu1	1.900(2)	1.893(1)	1.913(2)	1.921(2)
C = N_{imine}	1.304(3)	1.312(3)	1.297(4)	1.302(3)

Table 5.6: Average bond angles (°) for previously reported copper(II) chelates with square pyramidal coordination geometries.

	NOYHAM[72]	NOYHIU[72]	NOYHOA[72]	QEFDAI[73]
N1-Cu1-N2	82.0(1)	82.35(7)	82.8(1)	82.0(1)
N1-Cu1-O1	93.0(1)	93.36(7)	93.4(1)	93.0(1)
N3-Cu1-N4	77.1(1)	78.10(7)	78.39(9)	77.1(1)
N2-Cu1-N3	93.3(1)	96.44(7)	93.7(1)	93.3(1)
O1-Cu1-N3	91.5(1)	88.20(7)	92.0(1)	91.5(1)
N1-Cu-N4	103.2(1)	100.66(7)	101.06(9)	103.2(1)
N2-Cu-N4	96.58(7)	98.60(7)	100.98(1)	93.4(1)
O1-Cu-N4	100.93(6)	96.59(7)	91.82(9)	99.45(9)

Table 5.5 and Table 5.6 give the average bond lengths and bond angles for the complexes NOYHAM, NOYHIU, NOYHOA and QEFDAI. All bond lengths compare favourably with each other as expected since all the chelates contain similar *N,N',O* tridentate ligands with similar

nitrogen donors on the co-ligands. The Cu-N bond distances ranged from 1.948 to 2.055 Å, while the Cu-O bond distances range from 1.893 to 1.921 Å. These distances are consistent with comparable bond lengths as previously discussed.[70, 71] The bond angles also show good correlation with each other with slight deviations seen around angles O1-Cu1-N3 and N1-Cu1-N4 which are influenced by the angle at which the co-ligand is positioned relative to the primary tridentate ligand. The most notable deviation lies in the complex NOYHIU; this is attributed to the steric influence of the bulky *t*-butyl substituents on the tridentate ligand.

NOYHIU and QEFDAI are used as representative examples to show the angle subtended by the co-ligand relative to the primary ligand plane. The mean planes were calculated using all non-hydrogen atoms in the co-ligands and the aromatic constituents of the tridentate ligands (i.e. functional groups were omitted). This information could prove to be a useful indicator to determine whether these systems are likely to be effective DNA binding agents. These dihedral angles are summarised in Table 5.7.

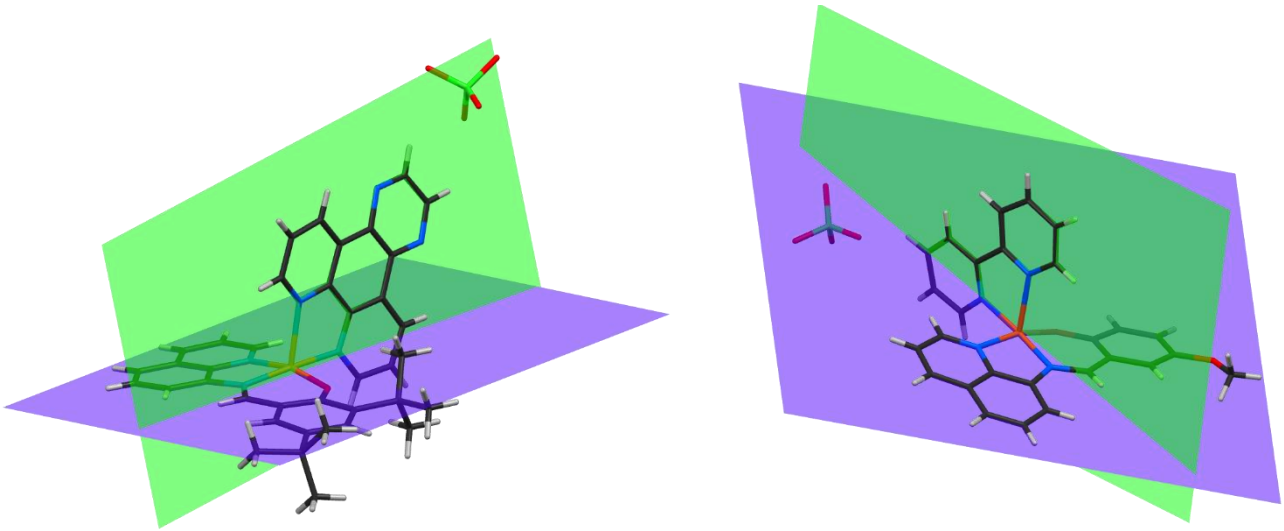

(a) (b)

Figure 5.8: The two planes at which the two ligands are positioned to each other for (a) NOYHIU and (b) QEFDAI. The planes of the co-ligands are shown in green while the primary ligands lie in the purple planes.

Table 5.7: The measured dihedral angle between the mean planes of the primary and co-ligands of the reported copper(II) chelates.

CSD Ref. Code	Dihedral angle between planes (°)
DAYMUN	78.31
DAYNAU	84.90
KUPDEF	86.23
NOYHAM	81.32
NOYHIU	87.00
NOYHOA	85.82
QEFCOV	87.04
QEFCUB	86.19
QEFDAI	88.82

The dihedral angles between the co-ligands and primary ligands for the previously studied chelates range from 78.31° – 88.82°. These data show that the two ligands are nominally perpendicular. The main factor influencing this parameter is likely to be steric hindrance from any bulky substituents on the primary ligands. The chelates will then adopt an orientation which will minimise any non-bonded repulsion between these bulky groups and the co-ligands. In DNA binding, the angle at which the two planes are positioned is crucial in heteroleptic complexes since only one of the two ligands interact directly with the DNA double helix. The closer the angle is to 90° the better the intercalation properties.[75]

5.1.4 Objectives

The main objective of the crystallographic studies is to investigate the solid state structures of the copper(II) chelates and contribute to the existing body of knowledge relating to heteroleptic copper(II) complexes. This study will also provide insight into the nature of the solid state interactions that these systems exhibit, providing valuable information as to whether these chelates are likely to be effective DNA binding agents.

5.2 Experimental

The X-ray data were recorded on a Bruker Apex Duo diffractometer equipped with an Oxford Instruments Cryojet operating at 100(2) K and an Incoatec microsource operating at 30 W power. For all structures the data were collected with M_o *K*α (λ = 0.71073 Å) radiation at a crystal-to-detector distance of 50 mm. The data collections were performed using omega and phi scans with exposures taken at 30 W X-ray power and 0.50° frame widths using APEX2.[76]

The data were reduced with the program SAINT using outlier rejection, scan speed scaling, as well as standard Lorentz and polarisation correction factors.[76] A SADABS semi-empirical multi-scan absorption correction was applied to the data.[76] Direct methods, SHELXS and WINGX were used to solve all structures.[77, 78] All non-hydrogen atoms were located in the difference density map and refined anisotropically with SHELXLS.[77] The hydrogen atoms of all NH and OH groups were located in the difference density map and allowed to refine isotropically. All diagrams were rendered using Mercury 3.3.

The molecular structures were validated using an IUCR checkCIF[79] and the reports are available in Appendix C.

Table 5.8 and Table 5.9 provides a summary of the crystallographic data for the single-ligand and heteroleptic copper(II) chelates synthesised in this work.

Table 5.8: Summary of the X-ray data for the single-ligand copper(II) chelates.

Crystal Data	**[Cu(L1)(Cl)]**	**[Cu(L2)(Cl)$_2$]**	**[Cu(L2)(Cl)$_2$]·MeOH**
Chemical formula	$C_{16}H_{11}ClCuN_2O{\cdot}CH_3OH$	$C_{15}H_{11}Cl_2CuN_3$	$C_{16}H_{15}Cl_2CuN_3O$
***M*$_r$**	378.30	367.71	399.75
Crystal system	Triclinic	Triclinic	Monoclinic
Space group	*P*-1	*P*-1	$P2_1/c$
Temperature / K		100	
***a* / Å**	7.9838(4)	6.9474(5)	9.5526(9)
***b* / Å**	8.8753(5)	8.3637(6)	8.7837(9)
***c* / Å**	11.7868(6)	12.4235(8)	18.959(2)
α / °	71.550(2)	98.995(3)	90.00
β / °	71.550(2)	100.072(3)	95.786(5)
γ / °	67.783(2)	92.536(3)	90.00
Z	2	2	4
Radiation type		M_o K_α	
***V* (Å^3)**	730.28(7)	700.11(8)	1582.7
F(000)	386	370	812
μ (mm^{-1})	1.69	1.94	1.72
Crystal size (mm)	0.18 x 0.12 x 0.07	0.26 × 0.09 × 0.05	0.55 × 0.21 × 0.16
Diffractometer		Bruker *APEX*-II CCD	
Absorption correction		Multi-scan *SADABS*, Bruker 2012	
No. of measured, independent and observed [*I* > 2σ(*I*)] reflections	20960, 3285, 3018	11495, 2691, 2553	11341, 3093, 2890
R$_{int}$	0.024	0.016	0.023
Refinement			
R*[*F*^{2} > 2σ(*F*^{2})], *wR*(*F*^{2}), *S	0.041, 0.119, 1.13	0.021, 0.055, 1.11	0.025, 0.061, 1.03
No. of reflections	3285	2691	3093
No. of parameters	210	190	212
No. of restraints	0	0	0
Δρ$_{max}$, Δρ$_{min}$ (e Å^{-3})	0.75, −1.59	0.47, −0.23	0.36, −0.35

Table 5.9: Summary of the X-ray data for the heteroleptic copper(II) chelates.

Crystal Data	[Cu(L1)(Bpy)](Cl)	[Cu(L1)(Phen)](Cl)	[Cu(L1)(Phen-NH_2)](Cl)
Chemical formula	$C_{26}H_{19}Cl_1Cu_1N_4O_1$	$C_{28}H_{19}ClCuN_4O_2 \cdot 5H_2O$	$C_{28}H_{20}ClCuN_5O$
M_r	502.44	535.47	541.48
Crystal system	Monoclinic	Triclinic	Triclinic
Space group	$P2_1/n$	P-1	P-1
Temperature / K		100	
***a* / Å**	12.4998(12)	14.0251(11)	10.7071(4)
***b* / Å**	22.288(2)	14.3232(12)	11.3941(4)
***c* / Å**	19.0810(16)	14.7635(11)	12.4902(5)
α / °	90.00	94.455(4)	106.702(2)
β / °	103.856(3)	105.789(4)	109.913(2)
γ / °	90.00	114.679(4)	103.598(2)
Z	8	4	2
Radiation type		M_o K_α	
***V* (Å^3)**	5161.1(8)	2530.4(3)	1274.97(9)
F(000)	2056	1096	554
μ (mm^{-1})	0.97	1.00	0.99
Crystal size (mm)	0.26 x 0.18 x 0.12	0.31 × 0.13 × 0.08	0.05 × 0.03 × 0.02
Diffractometer		Bruker *APEX*-II CCD	
Absorption correction		Multi-scan *SADABS*, Bruker 2012	
No. of measured, independent and observed [$I > 2\sigma(I)$] reflections	36463, 10106, 8704	40319, 11571, 8396	24236, 6605, 5615
R_{int}	0.054	0.064	0.023
Refinement			
R*[$F^2 > 2\sigma(F^2)$], *wR*(F^2), *S	0.072, 0.212, 1.11	0.055, 0.163, 1.01	0.033, 0.085, 1.06
No. of reflections	10106	11571	6605
No. of parameters	595	648	333
No. of restraints	0	1	0
$\Delta\rho_{max}$, $\Delta\rho_{min}$ (e Å^{-3})	2.22, −1.75	0.75, −1.16	0.52, −0.28

5.3 Results and Discussion

5.3.1 X-ray crystallography of single-ligand copper(II) complexes

a) X-ray structure analysis of [Cu(L1)(Cl)]

The copper(II) complex of HL1 crystallised in the triclinic space group *P*-1, with a single molecule in the asymmetric unit (*Z* = 2). The structure of [Cu(L1)(Cl)] consists of dimeric units linked by Cu-Cl-Cu bridges. The asymmetric unit comprises a single square planar copper(II) chelate with the tridentate ligand and a chloro ligand occupying the four coordination sites. The molecule is an inversion dimer bridged by two chloride ions. The molecule crystallised as the methanol monosolvate i.e. one methanol molecule per asymmetric unit. The crystal structure for [Cu(L1)(Cl)] has been previously crystalised by Liu *et al*. in the monoclinic space group *P*2(1)/*n* and also displayed the same polymeric units linked by single Cu-Cl-Cu bridges.[80] The structure reported herein is therefore a polymorph of that previously reported. The contents of the asymmetric unit and the structure of the inversion dimer are shown in Figure 5.9.

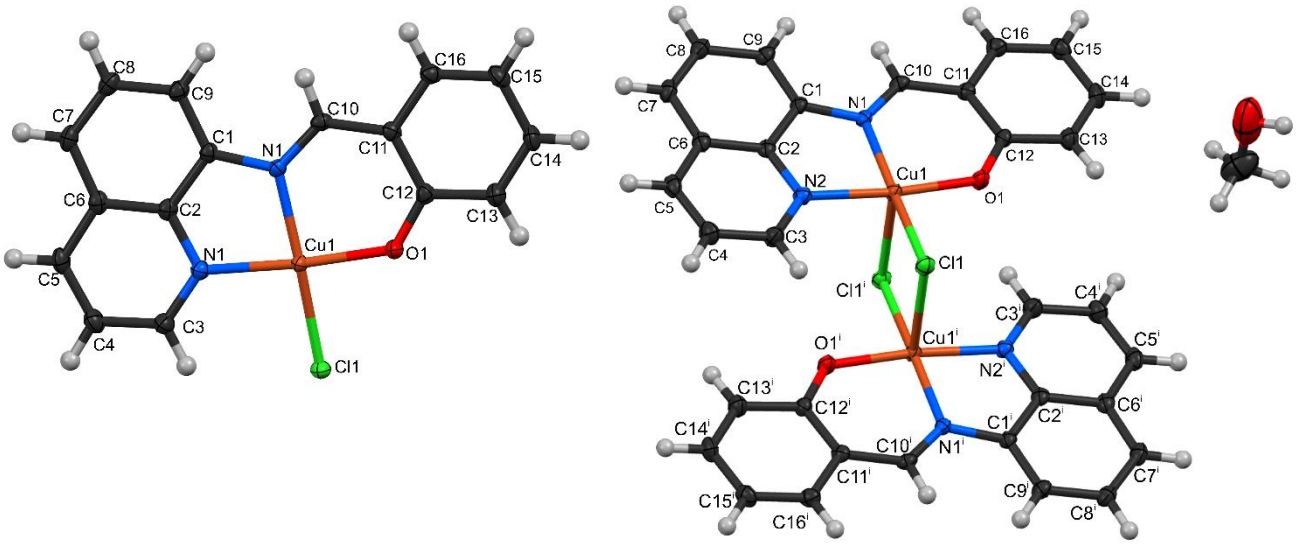

Figure 5.9: (a) The asymmetric unit of [Cu(L1)(Cl)] and (b) the inversion dimer of [Cu(L1)(Cl)], with thermal ellipsoids drawn at the 50% probability level. Hydrogen atoms have been rendered as spheres of arbitrary radius. Symmetry code: -x, -y, -z.

The dimeric μ-chloro structure of [Cu(L1)(Cl)] exhibits the expected square pyramidal geometry as noted with previous heteroleptic complexes of this class.[70, 73] Selected bond lengths and angles for [Cu(L1)(Cl)] are summarised in Table 5.10 The C=N_{imine} bond length

measures 1.305(5) Å and lies within the range of 1.274(5) - 1.366(3) Å for previously reported structures. Bond lengths, Cu1-N1, Cu1-N2 and Cu1-O1 measure 1.973(3), 2.002(3) and 1.908(3) Å, respectively. Again, comparing favourably to similar previously reported complexes.[80]

The square pyramidal geometry of the metal centre has a basal plane which consists one oxygen atom and two nitrogen atoms from the Schiff base ligand and one chloro ligand. The base forms a near ideal least squares plane (N1-N2-Cu1-O1-Cl1) with the largest deviation from the mean plane occurring at N1 with a deviation of 0.064 Å. The copper(II) ion is displaced by 0.132 Å from the same mean plane towards the apical chloride. The apical Cu-Cl bond is significantly longer (2.8151(8) Å) than the Cu-Cl bond of the basal chloride ion (2.2924(9) Å).

The bond angles, N1-Cu1-N2 and N1-Cu1-O1, measuring 82.3(1)° and 93.7(1)°, respectively are comparable to related structures.[68] The large difference between the two angles is attributed to the differing bite of the ligand chelating atoms; the five-membered ring (C1-C2-N2-Cu1-N1) having a smaller angle than the larger six-membered (C10-N1-Cu1-O1-C12-C11). The bond angles describing the coordination sphere of [Cu(L1)Cl] are summarised in Table 5.10.

Table 5.10: Selected bond lengths (Å) and bond angles (°) for [Cu(L1)(Cl)].

Bond lengths (Å)	
Cu1-N1	1.973(3)
Cu1-N2	2.002(3)
Cu1-O1	1.908(3)
Cu1-Cl1	2.2924(9)
Cu1-Cl1*	2.8151(8)
C10-N1	1.305(5)
Bond angles (°)	
N1-Cu1-N2	82.3(1)
N1-Cu1-O1	93.7(1)
N2-Cu1-Cl1*	95.21
O1-Cu1-Cl1	89.09

* denotes an inversion symmetry related chloro ligand which occupies the fifth coordination site.

The chelate [Cu(L1)Cl] crystallises as the methanol monosolvate. The methanol OH group is involved in a bifurcated hydrogen bond (i.e. a single H-bond donor and two H-bond acceptors). The methanolic OH is hydrogen-bonded to the chloro ligand and the phenolic oxygen atom. This hydrogen bonding motif leads to a four-membered hydrogen-bonded ring. The hydrogen bonding is depicted in Figure 5.10 below. The hydrogen bond parameters are summarised in Table 5.11.

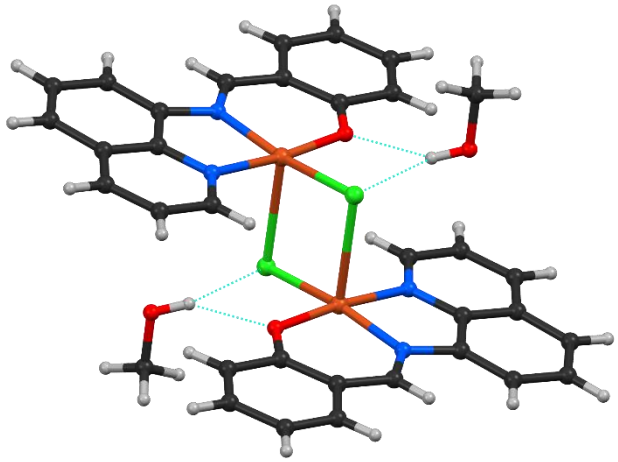

Figure 5.10: Hydrogen bonding motif of [Cu(L1)Cl] showing the bifurcated nature of the intermolecular interaction. Hydrogen bonds are shown as dashed blue lines.

Table 5.11: Hydrogen bond parameters (Å, °) of [Cu(L1)Cl].

Hydrogen Bond	D–H	H···A	D···A	D–H···A
O–H···O	0.84(2)	2.032(2)	2.788(6)	128(1)
O–H···Cl	0.84(2)	2.813(2)	3.391(7)	149(1)

The data in Table 5.11 show that the hydrogen bond lengths are significantly shorter than the sum of the van der Waals radius of the interacting atoms by 0.137 and 0.688 Å, for the O–H···O and O–H···Cl interactions, respectively. Although bond length does not necessarily correlate linearly with bond strength due to packing constraints in the lattice, these bond lengths are significantly shorter than the sum of the van der Waals radii and are therefore likely to be moderate to strong interactions.

b) X-ray structures of $[Cu(L2)(Cl)_2]$ and $[Cu(L2)(Cl)_2]\cdot MeOH$

The copper(II) complex $[Cu(L2)(Cl)_2]$ crystallised as pseudopolymorphs. After crystallisation by slow liquid diffusion of a methanol solution of the chelate into diethyl ether, inspection of the crystals revealed two crystals of different shades of green. Crystallographic studies showed that one molecule crystallised as the methanol monosolvate ($[Cu(L2)(Cl)_2]\cdot MeOH$) and the other was solvent free. $[Cu(L2)(Cl)_2]$ crystalised in the triclinic space group *P*-1 with $Z = 2$; a single molecule in the asymmetric unit. $[Cu(L2)(Cl)_2]\cdot MeOH$ crystalised in the triclinic space group $P2_1/c$ with $Z = 4$ and one chelate and methanol solvate molecule in the asymmetric unit. The asymmetric unit of each polymorph is shown in Figure 5.11.

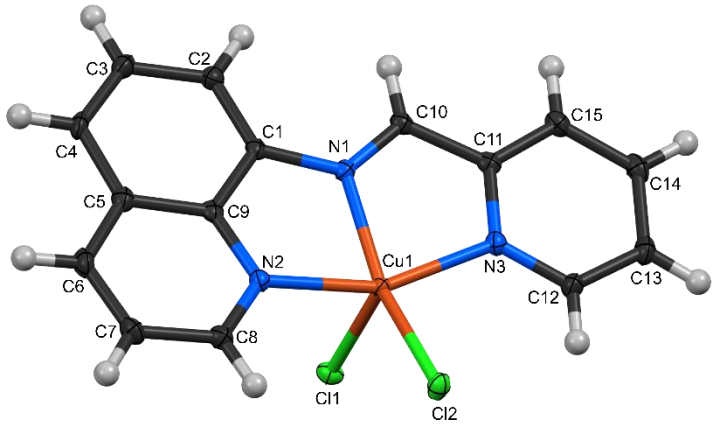

(a)

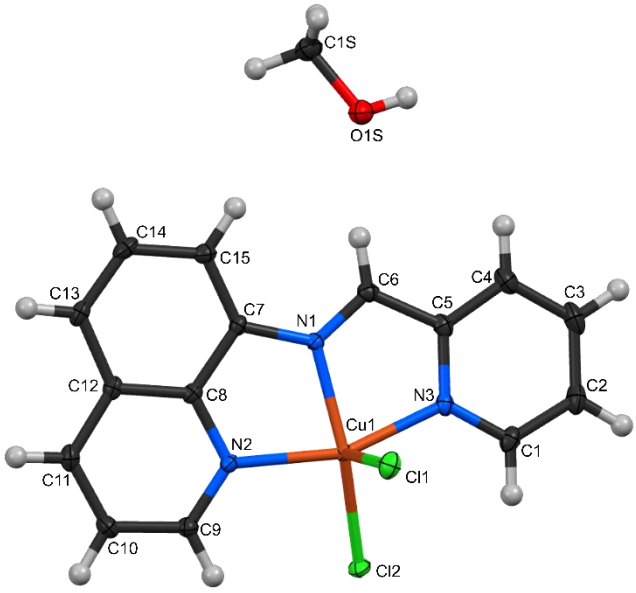

(b)

Figure 5.11: Labelled solid state structures of (a) [Cu(L2)(Cl)2] and (b) [Cu(L2)(Cl)2]·MeOH with thermal ellipsoids drawn at the 50% probability level. Hydrogen atoms have been rendered as spheres of arbitrary radius.

Both $[Cu(L2)(Cl)_2]$ and $[Cu(L2)(Cl)_2]\cdot MeOH$ display the typical distorted square pyramidal geometry around the copper(II) centre. The two pseudopolymorphs are structurally identical but slight variations in bond lengths and bond angles around the metal centre were noted. N3-Cu1 and N2-Cu2 have similar bond lengths and are considerably longer when compared to N1-Cu1. The bond length N3-Cu1 in $[Cu(L2)(Cl)_2]$ is 2.046(2) Å, while the equivalent bond in $[Cu(L2)(Cl)_2]\cdot MeOH$ measures 2.027(2) Å. The $C=N_{imine}$ bond length in both structures are comparable measuring 1.282(2) and 1.289(2) Å. The Cu-Cl bond lengths are the longest due to the chloride ligands having a large van der Waals radius thus extending the bond lengths.

The N1-Cu1-N2 bond angles in both structures measure 80.62(6)° while N1-Cu1-N3 measures 79.27(6)° for $[Cu(L2)(Cl)_2]$ and 79.62(6)° for $[Cu(L2)(Cl)_2]\cdot MeOH$. The Cl1-Cu1-Cl2 bond angle is the most obtuse in both structures and is caused by steric repulsion between the chloro ligands. The most notable difference between the structures $[Cu(L2)(Cl)_2]$ and $[Cu(L2)(Cl)_2]\cdot MeOH$ is the Cl1-Cu-Cl2 bond angle. This difference is attributed to the latter structure being involved in hydrogen bonding. The larger bond angle seemingly allows for more efficient hydrogen bonding. The bond lengths and bond angles describing the coordination sphere of $[Cu(L2)(Cl)_2]$ and $[Cu(L2)(Cl)_2]\cdot MeOH$ are summarised in Table 5.12.

Table 5.12: Selected bond lengths and bond angles of [Cu(L2)(Cl)2] and [Cu(L2)(Cl)2]·MeOH

Bond lengths (Å)		
	$[Cu(L2)(Cl)_2]$	$[Cu(L2)(Cl)_2]\cdot MeOH$
N1-Cu1	1.985(1)	1.989(2)
N3-Cu1	2.046(2)	2.034(2)
N2-Cu1	2.042(1)	2.027(2)
Cl1-Cu1	2.4616(5)	2.2461(5)
Cl2-Cu1	2.2567(6)	2.5208(6)
$C=N_{imine}$	1.282(2)	1.289(2)
Bond angles (°)		
	$[Cu(L2)(Cl)_2]$	$[Cu(L2)(Cl)_2]\cdot MeOH$
N1-Cu1-N2	80.62(6)	80.62(6)
N1-Cu1-N3	79.27(6)	79.62(6)
N1-Cu1-Cl1	97.42(5)	96.76(5)
Cl1-Cu1-Cl2	105.26(2)	108.45(2)

Along with the variations in the bond lengths and angles between the two pseudopolymorphs, the structures also have different space groups with a different number of molecules in each unit cell. $[Cu(L2)(Cl)_2]$ has two molecules in the unit cell shown in Figure 5.12.

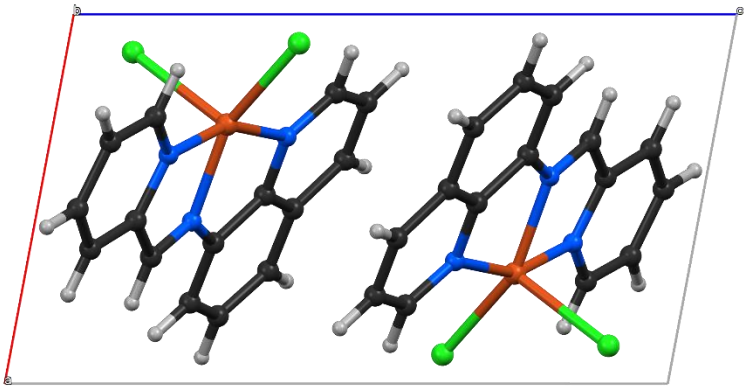

Figure 5.12: Packing diagram of $[Cu(L2)(Cl)_2]$ viewed down the *b*-axis.

The packing diagram of $[Cu(L2)(Cl)_2]$·MeOH shows four complex molecules and four methanol molecules in the unit cell. Figure 5.13 shows the packing of $[Cu(L2)(Cl)_2]$·MeOH with noticeable differences to the packing diagram of $[Cu(L2)(Cl)_2]$.

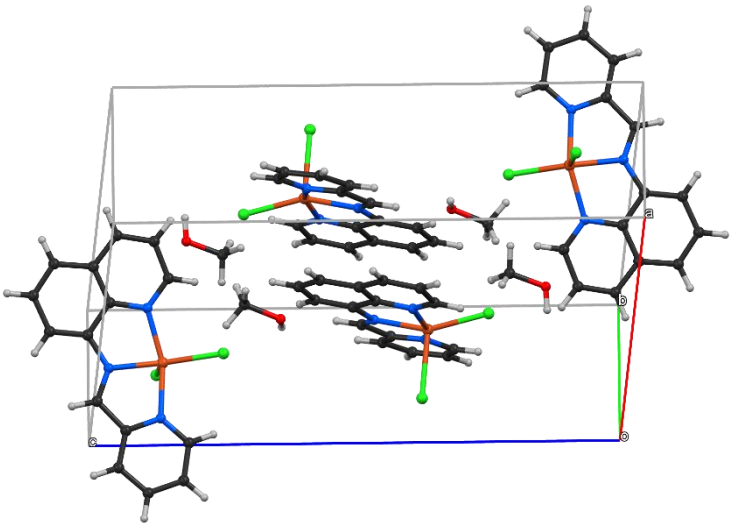

Figure 5.13: Packing diagram of $[Cu(L2)(Cl)_2]$·MeOH.

The methanol OH group of $[Cu(L2)(Cl)_2]$·MeOH is involved in hydrogen bonding. The methanolic OH is hydrogen-bonded to a single chloro ligand. The hydrogen bonding is depicted in Figure 5.14. The hydrogen bond parameters are summarised in Table 5.13.

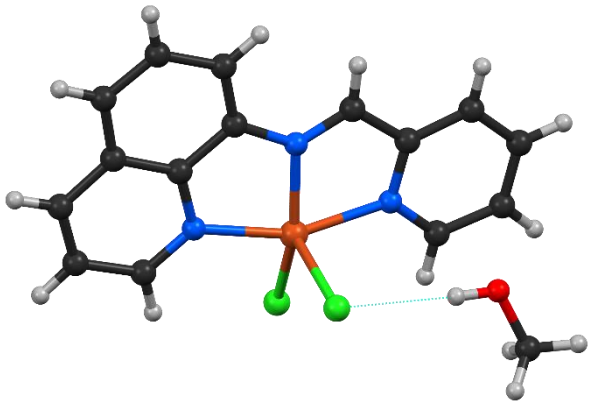

Figure 5.14: Hydrogen bonding of $[Cu(L2)(Cl)_2]\cdot MeOH$ showing the nature of the intermolecular interaction. The hydrogen bond is shown as a dashed blue line.

Table 5.13: Hydrogen bond parameters (Å, °) of $[Cu(L2)(Cl)_2]\cdot MeOH$

Hydrogen Bond	D–H	H···A	D···A	D–H···A
O–H···Cl	0.835(3)	2.349(3)	3.183(2)	176(2)

The data in Table 5.13 show that it is a very short interaction distance. This coupled with the fact that the bond angle is approaching ideality (180°) suggests that this is a strong hydrogen bond.

5.3.2 X-ray crystallography of heteroleptic copper(II) complexes

a) X-ray structure analysis of [Cu(L1)(Bpy)](Cl)

The complex [Cu(L1)(Bpy)](Cl) crystallised in the monoclinic space group $P2_1/n$, with two molecules in the asymmetric unit and $Z = 4$. A search of the CSD showed that the solid state structure of [Cu(L1)(Bpy)](Cl) was not previously elucidated.

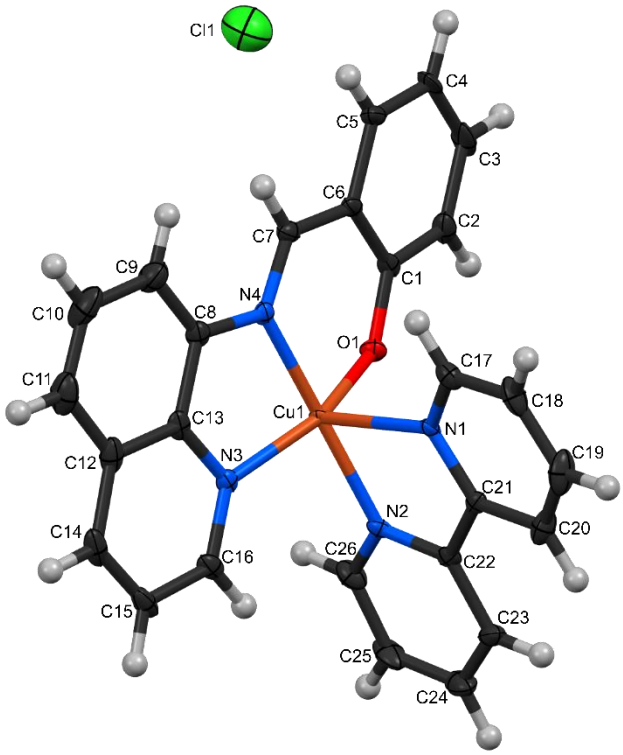

Figure 5.15: X-ray crystal structure of [Cu(L1)(Bpy)](Cl) showing a single molecule of the asymmetric unit, and atom numbering scheme with thermal ellipsoids drawn at the 50% probability level. Hydrogen atoms are rendered as spheres of arbitrary radius.

The two molecules within the asymmetric unit are very similar as illustrated by a least-squares fit which gives a root mean square deviation (RMSD) of 1.1484 Å. The two molecules will therefore be discussed collectively. [Cu(L1)(Bpy)](Cl) exhibits a distorted square pyramidal geometry around the copper(II) centre. The basal plane is made up of two nitrogen atoms and one oxygen atom from the Schiff base ligand and one nitrogen atom (N2) from the co-ligand, Bpy. The apical coordination site is occupied by a nitrogen atom (N1) from the Bpy co-ligand. The base does not form an ideal least squares plane since ring bending is observed between

the 8-aminoquinoline moiety and the salicylic ring. The largest deviations from the mean plane (all non-H atoms of the Schiff base ligand) are 0.083 and 0.156 Å for C4 and C5, respectively. The copper(II) ion is displaced by 0.110 Å from the basal plane towards the apical nitrogen atom.

The solid state structure for [Cu(L1)(Bpy)](Cl) illustrates a mononuclear species with a penta-coordinated copper(II) centre. Three chelating rings are observed around the metal centre with one six- and two five-membered rings. The distances between the Cu1 atom and the donor atoms are summarised in Table 5.14. All bond lengths lie within the reported range for Cu-O and Cu-N bonds. It is also noted that the apical nitrogen N1 has a longer bond length measuring 2.214(4) Å, compared to the three Cu-N bond distances for the atoms in the basal plane.

The key bond angles lie within the chelating rings around the metal centre. Angle N4-Cu1-O1 measures 93.3(1)° while N3-Cu1-N4 has an acute angle of 82.6(1)°. The large difference is attributed to the ring sizes, with the six-membered ring C1-O1-Cu1-N4-C7 possessing the larger bond angle as compared to the smaller five-membered ring. The chelating ring of the co-ligand has the smallest bond angle of 78.1(1)°; a consequence of the small bite angle. The bulk of the bond parameters are summarised in Table 5.14.

Table 5.14: Selected average bond lengths and angles for [Cu(L1)(Bpy)](Cl).

Bond lengths (Å)	
Cu1-N1	2.214(4)
Cu1-N2	2.017(3)
Cu1-N3	2.022(3)
Cu1-N4	1.954(3)
Cu1-O1	1.931(2)
C=N_{imine}	1.311(5)
Bond angles (°)	
N1-Cu1-N2	78.1(1)
N4-Cu1-O1	93.3(1)
N3-Cu1-N4	82.6(1)
N2-Cu1-N4	174.4(1)

An interesting aspect of heteroleptic complexes is the angle subtended by the two ligands. As previously mentioned, this information will aid in the understanding of whether the complex will be a good DNA intercalator or groove binder.

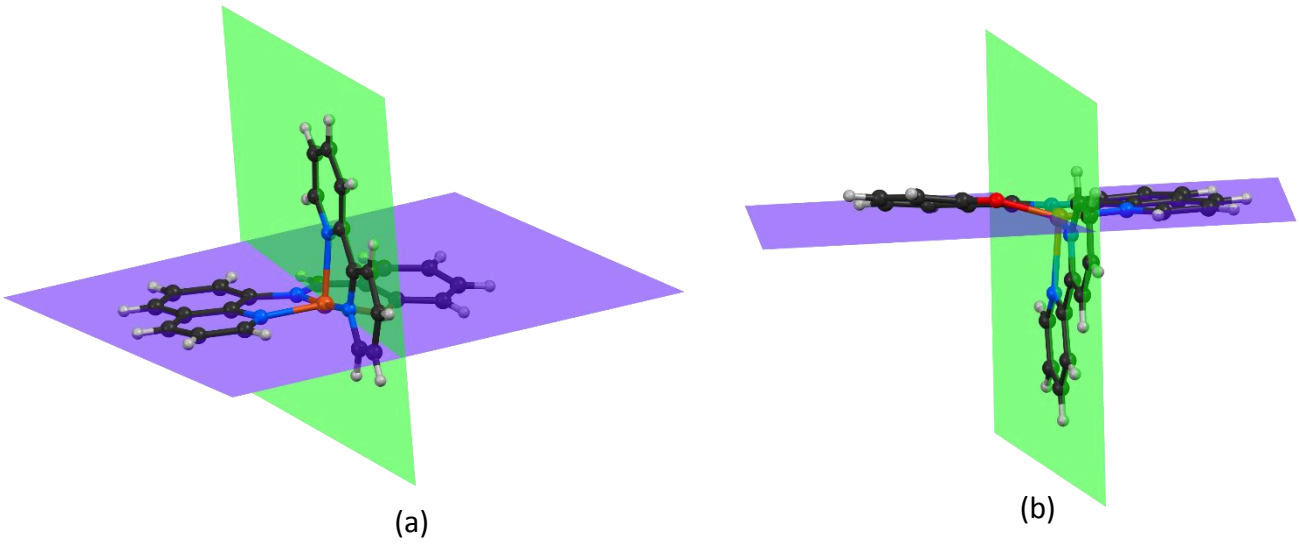

Figure 5.16: Perspective views of the mean planes (all non-H atoms) generated by the two ligands. The tridentate ligand lies in the purple plane and the Bpy co-ligand in the green plane.

Figure 5.16 highlights the near perpendicular position of the Bpy ligand relative to the Schiff base ligand, subtending an angle of 89.17°. The two planes lie almost perpendicular to each other; this orientation should lead to minimal steric strain. When reviewing previous heteroleptic complexes of this class it was observed that by adding bulky substituents onto the tridentate ligand, it had a noticeable influence of the angle between the planes.[70, 71, 73] Figure 5.16 (b) also highlights the ring bending of the *N,N',O* ligand after it is coordinated to the copper(II) centre. Section 5.1.2 reported the free *N,N',O* ligand (NEZQAL) which had a slight deviation of 3.81° between the quinoline heterocyclic ring system and the salicylideneimine moiety. Once coordinated to the copper(II) centre in [Cu(L1)(Bpy)](Cl), the same angle increases to 10.85°. This is illustrated in Figure 5.16 (b) where the salicylic ring system lies significantly above the plane.

[Cu(L1)(Bpy)](Cl) does not display any classical hydrogen bonding, however, the structure does exhibit intermolecular C-H···O interactions between the phenolic oxygen (O2) of the *N,N',O* ligand and the bipyridyl C26-H26 group of an adjacent molecule. This leads to the formation of a dimeric supramolecular structure with crystallographically imposed inversion symmetry (Figure 5.17). Although C-H···O interactions are generally considered weak intermolecular

interactions. In this case the D···A distance is 0.260 Å shorter than the sum of the van der Waals radii suggesting a stronger interaction. In addition to these interactions, the dimer is further stabilised by π···π interactions between the Bpy and Schiff base ligands. The interplanar spacing measures 3.28 Å, which is shorter than the interplanar spacing in graphite (3.35 Å) suggesting it would have a significant stabilising force.

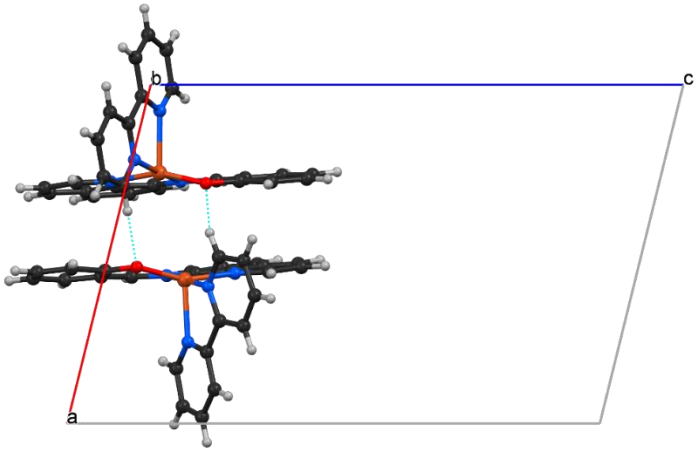

Figure 5.17: The dimeric supramolecular structure of [Cu(L1)(Bpy)](Cl) supported by C-H···O. Viewed down the *b*-axis.

b) X-ray structure analysis of [Cu(L1)(Phen)](Cl)

[Cu(L1)(Phen)](Cl) crystallised in the triclinic space group *P*-1 with two molecules in the asymmetric unit (*Z* = 2). The crystal structure for [Cu(L1)(Phen)](Cl) has been previously elucidated by Lin *et al.* in the monoclinic space group P2(1)/c with *Z* = 4.[72] The structure reported herein is therefore a polymorph of that previously reported.

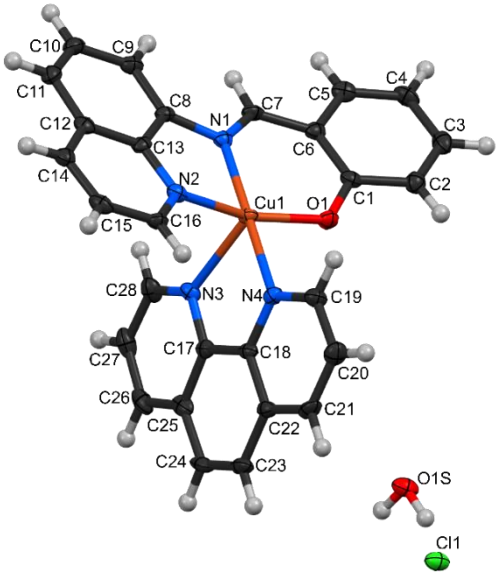

Figure 5.18: X-ray crystal structure of [Cu(L1)(Phen)](Cl) showing a single molecule of the asymmetric unit and associated water molecule and chloride counter ion showing the atom numbering scheme. Thermal ellipsoids drawn at the 50% probability level.

The solid state structure of [Cu(L1)(Phen)](Cl) displays a mononuclear species with a penta-coordinated copper(II) centre resulting in three chelating rings, i.e. one six- and two five-membered chelating rings. The copper(II) centre is penta-coordinated by two nitrogen atoms and one oxygen atom from the *N,N',O* tridentate Schiff base ligand and by two nitrogen atoms from 1,10-phenanthroline. This yields a distorted square pyramidal coordination geometry around the copper(II) centre.

Atoms N1, N2, N4 and O1 form the base which is a near ideal least squares plane with N3 being the apical atom. The largest deviation from the mean basal plane occurs at C16 with a deviation of 0.314 Å. The copper(II) centre also shows a displacement of 0.138 Å from the four coordinating atoms of the basal plane towards the apical nitrogen.

[Cu(L1)(Bpy)](Cl) and [Cu(L1)(Phen)](Cl) show similar trends in Cu-N and Cu-O bond lengths. N3, the apical atom, has an elongated bond length of 2.242(3) Å when compared the other Cu-N bond lengths which range from 1.950(3) - 2.020(3) Å. All bond lengths compare favourably with those previously reported for similar heteroleptic complexes of this class.[72]

The six-membered chelate ring and associated bond angle N1-Cu1-O1 (93.42(1)°) is again more obtuse than those of the five-membered chelate rings, N1-Cu1-N2 and N3-Cu1-N4 with bond angles measuring 83.05(1)° and 77.52(1)°, respectively. Table 5.15 summarises selected bond lengths and bond angles for [Cu(L1)(Phen)](Cl).

Table 5.15: Selected average bond lengths and bond angles for [Cu(L1)(Phen)](Cl).

Bond lengths (Å)	
Cu1-N1	1.962(3)
Cu1-N2	2.014(3)
Cu1-N3	2.293(3)
Cu1-N4	2.034(3)
Cu1-O1	1.911(3)
C=N_{imine}	1.287(4)
Bond angles (°)	
N1-Cu1-N2	83.05(1)
N1-Cu1-O1	93.42(1)
N3-Cu1-N4	77.52(1)
N1-Cu1-N4	178.99(1)

The chelate [Cu(L1)(Phen)](Cl) crystallises as the hemihydrate i.e. a single water molecule associated with the two metal chelates in the asymmetric unit. The water molecule bridges a single chelate and chloride counter ion to form a hydrogen-bonded trimeric structure. The hydrogen bonding motif is depicted in Figure 5.19. The hydrogen bond parameters are summarised in Table 5.16.

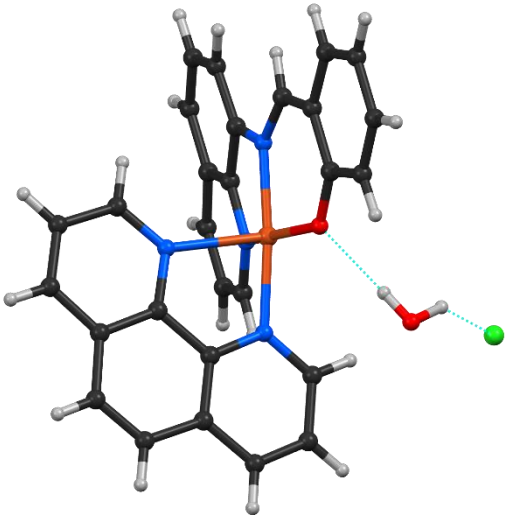

Figure 5.19: Hydrogen bonding of [Cu(L1)(Phen)](Cl) showing the bridging water molecule and resulting heterotrimeric structure.. Hydrogen bonds are shown as dashed blue lines.

Table 5.16: Hydrogen bond parameters (Å, °) of [Cu(L1)(Phen)](Cl).

Hydrogen Bond	D–H	H···A	D···A	D–H···A
O–H···O	0.83(3)	1.958(3)	2.785(3)	177(4)
O–H···Cl	0.89(6)	2.396(5)	3.137(2)	140(5)

The steric bulk of the water molecules along with the steric bulk of the four chloride ions in the unit cell could aid crystallisation by reducing the size of the intermolecular cavities. The angle at which the two ligand planes are positioned relative to each other measures 89.75°. Figure 5.20 highlights the near perpendicular orientation between the tridentate ligand and the Phen co-ligand.

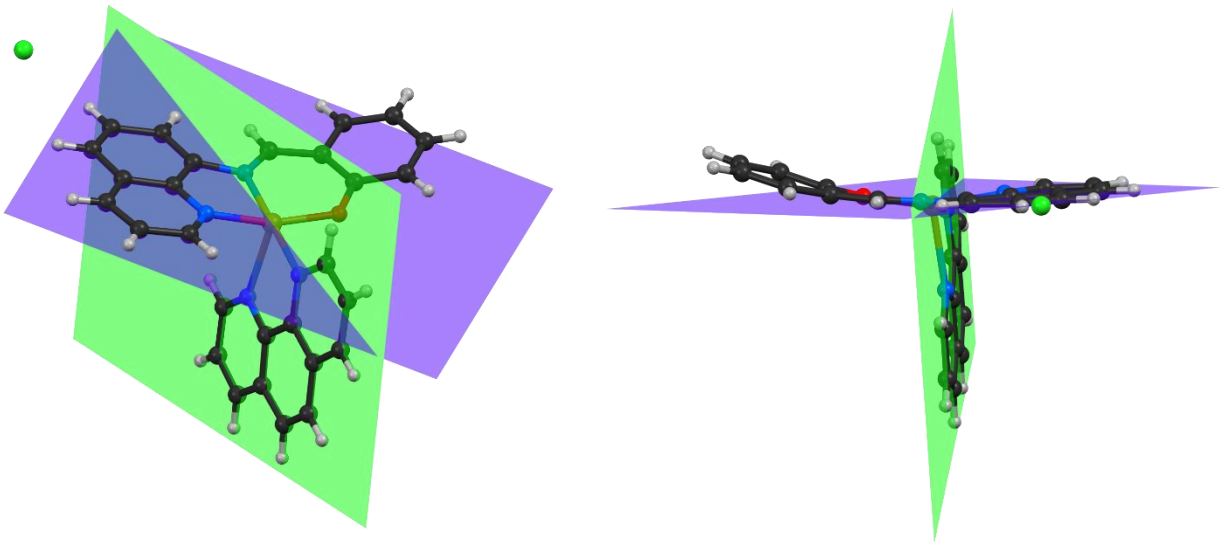

(a) (b)

Figure 5.20: Two views of the planes generated by the two ligands of [Cu(L1)(Phen)](Cl). The tridentate ligand plane is shown in purple and the Phen co-ligand plane is shown in green.

As seen with [Cu(L1)(Bpy)](Cl), the two ligand planes of [Cu(L1)(Phen)](Cl) lie almost perpendicular to each other again leading to minimal steric strain. Figure 5.20 (b) also highlights the ring bending noted for the *N,N',O* ligand after it is coordinated to the copper(II) centre. The angle deviation between the planes of the quinoline heterocyclic ring system and the salicylideneimine moiety are much larger for [Cu(L1)(Phen)](Cl) measuring 18.51°. A greater angle than that reported for the free ligand NEZQAL which is 3.81°.

b) X-ray structure analysis of [Cu(L1)(Phen-NH_2)](Cl)

[Cu(L1)(Phen-NH_2)](Cl) crystallised in the triclinic space group *P*-1 with a single molecule in the asymmetric unit and *Z* = 2. A search of the CSD showed that the solid state structure of [Cu(L1)(Phen-NH_2)](Cl) was not previously elucidated.

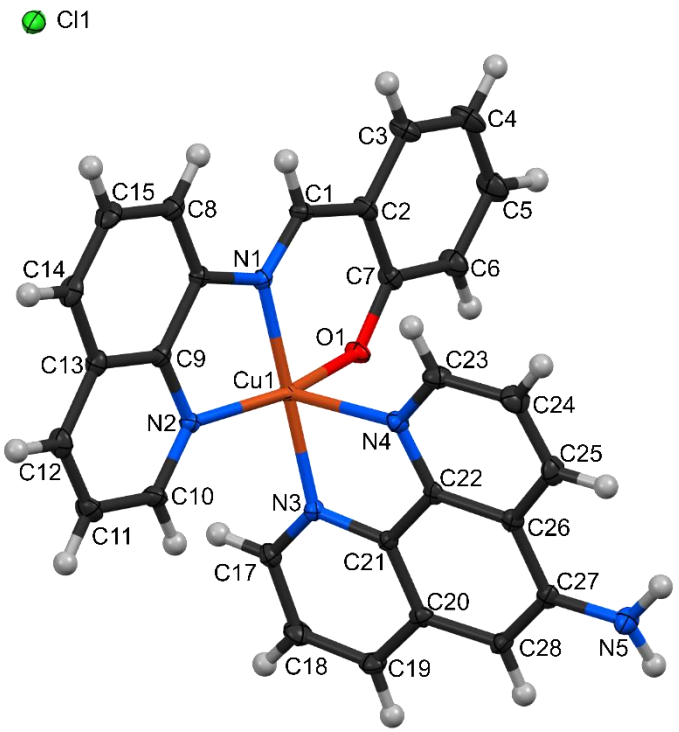

Figure 5.21: Labelled solid state structure of [Cu(L1)(Phen-NH_2)](Cl) showing the atom numbering scheme with thermal ellipsoids drawn at the 50% probability level. Hydrogen atoms are rendered as spheres of arbitrary radius.

[Cu(L1)(Phen-NH_2)](Cl) exhibits the typical distorted square pyramidal geometry around the copper(II) centre with one six- and two five-membered chelating rings. The basal plane comprises two nitrogen atoms and one oxygen atom from the Schiff base ligand and one nitrogen atom (N3) from the co-ligand, Phen-NH_2. The apical coordination site is occupied by the second nitrogen atom (N4) of the Phen-NH_2 co-ligand. The basal plane shows similar characteristics to those previously discussed. In this chelate structure, the largest deviation from the basal plane occurs at C4 with a deviation of 0.610 Å. The copper(II) ion is displaced from the basal plane towards the apical nitrogen with a deviation of 0.124 Å.

The solid state structure of [Cu(L1)(Phen-NH_2)](Cl) shows a mononuclear species with a penta-coordinated copper(II) centre. Cu-N and Cu-O bond lengths are consistent with those of this study as well as those in literature.[71, 73] The distances between the Cu1 ion and the donor

atoms are summarised in Table 5.17. It is again noted that the apical nitrogen N4 has a longer bond length of 2.241(2) Å, when compared to the other Cu-N bond distances.

Similar trends to those previously discussed with respect to the bond angles of the coordination sphere are again noted. N1-Cu1-O1 bond angle measures 92.89(6)° while N1-Cu1-N2 measures 82.95(6)°. The large difference is again attributed to the ring and associated bite of the ligands. The chelate ring of the co-ligand has the smallest bond angle of all three chelates reported herein, measuring 78.78(6)°.

Table 5.17: Selected bond lengths and bond angles for [Cu(L1)(Phen-NH_2)](Cl).

Bond lengths (Å)	
Cu1-N1	1.957(2)
Cu1-N2	2.010(1)
Cu1-N3	2.013(2)
Cu1-N4	2.241(2)
Cu1-O1	1.940 (9)
C=N_{imine}	1.305(2)
Bond angles (°)	
N1-Cu1-N2	82.95(6)
N1-Cu1-O1	92.89(6)
N3-Cu1-N4	78.78(6)
N1-Cu1-N3	178.10(7)

[Cu(L1)(Phen-NH_2)](Cl) exhibits several short H···Cl contacts to the chloride counter ion, with a single anion bridging four molecules. The short contacts between the chloride anion and the copper(II) chelate are shown in Figure 5.22.

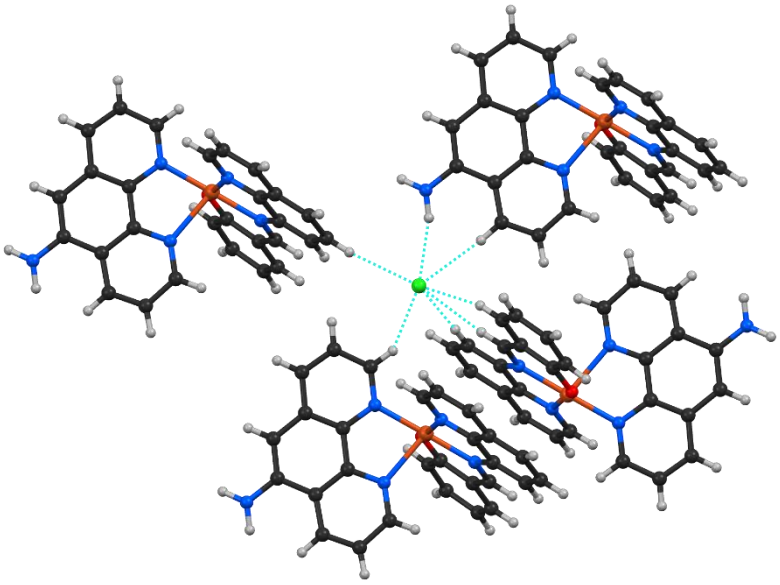

Figure 5.22: Short contacts between the chloride anion and the surrounding copper(II) chelates in [Cu(L1)(Phen-NH_2)](Cl).

The crystal structure shows seven short contacts between the chloride anion and the hydrogen atoms of the amino group, the quinoline heterocyclic ring system, the salicylideneimine moiety as well the phenanthroline co-ligand. The short contacts stabilise the crystal lattice, ultimately aiding in the crystal growth of the desired chelate. Table 5.18 provides a summary of the short contact distances for [Cu(L1)(Phen-NH_2)](Cl).

Table 5.18: Summary of the lengths of the short contacts to the chloride anion in [Cu(L1)(Phen-NH_2)](Cl).

Short contact	Length
Cl···amino H	2.410(3)
Cl···quinoline H_1	2.699(4)
Cl···quinoline H_2	2.909(6)
Cl···salicylideneimine H	2.868(3)
Cl···imine H	2.704(9)

The NH_2 group of the co-ligand is hydrogen-bonded to a chloride anion and the phenolic oxygen atom of an adjacent molecule. This complementary hydrogen bonding pattern (Figure 5.23) leads to a dimeric supramolecular structure with crystallographically imposed inversion symmetry. The hydrogen bond parameters are summarised in Table 5.19.

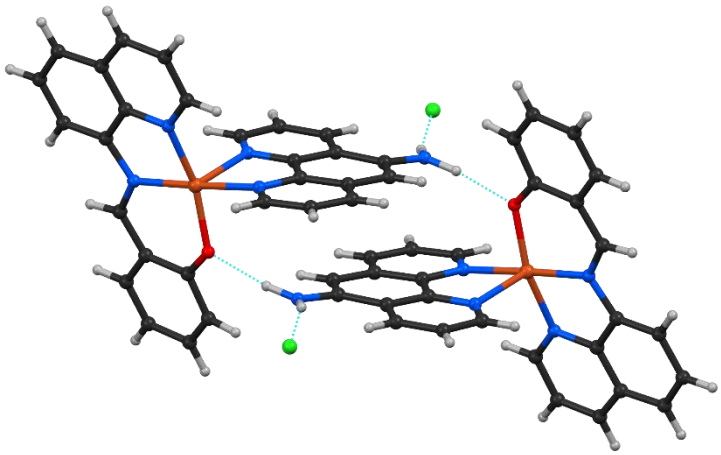

Figure 5.23: Dimeric supramolecular structure of [Cu(L1)(Phen-NH_2)](Cl) with crystallographically imposed inversion symmetry.

Table 5.19: Hydrogen bond parameters (Å, °) of [Cu(L1)(Phen-NH_2)](Cl).

Hydrogen Bond	D–H	H···A	D···A	D–H···A
N5–H102···O1	0.97(3)	2.00(3)	2.968(2)	171(3)
N5–H101···Cl1	0.96(3)	2.41(3)	3.332(2)	161(3)

These bond lengths are again shorter than the sum of the van der Waals radii, suggesting strong interactions. This is further supported by the bond angles approaching ideality.

As was investigated with the two previous heteroleptic chelates, the angle subtended by the two ligand planes was measured for [Cu(L1)(Phen-NH_2)](Cl) and showed an interesting variation.

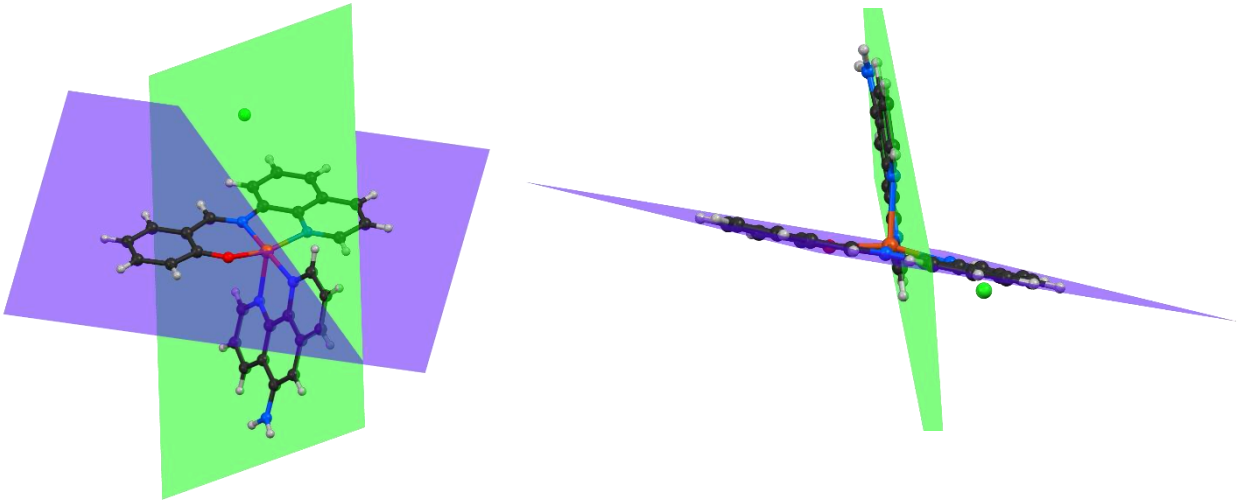

Figure 5.24: Two views of the planes generated by the two ligands for [Cu(L1)(Phen-NH_2)](Cl). The tridentate ligand plane is shown in purple and the Phen-NH_2 co-ligand plane is shown in green.

Even though [Cu(L1)(Phen)](Cl) and [Cu(L1)(Phen-NH_2)](Cl) are structurally identical, with the exception of an additional amino group, the angles between the ligand planes are significantly different. The angle between the Schiff base ligand and the Phen-NH_2 co-ligand measures 71.39°, a large deviation from [Cu(L1)(Phen)](Cl) (89.75°) and [Cu(L1)(Bpy)](Cl) (89.17°). It is likely that this deviation is to accommodate the lattice-stabilising hydrogen bonding. Another interesting difference is the deviation between the quinoline heterocyclic ring system and the salicylideneimine moiety measures 4.18°. An angle, much closer to the free ligand (NEZQAL) which was 3.81°. It would seem that the perpendicular geometry of the two former complexes requires this distortion of the tridentate ligand.

5.4 Conclusion

The solid state structures of five copper(II) chelates were determined. The copper(II) chelates all exhibited a square pyramidal coordination geometry around the metal centre which is in keeping with previously reported chelates of this class. The bond lengths and angles of interest were those around the copper(II) centre, i.e. Cu-N and Cu-O. These bond lengths were comparable with complexes within this study as well as those reported in literature. The same can be said for bond angles where all angles occur within a comparable range. Co-ligands without hydrogen bonding capabilities lead to geometries with perpendicular ligands. Hydrogen bonding lead to distortions in this geometry. The solid state interactions that these chelates are capable of, provide important information as to whether these systems will be effective DNA binders.

Chapter 6 | Computational Chemistry

6.1 Introduction

6.1.1 Fundamental Concepts of Molecular Simulations

Computational chemistry (molecular simulations) is a powerful tool which provides valuable information on the molecular geometry of compounds. It uses quantum mechanics and mathematical formulations to solve and investigate chemically relevant problems using computational simulations. Chemists frequently utilise these tools to investigate various aspects and features of molecules including the chemical reactivity, characterisation spectra (IR, NMR and UV/Vis), molecular geometry, electronic structure and substrate–enzyme interactions.[81]

Various computational methods exist such as Molecular Mechanics, *Ab Initio*, Semi-empirical calculations, Density Functional Theory (DFT) and Molecular dynamics. Density Functional Theory simulations have been used in this study to gain a deeper understanding of the experimental solid state structures. In particular, the influence of intermolecular interactions on the solid state structures determined in the crystallographic studies.[82]

To simulate the properties of interest for a chemical compound an understanding of the electron configuration of the molecule is required. Since an electron's position cannot be defined precisely, a wavefunction is utilised to calculate the electron distribution of a molecule. The wavefunction represents the probability of finding electrons in certain locations.[83] Calculating wavefunctions of molecules is not possible for any molecule larger than a hydrogen atom, therefore DFT calculations (which are based on the Schrödinger equation) use an indirect method of finding an approximate solution to the wavefunction. The method uses the electron distribution of a molecule to determine the ground-state electronic configuration. The ground-state electronic configuration is then used to calculate the wavefunction, after which various properties of a molecule can be calculated i.e. DFT finds an approximate solution to the Schrodinger equation by making certain assumptions regarding electron density of a molecule.[81, 82]

DFT simulations require the application of both a functional and a basis set. A functional is an instruction which produces a number from a set of coordinates or variables. A functional is a mathematical entity related to a function which produces a number from a function (a function of a function). The basis set is a set of atomic functions which describes the number and type of atomic orbitals which are considered in the calculation of a particular molecule.[81] Basis sets are fundamentally the region of space to which each electron is restricted. The fewer the number of restrictions on the positions of each electron, the more accurate the prediction of the molecular orbitals. The drawback is that the more degrees of freedom that are allowed, the longer the simulations take to complete.[81]

Of all modern functionals, B3LYP (which is a hybrid functional) has proven the most popular and is the functional of choice for this work.[83] B3LYP takes into account both the electron spin densities and electron spin gradients and is therefore classified as a gradient-corrected functional. This functional was coupled with the 6-311G (d,p) basis set which is restricted to atoms from H to Kr. This split valence basis set incorporates the hyperpolarisabilities for the d and p orbitals which greatly improves the accuracy of the molecular simulations.[81] The basis set 6-311G is restricted from H-Kr, but has been shown to give more accurate results than the broader basis set 3-21G, which could also be used in this study as it is applicable to atoms in the range H-Xe. The basis set 6-311G applies fewer restrictions to the electrons during the calculation and gives more accurate results, but requires greater computational time. Considering the relatively small size of the molecules of interest, the larger basis set could be applied while keeping simulations times acceptable. The 6-311G basis set is therefore an appropriate basis set for the single-ligand as well as the heteroleptic copper(II) chelates of interest.

6.1.2 Objectives

The main objective of this work is to determine the influence of intermolecular interactions in the solid state on the geometry of the metal chelates. The calculations will provide insight into the chemistry of both the single-ligand and heteroleptic copper(II) chelates. The geometry-optimised structures of the metal chelates *in vacuo* will be simulated. The vibrational frequency calculations will also be run as they are pivotal in determining whether the geometry optimisations are true global minima on the potential energy surface.

6.1.3 Experimental

The DFT simulations were run at the B3LYP/6-311G(d,p) level of theory [84, 85, 86, 87, 88, 89, 90] using *GAUSSIAN09W*.[91] The X-ray structure coordinates were used, where possible, as the input structures for the full geometry optimisations. All simulations of the copper(II) chelates excluded counter ions and solvent molecules. No restrictions were imposed during the geometry optimisations. The frequency simulations showed no negative Eigen values suggesting that all the optimised structures are true minima on the global potential energy surface. All atom numbering within this chapter corresponds with that used in Chapter 5.

6.2 Results and Discussion

6.2.1 Geometry Optimisations of Single-ligand Copper(II) Chelates

To fully understand the consequences of the methanol solvent molecule on the geometry of $[Cu(L2)Cl_2]$, the geometry of the structure (metal chelate only) was optimised in the gas phase and compared to the experimentally determined solvated and non-solvated structures. The experimental X-ray structure and simulated structure were compared using structural overlays (least squares fits) (Figure 6.2.1). The similarity of the calculated and simulated structures suggests, as indicated by the relatively small root-mean-square deviations (RMSD), the level of theory used for the calculations was appropriate and the results are likely to be reliable. The bond parameters for the experimental and calculated structures are summarised in Table 6.2.1 and Figure 6.2.1, respectively. The gas-phase structure is 47.8 kJ mol^{-1} lower in energy than the solid-state desolvated structure and 10.68 kJ mol^{-1} lower in energy than the solid state solvated structure. Surprisingly, the solvated chelate has a lower RMSD of 0.470 Å compared to the non-solvated chelate with an RMSD of 0.508 Å as well as a lower ΔE value. These data suggest that the structure has to undergo minimal deformation from the true lowest energy conformation to allow for optimum hydrogen bonding with the methanol solvate molecule. This small required deviation from the lowest energy conformation coupled with the energy gained through hydrogen bonding would suggests that the solvated structure is significantly more stable than the desolvated structure.

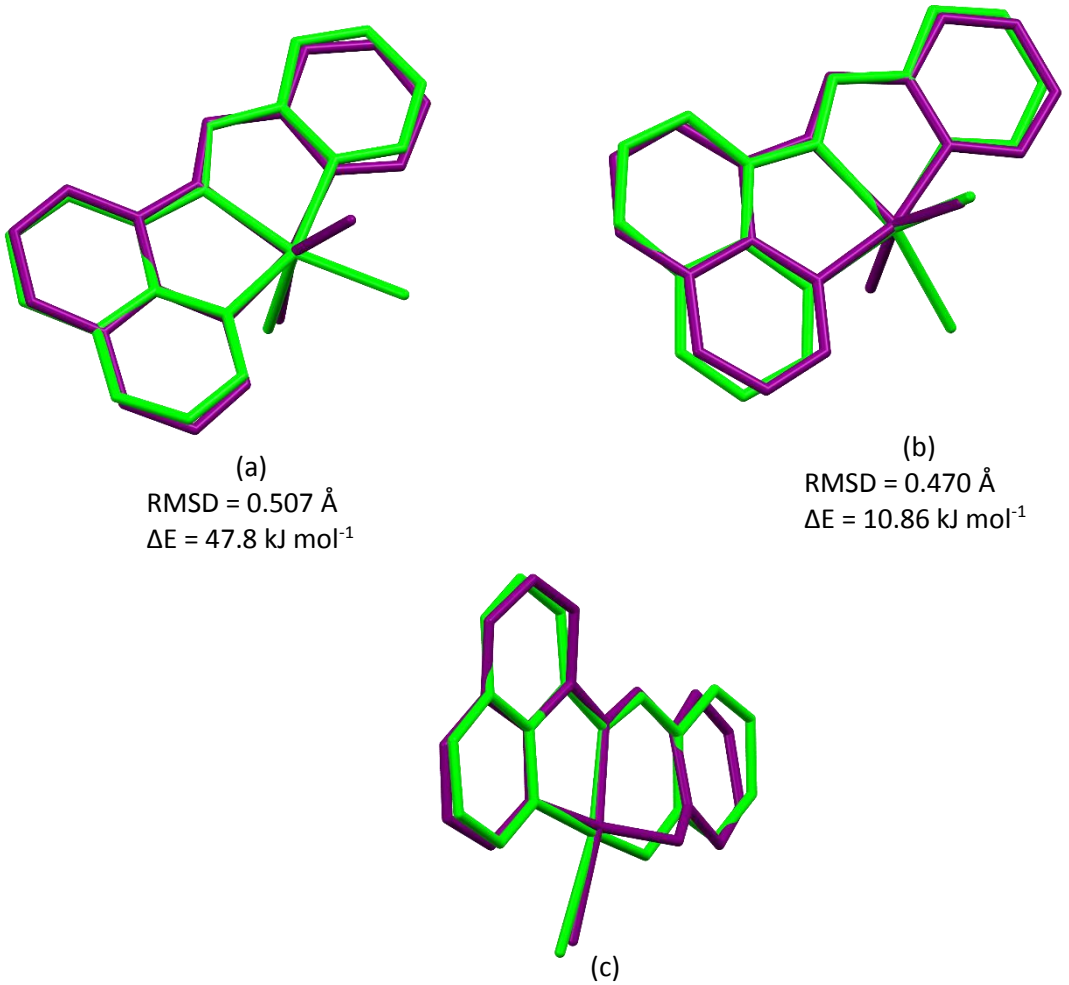

(a)
RMSD = 0.507 Å
ΔE = 47.8 kJ mol^{-1}

(b)
RMSD = 0.470 Å
ΔE = 10.86 kJ mol^{-1}

(c)
RMSD = 0.335 Å
ΔE = 31.2 kJ mol^{-1}

Figure 6.2.1: Comparison of DFT-calculated (purple) and X-ray crystal structures (green), (a) the desolvated structure of [Cu(L2)(Cl)$_2$], (b) the methanol monosolavted X-ray structure of Cu(L2)Cl$_2$] and (c) the monomer of the μ-chloro bridged structure of [Cu(L1)Cl]. Root mean square deviations (RMSDs) for all non-hydrogen atoms for each structure are indicated on the diagram (Å) along with ΔE (kJ mol^{-1}). ΔE represents the energy difference between the solid-state and gas phase structures.

Table 6.2.1: Comparison of experimental and DFT-calculated bond lengths (Å) and angles (°) for [Cu(L2)(Cl)$_2$] and [Cu(L2)(Cl)$_2$]·MeOH.

Bond lengths (Å)					
	Experimental		Calculated	Difference* (%)	Difference* (%)
	[Cu(L2)(Cl)$_2$]	[Cu(L2)(Cl)$_2$]·MeOH		[Cu(L2)(Cl)$_2$]	[Cu(L2)(Cl)$_2$]·MeOH
N1-Cu1	1.985(1)	1.989(2)	2.1133	6.07	5.88
N3-Cu1	2.046(2)	2.034(2)	1.9199	-6.57	-5.94
N2-Cu1	2.042(1)	2.027(2)	1.9125	-6.77	-5.99
Cl1-Cu1	2.4616(5)	2.5208(6)	2.2060	-11.59	-1.82
Cl2-Cu1	2.2567(6)	2.2461(5)	2.2061	-2.29	-14.26
C=N$_{imine}$	1.282(2)	1.289(2)	1.2754	-0.52	-1.07

Table 6.2.1 continued…

	Bond angles (°)				
	Experimental		Calculated	Difference* (%)	Difference* (%)
	$[Cu(L2)(Cl)_2]$	$[Cu(L2)(Cl)_2]\cdot MeOH$		$[Cu(L2)(Cl)_2]$	$[Cu(L2)(Cl)_2]\cdot MeOH$
N1-Cu1-N2	80.62(6)	80.62(6)	81.98	1.66	1.66
N1-Cu1-N3	79.27(6)	79.62(6)	81.15	2.32	1.89
N1-Cu1-Cl1	97.42(5)	96.76(5)	103.34	5.73	6.37
Cl1-Cu1-Cl2	105.26(2)	108.45(2)	153.33	31.35	29.27

*Percentage Difference = $\frac{(Calc-Exp)}{Calc}\ x\ 100$

The data in Table 6.2.1 show that the majority of the bond lengths and angles of the optimised and experimental structures compare favourably. The greatest difference in the bond angles is for angle Cl1-Cu1-Cl2. The DFT-calculated angle is 153.33° while the experimental data shows more acute angles measuring 105.26(2)° and 108.45(2)° for the solvated and non-solvated chelates, respectively. This is likely a result of the chloride ions being involved in hydrogen bonding with the methanol solvent molecule in the crystal lattice. Another key difference lies in the angles at which the two chloride ions are positioned relative to the rest of the complex. In the experimental structures Cl1 is approximately perpendicular to the complex while Cl2 is nominally co-planar with the basal plane of the complex. It would seem that the additional stability gained through the hydrogen bonding in the solid state is sufficient to offset the energy required for this deviation from the true lowest energy structure in the gas phase. Additionally, in the absence of packing constraints in the lattice, the chloro ligands can adopt a more obtuse angle which would alleviate any non-bonded repulsion between the ligands.

With respect to the bond distances, it is noted that the experimental N1-Cu1 bond length is shorter than the DFT-simulated distance. The distances between the metal centre and N2 and N3 are larger than the simulated length of 1.9199 Å. It is also interesting to note that distance to N3 is slightly longer than N2. The bond between C=N_{imine} is a double bond and is longer than the simulated distance. The Cu-Cl bond distances are significantly different in the experimental structures with one Cu-Cl bond being significantly longer than the other in both complexes. This is not seen in the simulated structure where both Cu-Cl bond lengths are very similar. All other distances lie compare favourably with the DFT calculated distances.

The solid state structure of [Cu(L1)Cl] is a dimer type structure which is bridged by two chloro ligands. Figure 6.2.1 (c) shows the experimental and DFT-optimised monomer of the chelate. The gas-phase structure is 31.2 kJ mol^{-1} lower in energy than the solid-state structure. The RMSD of 0.335 Å is relatively large for a small molecule showing that in the solid state the molecule has to undergo a relatively large deviation from the lowest energy conformation. Seemingly this energy difference is offset by the more favourable packing of the higher energy conformation. Figure 6.2.2 illustrates the least-squares fit of the experimental and the DFT-simulated structures of the μ-chloro bridged structure with an RMSD of 0.763 Å for all non-hydrogen atoms. The gas-phase structure is 68.9 kJ mol^{-1} lower in energy than the solid-state structure. The least-squares fit of the dimer structure illustrates a significant difference between the experimental and solid state structures as illustrated by the large RMSD. In the absence of packing constraints *in vacuo*, the ligands are able to adopt the lowest energy conformation. In the solid state the structure has to deviate from this true low energy structure to allow for optimal packing in the lattice.

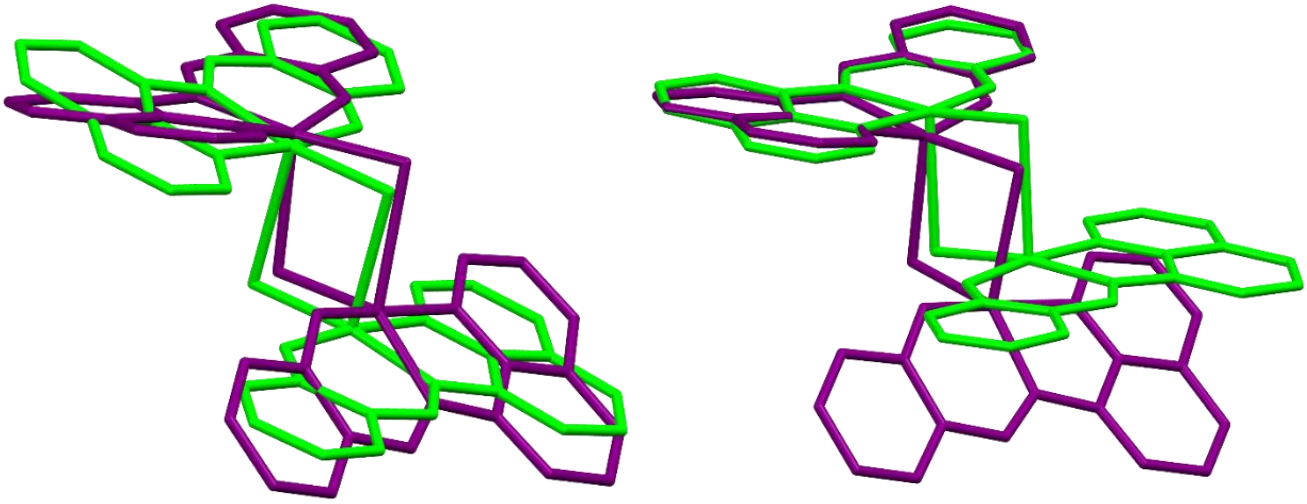

RMSD = 0.763 Å RMSD = 0.215 Å

Figure 6.2.2: Least-squares fit of the experimental (green) and DFT-simulated (purple) dimeric structure of [Cu(L1)Cl]. [Left] Molecular overlay of the entire structure. [Right] An overlay of the quinoline and salicylideneimine moiety only.

The structural overlay for [Cu(L1)Cl] (an overlay of the quinoline and salicylideneimine moiety only) shows a RMSD of 0.215 Å which is lower than the corresponding molecule overlay. The lower RMSD confirms that the quinoline and salicylideneimine region of the calculated structure has been accurately simulated when compared to the experimental structure. The angle subtended by the bridged chloro ligands is responsible for the large variation in the

experimental and calculated structures. Table 6.2.2 provides a comparison of bond lengths and bond angles for [Cu(L1)(Cl)].

Table 6.2.2: Comparison of experimental and DFT-calculated bond lengths (Å) and bond angles (°) for the dimer of [Cu(L1)(Cl)].

Bond lengths (Å)			
	Experimental	Calculated	Difference (%)
Cu1-N1	1.973(3)	1.9900	0.85
Cu1-N2	2.002(3)	2.0082	0.31
Cu1-O1	1.908(3)	1.9322	1.25
Cu1-Cl1	2.2924(9)	2.3251	1.41
Cu1-Cl1*	2.8151(8)	2.6023	-8.18
C10-N1	1.305(5)	1.3053	0.02
Bond angles (°)			
	Experimental	Calculated	Difference (%)
N1-Cu1-N2	82.3(1)	82.05	-0.30
N1-Cu1-O1	93.7(1)	90.87	-3.11
N2-Cu1-Cl1*	95.21	93.87	-1.43
O1-Cu1-Cl1	89.09	90.38	1.43
Cl1-Cu1-Cl1*	95.60(3)	90.86	-5.22

Percentage Difference = $\frac{(Calc-Exp)}{Calc}\ x\ 100$

The most noticeable difference in the bond lengths is noted for the Cu1-Cl1* with Cl1* being the axial chloro ligand. The largest percentage difference with the experimental and calculated bond angles occurs with the angles associated with the chloride atoms. The experimental angle Cl1-Cu1-Cl1* measures 95.60(3)° which is significantly larger than the calculated angle which measures 90.86°. With the exception of the bond parameters involving the chloro ligands, the similarity of the selected bond lengths and bond angles for the experimental and geometry-optimised structures suggests that the chosen level of theory was appropriate.

No crystal structure was obtained for $[Cu(L)(Cl)_2]$, therefore DFT simulations are important to determine the geometry of the chelate. The geometry of the chelate was optimised as a gas-phase model. No negative Eigen values were obtained, thus the chelate has been optimised to the energy minimum on the global potential energy surface. The geometry-optimised structures for the copper(II) chelate is shown in Figure 6.2.3.

A summary of the calculated bond lengths and bond angles defining the coordination sphere of the copper(II) chelate are given in Table 6.2.3. Figure 6.2.3 is a partially labelled diagram showing the distorted square pyramidal geometry within the coordination sphere of the copper(II) centre.

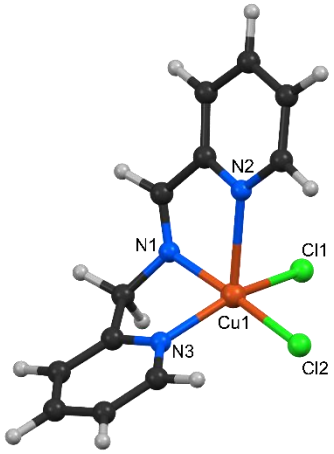

Figure 6.2.3: Partially labelled DFT-optimised structure showing the distorted square pyramidal geometry of $[Cu(L)(Cl)_2]$.

Table 6.2.3: A summary of the calculated bond lengths (Å) and bond angles (°) for $[Cu(L)(Cl)_2]$.

Bond lengths (Å)		Bond angles (°)	
N1-Cu1	1.909	N1-Cu1-N2	80.31
N3-Cu1	1.981	N1-Cu1-N3	75.47
N2-Cu1	2.420	N1-Cu1-Cl1	153.05
Cl1-Cu1	2.181	Cl1-Cu1-Cl2	92.59
Cl2-Cu1	2.141		
$C=N_{imine}$	1.278		

The structure of $[Cu(L)(Cl)_2]$ shows an interesting geometry around the copper(II) centre when compared to its closely related counterpart $[Cu(L2)(Cl)_2]$. The basal plane of $[Cu(L2)(Cl)_2]$ comprises atoms N1, N2, N3 and Cl2, with Cl1 being the apical atom in the square pyramidal geometry. Correspondingly, the Cu1-Cl1 bond length is longer than that of Cu1-Cl2. Figure 6.2.3 shows that the basal plane of $[Cu(L)(Cl)_2]$ consists of N1, N3, Cl1 and Cl2, with the apical atom being N2. Similarly, the Cu1-N2 bond which measures 2.420 Å, is significantly larger than the corresponding bond lengths of Cu1-N1 (1.909 Å) and Cu1-N3 (1.981 Å). The additional flexibility afforded by the sp^3 hybridised methylene bridging atom of [Cu(L)Cl] compared to the rigid aromatic nature of [Cu(L2)Cl] has allowed for this significantly different geometry.

6.2.2 Geometry Optimisation of the Heteroleptic Copper(II) Chelates

Geometry optimisations and frequency calculations were performed on all copper(II) chelates using the level of theory described above. The absence of negative Eigen values suggests that the geometry optimised structures were true minima on the global potential energy surface. The least-squares fits of the three heteroleptic complexes are shown in Figure 6.2.4. The RMSDs for all non-hydrogen atoms indicate that the experimental and calculated structures are in reasonably good agreement.

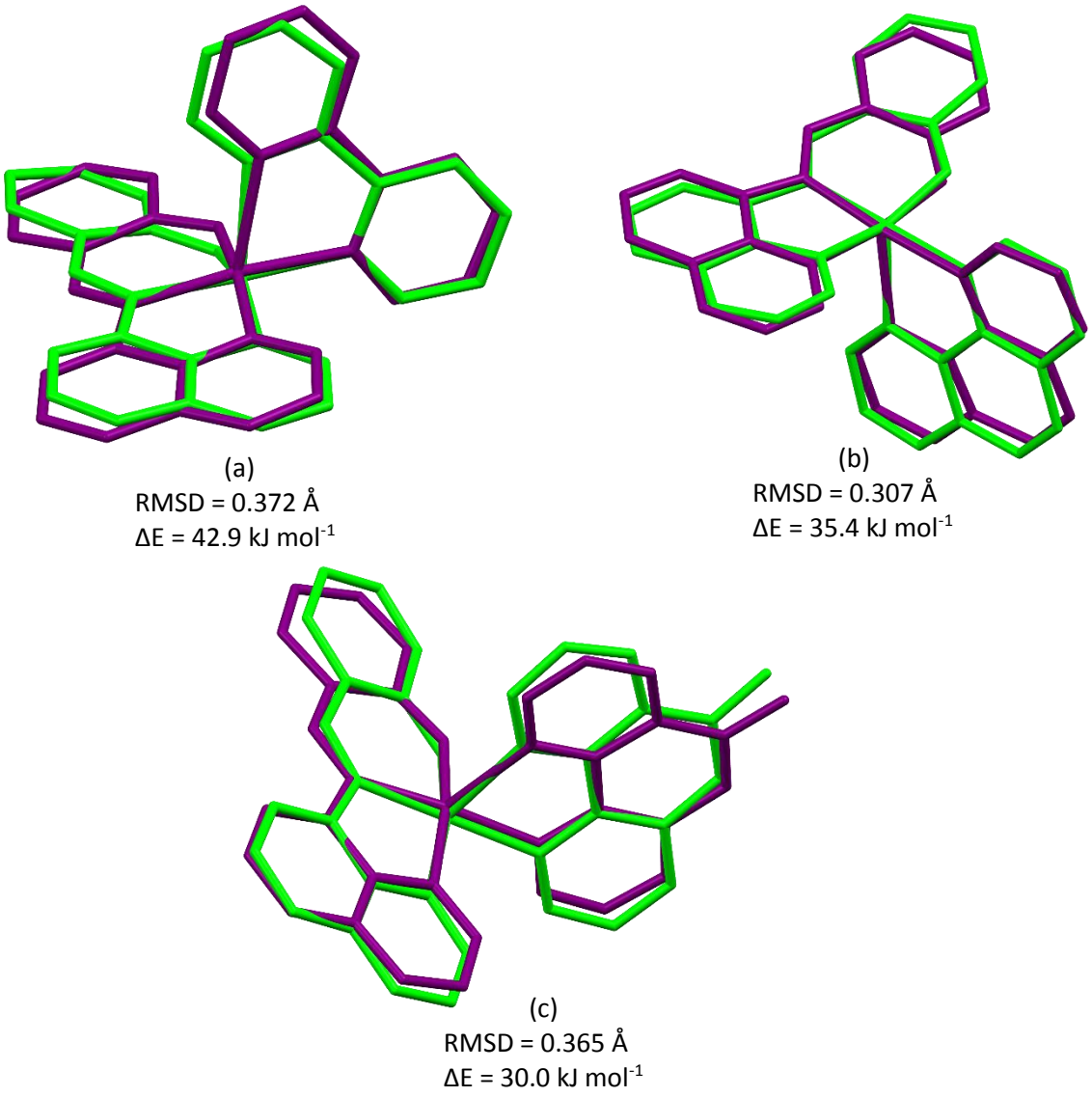

Figure 6.2.4: Comparison of DFT-calculated (purple) and X-ray crystal structures (green) of structures (a) [Cu(L1)(Bpy)](Cl), (b) [Cu(L1)(Phen)](Cl) and (c) [Cu(L1)(Phen-NH_2)](Cl). RMSDs for all non-hydrogen atoms for each structure are indicated on the diagram (Å) along with ΔE values (kJ mol^{-1}).

The RMSDs for the heteroleptic complexes are in most cases smaller than those of the single-ligand complexes. The bidentate ligands have fewer degrees of freedom and allow for fewer conformational distortions. Hence there is greater similarity between the experimental and calculated structures.

The RMSD for [Cu(L1)(Bpy)](Cl) measures 0.372 Å with the gas-phase structure being 42.9 kJ mol^{-1} lower in energy than the solid-state structure. The similarity of the calculated and experimental structures suggests the level of theory used for the calculations was appropriate and the simulations are likely to be reliable. The structural overlay for [Cu(L1)(Bpy)](Cl) (an overlay of the quinoline and salicylideneimine moiety only) shows an RMSD of 0.133 Å and is depicted in Figure 6.2.5. This shows a similar trend to that observed previously: the most significant difference between the structures lies in the angle between the tridentate ligand and the co-ligands.

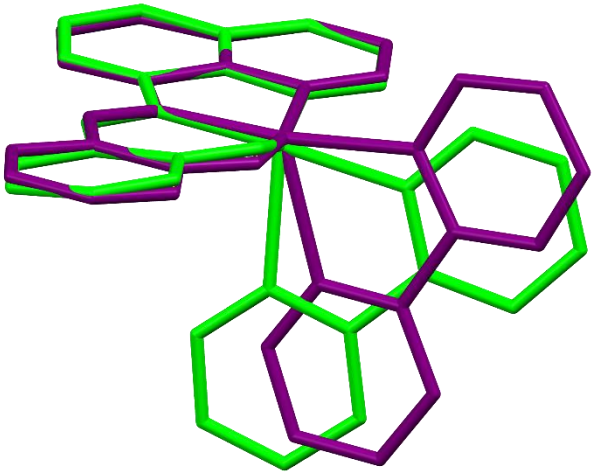

Figure 6.2.5: Structural overlay of the experimental (green) and DFT-simulated (purple) for the quinoline and salicylideneimine moiety only of [Cu(L1)(Bpy)](Cl).

A summary of key calculated and experimental bond lengths and bond angles is given in Table 6.2.5 along with the percentage difference between these data.

Table 6.2.4: Comparison of experimental and DFT-calculated bond lengths (Å) and bond angles (°) for [Cu(L1)(Bpy)](Cl).

Bond lengths (Å)			
	Experimental	**Calculated**	**Difference (%)**
Cu1-N1	2.214(4)	2.295	3.53
Cu1-N2	2.017(3)	2.076	2.84
Cu1-N3	2.022(3)	2.030	0.39
Cu1-N4	1.954(3)	1.973	0.96
Cu1-O1	1.931(2)	1.911	-1.05
C=N_{imine}	1.311(5)	1.314	0.23
Bond angles (°)			
	Experimental	**Calculated**	**Difference (%)**
N1-Cu1-N2	78.1(1)	75.64	-3.25
N4-Cu1-O1	93.3(1)	93.12	-0.19
N3-Cu1-N4	82.6(1)	82.57	-0.04
N1-Cu1-N4	97.80(1)	111.49	12.28

Percentage Difference = $\frac{(Calc-Exp)}{Calc}\ x\ 100$

From Table 6.2.4 it can be concluded that all bond lengths are in good agreement as indicated by the small percentage differences. From the structural overlay in Figure 6.2.5 it is evident that the quinoline and salicylideneimine region of the calculated structure has been accurately simulated when compared to the experimental structure. The key difference lies in the angle N1-Cu1-N4 which shows a very large deviation between the gas-phase and solid state structures. The angle is larger for the gas-phase structure by 13.39°; this significantly changes the overall geometry of the chelate. In the gas phase, the copper(II) chelate is not restricted by lattice packing and so the geometry optimisation yields a chelate structure with the lowest steric strain and correspondingly the lowest energy.

The RMSD for [Cu(L1)(Phen)](Cl) measures 0.307 Å with the gas-phase structure being 35.4 kJ mol^{-1} lower in energy than the solid-state structure (Figure 6.2.4). The structural overlay for [Cu(L1)(Phen)](Cl) (an overlay of the quinoline and salicylideneimine moiety only) shows a RMSD of 0.174 Å and is illustrated in Figure 6.2.6.

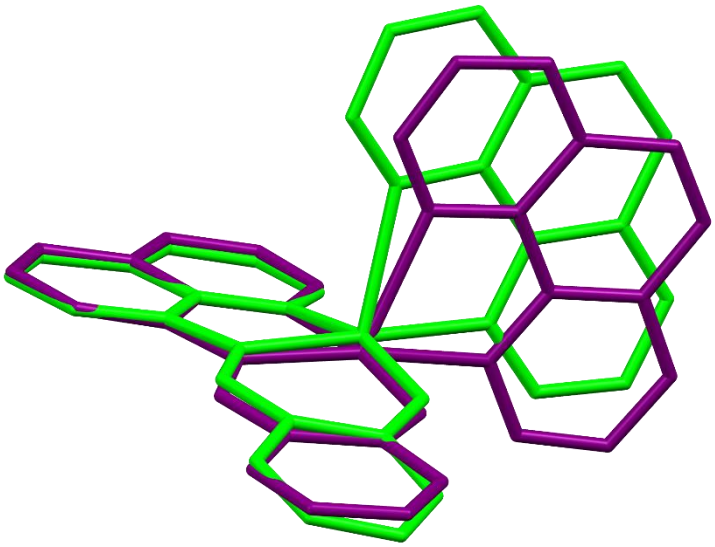

Figure 6.2.6: Structural overlay of the experimental (green) and DFT-simulated (purple) of the quinoline and salicylideneimine moiety only for [Cu(L1)(Phen)](Cl).

Figure 6.2.6 shows a similar result to that previously discussed where the quinoline and salicylideneimine regions are in good agreement with each other in the gas phase and the solid state structures. The most significant deviations are observed in the angle between the co-ligand and primary ligand. The relevant bond lengths and bond angles for [Cu(L1)(Phen)](Cl) are summarised in Table 6.2.5 and Table 6.2.6. The consequence of this small deviation, however, is a significantly different molecular geometry.

Table 6.2.5: Comparison of experimental and DFT-calculated bond lengths (Å) for [Cu(L1)(Phen)](Cl).

Bond lengths (Å)			
	Experimental	**Calculated**	**Difference (%)**
Cu1-N1	1.962(3)	1.972	0.51
Cu1-N2	2.014(3)	2.031	0.84
Cu1-N3	2.293(3)	2.331	1.63
Cu1-N4	2.034(3)	2.071	1.79
Cu1-O1	1.911(3)	1.909	-0.10
C=N_{imine}	1.287(4)	1.313	1.98

Table 6.2.6: Comparison of experimental and DFT-calculated bond angles (°) for [Cu(L1)(Phen)](Cl).

	Bond angles (°)		
	Experimental	**Calculated**	**Difference (%)**
N1-Cu1-N2	83.05(1)	82.57	-0.58
N1-Cu1-O1	93.42(1)	93.15	-0.29
N3-Cu1-N4	77.52(1)	76.62	-1.17
N1-Cu1-N3	96.74(1)	109.49	11.64

Percentage Difference = $\frac{(Calc-Exp)}{Calc}\ x\ 100$

All bond angles and bond lengths around the coordination sphere lie within good agreement of each other in the gas-phase and solid state structures. This is confirmed by the small percentage differences which range from 0.10 – 1.98 %. The exception is the N1-Cu1-N3 bond angle which measures 96.74(1)° in the solid state while the *in vacuo* structure shows a corresponding angle of 109.49°. The reason for the deviation in the bond angle is likely that the solid state structure has to deviate from the lowest energy structure to allow for optimal packing in the lattice.

The most interesting of the three structures is [Cu(L1)(Phen-NH_2)](Cl) since this is the only heteroleptic compound with the potential to hydrogen bond. This is significant as hydrogen bonding has been previously shown to lead to marked deviations between the lowest energy structures and those observed experimentally.[51] The RMSD for [Cu(L1)(Phen-NH_2)](Cl) measures 0.365 Å with the gas-phase structure being 30.0 kJ mol^{-1} lower in energy than the solid-state structure. The structural overlay for [Cu(L1)(Phen-NH_2)](Cl) (an overlay of the quinoline and salicylideneimine moiety only) shows a RMSD of 0.0896 Å and is illustrated in Figure 6.2.7.

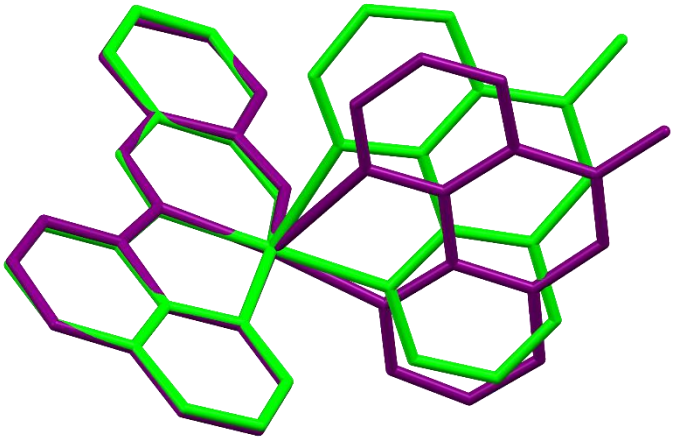

Figure 6.2.7: Structural overlay of the experimental (green) and DFT-simulated (purple) of the quinoline and salicylideneimine moiety only for [Cu(L1)(Phen-NH_2)](Cl).

As was observed with the previous two heteroleptic chelates, the quinoline and salicylideneimine moieties have a low RMSD value indicating that the geometry optimisation results are reliable. From the crystallographic studies, it was observed that the NH_2 group was involved in hydrogen bonding with the chloride counter ion as well as the oxygen atom of the Schiff base ligand. The molecule has seemingly had to undergo minimal deviation from the lowest energy conformation to allow for optimum hydrogen bonding. This is an unusual result and suggests that the hydrogen bonding groups are coincidentally pre-organised for optimum hydrogen bonding. This is an encouraging result as it shows that the complex will likely be able to hydrogen bond with the DNA helix with minimal distortion, stabilising the DNA/drug conjugate. Key bond lengths and bond angles are summarised in Table 6.2.7.

Table 6.2.7: Comparison of experimental and DFT-calculated bond lengths (Å) and angles (°) for [Cu(L1))(Phen-NH_2)](Cl).

	Bond lengths (Å)		
	Experimental	**Calculated**	**Difference (%)**
Cu1-N1	1.957(2)	1.974	0.86
Cu1-N2	2.010(1)	2.032	1.08
Cu1-N3	2.013(2)	2.061	2.33
Cu1-N4	2.241(2)	2.333	3.94
Cu1-O1	1.940 (9)	1.912	-1.46
C=N_{imine}	1.305(2)	1.314	0.68

Table 6.2.7 continued…

	Bond angles (°)		
	Experimental	**Calculated**	**Difference (%)**
N1-Cu1-N2	82.95(6)	82.51	-0.53
N1-Cu1-O1	92.89(6)	93.04	0.16
N3-Cu1-N4	78.78(6)	76.56	-2.90
N1-Cu1-N4	100.15(6)	109.05	8.16

Percentage Difference = $\frac{(Calc-Exp)}{Calc}\ x\ 100$

Table 6.2.7 shows a summary of the bond angles and lengths defining the coordination sphere of the copper(II) ion. The calculated bond lengths are all similar, as expected, with Cu1-N4 being slightly longer in the gas phase. Once again, the bond angle of interest, N1-Cu1-N4, is larger in the gas phase than in the solid state structure. This angle deviation is ubiquitous in all six structures studied. This is an interesting result as it shows that the simulated structures are tending towards a trigonal bipyramidal structure as opposed to the square pyramidal structure observed in the solid state. These geometries are both well known for copper(II) chelates, however, trigonal bipyramidal structures tend to be lower in energy as there is reduced steric strain in the complexes. It therefore stands to reason that in the gas phase, in the absence of packing constraints, the molecules are tending as far as possible towards a trigonal bipyramidal geometry.

6.3 Conclusions

The geometry optimisations for all copper(II) chelates were performed at the B3LYP/6-311G(d,p) level of theory. A good correlation was observed between the gas phase and solid state structures for all the chelates. DFT simulations were used to determine to the structure of $[Cu(L)(Cl)_2]$ which proved to be difficult to crystallise.

Similar trends emerged for all the copper(II) chelates studied; both the single-ligand and heteroleptic chelates. The geometry of the tridentate ligands coordinated to the copper(II) ion was consistently in good agreement with the experimental data. The main difference between the experimental (solid state) and simulated (gas phase) structures lies in the angle subtended by the co-ligands. In all cases this angle was more obtuse in the gas phase models showing the

lowest energy conformations were tending towards a trigonal bipyramidal geometry. Seemingly more favourable packing of the square pyramidal structures in the solid state was enough to offset the energy difference between the lowest energy conformations and those observed experimentally. The hydrogen bonding of [Cu(L1)(Phen-NH_2)]Cl did not (surprisingly) lead to any significant structural distortions in the solid state.

Overall, it can be concluded that the B3LYP/6-311G(d,p) level of theory which was used for the DFT simulations was appropriate and the data simulated for the gas phase structures was reliable and in good agreement with the solid state structures.

Chapter 7 | Biological studies

7.1 Introduction

The square pyramidal copper(II) chelates synthesised in this work have been designed to act as chemotherapeutic agents, exerting their cytotoxicity through DNA binding (intercalation and/or groove binding) interrupting DNA replication. This will in turn lead to cell apoptosis. The cytotoxic effects will be further enhanced by the ability of the copper(II) metal centre to catalyse hydroxyl radical production. Previous discussion highlighted the various chemical properties of the copper(II) chelates which make them suitable for the development of chemotherapeutic agents including their ctDNA binding affinities and ability to produce ROS. In the development of potential chemotherapeutic agents, it is vital to investigate the cytotoxicity by screening the chelates against a wide range of cancer cell lines. The copper(II) chelates presented in this work was screened *in vitro* against a panel of four human cell lines by the Advanced Materials Division at MINTEK in South Africa. The cell screening will not only show how effectively the metal chelates control the proliferation of tumour cells, but will also show any preference the copper chelates may have towards particular cell lines. This specificity is key as preferential cytotoxicity towards specific cell lines will reduce the side-effects associated with chemotherapy.

In this study, the chelates were screened against a panel of three human cancer cell lines and one normal human cell line. The IC_{50} values for each chelate were measured. The cell lines of choice represent some of the most prevalent forms of cancer and also form a representative cross-section of the more than 200 forms of cancer. Screening against a normal human cell line was carried out to investigate the cytotoxic effects on normal healthy tissue. The cell lines are:

1. Human embryo kidney cells (Normal)	HEK293
2. Human histiocytic lymphoma	U937
3. Human renal carcinoma	TK-10
4. Human leukaemia T cells	MT-4

Daunorubicin is a commercially available anticancer agent which acts as a DNA intercalator and topoisomerase II poison. The dose response curve of a central nervous system cancer cell

line with the chemotherapeutic agent Daunorubicin is illustrated in Figure 7.1.1. The growth percentage is the growth of the inoculated tumour cell line relative to a control batch. It is measured as a net increase or decrease in the mass of protein.[92]

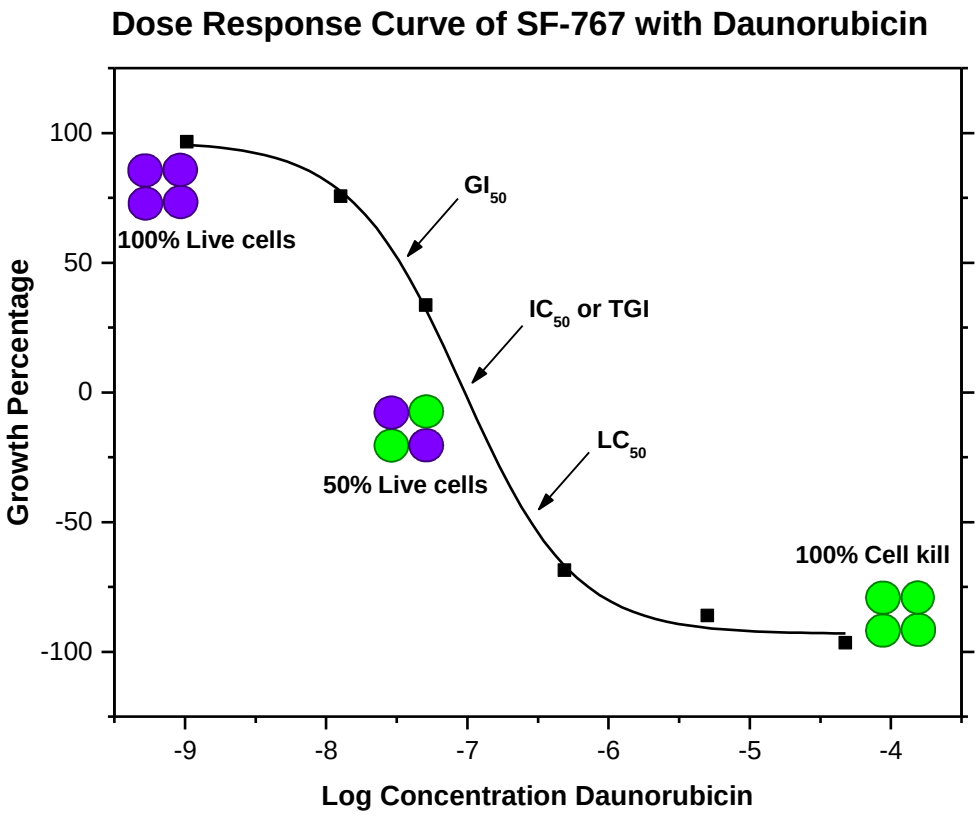

Figure 7.1.1: Dose-response curve of a central nervous system cancer cell line with the chemotherapeutic.

The cytotoxicity of a drug can be measured *via* three dose response parameters, each being the concentration of a drug required to reduce cell proliferation to a specified extent. These dose parameters are:

- GI_{50} value: concentration of the compound where there is 50% growth inhibition compared to the control. This is a 50% reduction in the nett protein increase in control cells during the drug incubation.
- IC_{50} value: concentration of the compound at which there is total growth inhibition. There is no net increase in the quantity of protein at the end of the experiment.
- LC_{50} value: concentration of the compound resulting in a 50% reduction in the measured protein at the end of drug treatment compared with the beginning. This indicates a net loss of cells following treatment.[92]

A great deal of research has been carried out where the cytotoxic effects of several copper chelates were screened against various human cancer cell lines. A study by Lu *et. al.* screened two closely related copper(II) chelates to those of this study against lung adenocarcinoma cancer cells (A549).[93]

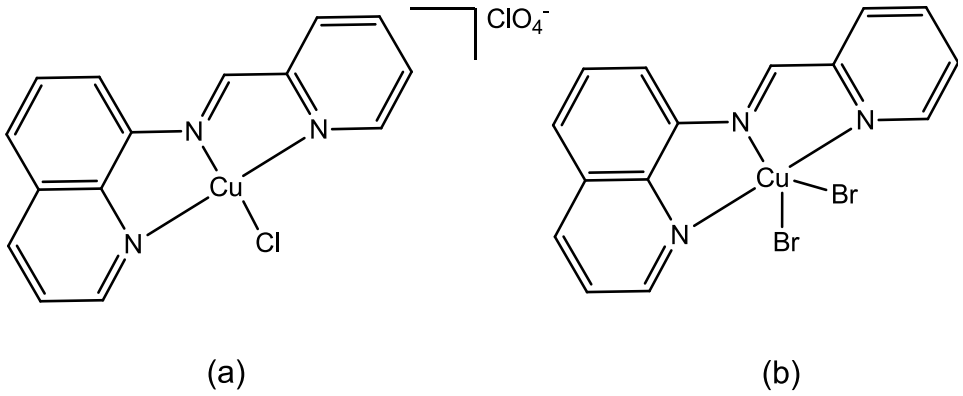

Figure 7.1.2: Closely related copper(II) chelates (a) [Cu(L)Cl](ClO$_4$) and (b) [Cu(L)Br$_2$] which exhibit cytotoxic effects against the cancer cell line A549.[2]

The -log IC_{50} values for [Cu(L)Cl](ClO$_4$) and [Cu(L)Br$_2$] as well as that of cisplatin against A549 are summarised in Table 7.1.1. The –log IC_{50} values indicate that the two copper(II) chelates have great potential to act as anticancer agents having a higher activity than cisplatin; the current industry standard for metallodrugs.

Table 7.1.1: -log IC_{50} values (µM) of similar copper(II) chelates and cisplatin against cancer cell line A549.[2]

Compound	Cell line A549
[Cu(L)Cl](ClO$_4$)	6.04
[Cu(L)Br$_2$]	6.37
Cisplatin	5.38

A study by Fernandes *et. al.* investigated the cytotoxicity of a range of novel copper(II) chelates against two human leukemia cell lines, acute monocytic leukemia (THP-1) and histiocytic lymphoma (U937). One of these copper(II) chelates, [(H$_2$L2)Cu(µ-Cl)$_2$Cu(H$_2$L2)]Cl$_2$, is shown in Figure 7.1.3.

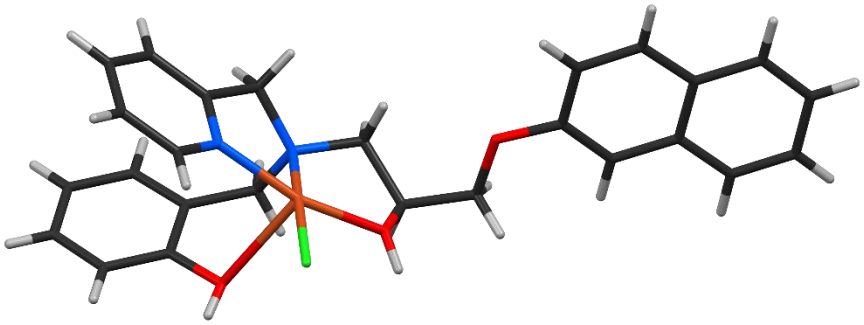

Figure 7.1.3: Solid state structure of $[(H_2L2)Cu(\mu\text{-}Cl)_2Cu(H_2L2)]Cl_2$. A potential copper(II)-based chemotherapeutic agent.

The study revealed that the copper(II) chelate, $[(H_2L2)Cu(\mu\text{-}Cl)_2Cu(H_2L2)]Cl_2$ was the most cytotoxic of the chelates in the study. Comparative studies were also carried out with cisplatin on the two cell lines, THP-1 and U937. The copper chelate exerted a potent inhibitory effect on the growth of THP-1 and U937 cell lines. The -log IC_{50} values were reported to be 4.95 µM (THP-1) and 5.09 µM (U937). This is an improvement over cisplatin for cell line U937 (4.79 µM) and a comparable activity against THP-1 (4.92 µM).

These selected data highlight the potential of copper(II) chelates as chemotherapeutic agents. In addition to the cell lines mentioned above, copper(II) compounds similarly have promising chemotherapeutic effects over a wide range of human cancer cell lines. As copper is an endogenous metal it is also possible that this enhanced activity towards tumour cells will be accompanied by lower toxicity towards healthy cells.

7.2 Experimental

The cytotoxic effect of the copper(II) compounds were evaluated in four human cell lines (TK-10, HEK293, U937 and MT-4). The assay endpoint was determined via the Cell Titer Aqueous Non-Radioactive assay.[94, 95] A 96 well microtiter plate was seeded with cells at a low passage number, at a concentration of 2×10^5 cells mL^{-1} in a total volume of 100 µL complete medium. The media contained 10% foetal bovine serum (FBS, Highveld Biological, R.S.A) and necessary antibiotics. After an incubation of 24 hours at 37 °C and 5% CO_2, the test compounds were added in two-fold serial dilutions for a total of 8 concentrations (100 - 0.78 µM). After an incubation of 96 hours, 10 µL of the Cell Titer solution was added to each well; the contents were gently mixed and the plates incubated under the previously described conditions. The plates were read at time intervals of 2 and 4 hours at an absorbance wavelength of 490 nm on a microplate reader (xMarkTM, Bio-Rad). IC_{50} values were determined as the concentration of the test substance required to reduce cell viability by 50% using OriginPro® version 8.0 software (OriginLab Corporation, Northampton, MA, USA). The cell screening experiments were performed at Mintek (South Africa).

7.3 Results and Discussion

7.3.1 Cytotoxic Activity of the Copper(II) Chelates

The IC_{50} values measured for the six synthesised copper(II) chelates against a representative panel of four human cell lines (three neoplastic and one healthy) are reported in Table 7.3.1.

Table 7.3.1: The IC_{50} values (μM) of the copper(II) chelates against three human cancer cell lines and one healthy human cell line.

Cell line	**HEK293**	**TK-10**	**U937**	**MT-4**	
	Human embryo kidney cells	Human renal carcinoma	Human lymphoblast lung cells	Human leukaemia T cells	Mean IC_{50} Value of cancer cells
$[Cu(L)(Cl)_2]$	3.18	-	3.22	1.16	2.19 ± 1.45
[Cu(L1)(Cl)]	5.66	20.00	24.64	11.28	18.64 ± 6.78
$[Cu(L2)(Cl)_2]$	3.43	-	5.06	1.30	3.18 ± 2.66
[Cu(L1)(Bpy)](Cl)	6.95	8.62	5.67	4.73	6.34 ± 2.03
[Cu(L1)(Phen)](Cl)	11.08	3.65	11.18	4.18	6.33 ± 4.20
$[Cu(L1)(Phen\text{-}NH_2)](Cl)$	4.65	3.95	17.02	4.00	8.32 ± 7.53

In General, compounds with lower IC_{50} values are more cytotoxic against the cancer cell lines. This data is counterintuitive, thus –log IC_{50} values are calculated. The lower the IC_{50} value of the copper(II) chelates, the larger its –log IC_{50} value. This allows for a clearer graphical representation of the data. Figure 7.3.1 shows a bar graph of the –logIC_{50} values of the metal chelates.

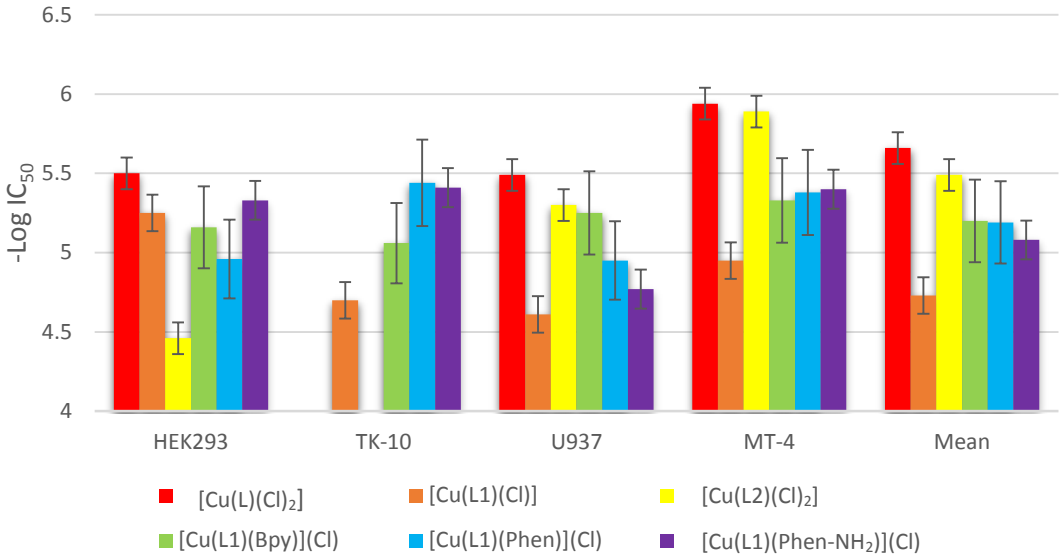

Figure 7.3.1: The -log IC_{50} values for the copper(II) chelates against four cell lines and their mean cytotoxicity.

The data in Figure 7.3.1 illustrates that each compound has a unique cytotoxicity profile (i.e. each cell line responds differently to the drug candidate) and confirms that the compounds are genuine chemotherapeutics with a well-defined mechanism of action.

HEK293 is a normal human cell line and was used a control in this study. The cytotoxic activity of the copper chelates towards the normal healthy cells illustrates the need for targeted drug delivery. The copper(II) chelates are similarly toxic to both healthy and tumour cells. By incorporating biomarkers (such as biotin) into the drug design it will ensure a higher uptake of the drug in neoplastic over healthy tissue. An interesting point highlighted by the data in is that $[Cu(L2)Cl_2]$ shows a significantly reduced cytotoxicity towards the healthy cell line while showing good toxicity towards tumour cell lines. This suggests that it may be a more suitable primary ligand for the development of the next generation of heteroleptic complexes. The reason for the reduced cytotoxicity is not clear, though it may be related to the reduced aromaticity and associated reduction in DNA binding affinity.

The copper chelates all show the greatest cytotoxicity towards the leukaemia cell line MT-4. This suggests that the compounds could be most suitable for the treatment of this particular class of cancer. It would therefore be pertinent to test the compounds against a wider variety of leukaemia cell lines in future work. It is noteworthy that [Cu(L1)(Cl)] is the least cytotoxic of all the chelates. The addition of a co-ligand is required to increase the cytotoxicity. If the same trend holds for the other single-ligand chelates then the addition of co-ligands to $[Cu(L)Cl_2]$ could lead to a potent chemotherapeutic. $[Cu(L1)(Phen\text{-}NH_2)](Cl)$ shows modestly enhanced

activity when compared to [Cu(L1)(Phen)](Cl). This is likely due to the NH_2 group's hydrogen bonding capabilities which stabilises the DNA/Drug conjugate.

As previously discussed, the copper(II) chelates were designed to bind DNA as a key step to inhibit cell replication. A comparison of the DNA binding affinities and cytotoxicities is therefore relevant. Table 7.3.2 shows (rather unexpectedly) little relationship between DNA binding affinity and cytotoxicity. In the case of $[Cu(L)(Cl)_2]$, this chelate exhibits the highest cytotoxicity of the screened copper chelates, however, it possesses one of the lowest DNA binding affinities. Chelate [Cu(L1)(Cl)] possessed the lowest cytotoxicity, but had the highest DNA binding affinity. This shows that the mechanism of action is more complex than DNA binding alone. The redox activity of the copper(II) ion is therefore likely to be a key component in the cytotoxicity. Ligands which are more flexible, such as in complex $[Cu(L)Cl_2]$, may allow for the geometric changes required for a transition from copper(II) to copper(I) since each of these metal ions have different preferences for coordination geometry.

Table 7.3.2: Relationship between the cytotoxicity and competitive EB-DNA binding affinities of the copper(II) chelates.

Most effective					Least effective
Cytotoxicity: *in vitro* cell screening					
$[Cu(L)(Cl)_2]$	$[Cu(L2)(Cl)_2]$	[Cu(L1)(Bpy)](Cl)	$[Cu(L1)(Phen\text{-}NH_2)](Cl)$	[Cu(L1)(Phen)](Cl)	[Cu(L1)(Cl)]
EB-ctDNA competitive binding affinities					
[Cu(L1)(Cl)]	[Cu(L1)(Phen)(Cl)]	$[Cu(L1)(Phen\text{-}NH_2)(Cl)]$	[Cu(L1)(Bpy)(Cl)]	$[Cu(L)(Cl_2)]$	$[Cu(L2)(Cl_2)]$

The data in Figure 7.3.1 and Table 7.3.1 shows that the cytotoxicity of the metal chelates varies significantly. The cytotoxicity of each chelate also varies against each cell line. The lack of correlation between the cytotoxicity profile and the DNA binding affinities suggests that the mechanism of action of the chelates is more complicated than anticipated. The single-ligand copper(II) chelates are also more cytotoxic than the heteroleptic copper(II) chelates. The opposite is observed with the DNA binding studies which showed the heteroleptic chelates exhibited stronger binding affinities compared to the single-ligand chelates. A stated above the heteroleptic chelates may more effectively stabilise the metal ion, reducing the production of ROS and ultimately reducing the cytotoxicity.

Another interesting trend is noted in both the cytotoxicity and DNA binding affinities of the single-ligand copper(II) chelates. $[Cu(L)(Cl)_2]$ and $[Cu(L2)(Cl)_2]$ both contained *N,N',N''* donor sets. Both these chelates were the most active in the cell screening but were the weakest DNA

binders. [Cu(L1)(Cl)] contained *N,N',O* donor atoms and displayed contrasting results. [Cu(L1)(Cl)] was the least active in the cell screening, but had the highest DNA binding affinity. $[Cu(L2)(Cl)_2]$ and [Cu(L1)(Cl)] are structurally comparable with the only difference between the two chelates being the donor atoms to the copper(II) metal centre. This observation suggests that the choice of donor atoms on the primary ligand system is significant and may have an impact on the cytotoxicity and DNA binding affinities.

The $-\log IC_{50}$ values of the copper(II) chelates for cell lines TK-10 and U937 as well as those of cisplatin, carboplatin and bleomycin (as acquired from the National Cancer Institute database and Su *et. a.l.*)[96] are summarised in Table 7.3.3. Figure 7.3.2 illustrates the cytotoxicity profile of the copper(II) chelates with three commercially available chemotherapeutic agents.

Table 7.3.3: The -log IC_{50} values of the copper(II) chelates as well as cisplatin, carboplatin and bleomycin.[5]

Compound	TK-10	U937
[Cu(L1)(Cl)]	4.70 ± 2.37	4.61 ± 5.56
[Cu(L1)(Bpy)](Cl)	5.06 ± 2.39	5.25 ± 0.14
[Cu(L1)(Phen)](Cl)	5.44 ± 0.92	4.95 ± 2.41
[Cu(L1)(Phen-NH_2)](Cl)	5.41 ± 0.54	4.77 ± 1.46
Cisplatin	4.91	5.70
Carboplatin	3.60	5.26
Bleomycin	4.88	-

Cisplatin and its analogue carboplatin are commonly used as industry standards against which anticancer agents are compared due to its high anticancer activity.[97] Bleomycins are large water soluble glycoproteins which are derived from the bacteria *Streptomyces verticillus.* Bleomycins are known to chelate metal ions, which enhances their cytotoxicity towards cancerous cells.[98]

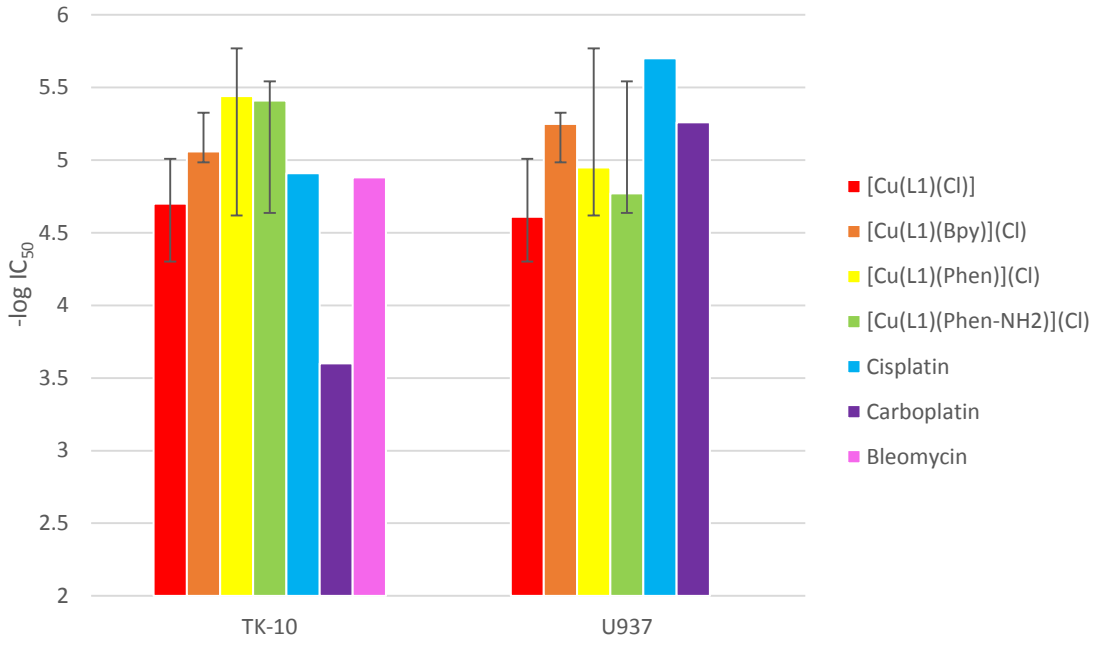

Figure 7.3.2: Comparison of the cytotoxicity of the copper(II) chelates with cisplatin, carboplatin and bleomycin.

From the graph in Figure 7.3.2 it can be concluded that the copper chelates are more active against the TK-10 cell line when compared to the commercially available agents. The three heteroleptic copper(II) chelates showed higher activity than cisplatin and bleomycin, while the single-ligand copper(II) chelate were less active. Carboplatin is the least active of all the compounds listed. These data show that in terms of cytotoxicity the copper(II) chelates synthesised in this work have potential as chemotherapeutics.

7.4 Conclusions

Both the single-ligand and heteroleptic copper(II) chelates were screened against a panel of four human cell lines: HEK293, TK-10, U937 and MT-4. Of the four cell lines, one was a normal human cell line which was used as control (HEK293). From the graph in Figure 7.3.1, the most active chelate was found to be $[Cu(L)(Cl)_2]$ with the highest mean activity (-log IC_{50} = 5.60 µM) across all cancer cell lines. This chelate also showed the lowest toxicity towards the healthy cell line. $[Cu(L2)(Cl)_2]$ which is comparable in structure to $[Cu(L)(Cl)_2]$ exhibited the second highest mean activity (-log IC_{50} = 5.49 µM).

The copper(II) chelates showed cytotoxicity against all four cell lines including the control cell line of normal cells. This highlights the importance of selective drug delivery to ensure that the compounds are selective towards cancerous tissue only. There is no correlation between

the DNA binding affinity and cytotoxicity. This suggests a more complex mechanism of action and that the redox activity and the production of ROS *in vitro* is a key step in the induction of cell apoptosis.

The chelates all showed enhanced activity against the TK-10 cell line, even having higher activity than cisplatin, carboplatin and bleomycin. The potential of the copper(II) chelates for the treatment of other leukaemia cell lines therefore warrants further testing.

These data confirm that each compound has a unique cytotoxicity profile and can be regarded as genuine chemotherapeutics with a well-defined mechanism of action and are not merely poisons. The cytotoxicity of the copper(II) compounds compare well with previously reported copper(II) chelates.

Chapter 8 | Conclusions and Future Work

8.1 Conclusions

A range of copper(II) Schiff base single-ligand and heteroleptic chelates for potential use as chemotherapeutic agents were successfully synthesised and characterised (Figure 8.1.1). The metal serves two functions: firstly, acting as a scaffold around which DNA-targeting ligands can be arranged. Secondly, the biologically accessible redox potential of the metal can catalyse the production of reactive oxygen species *in vitro*.

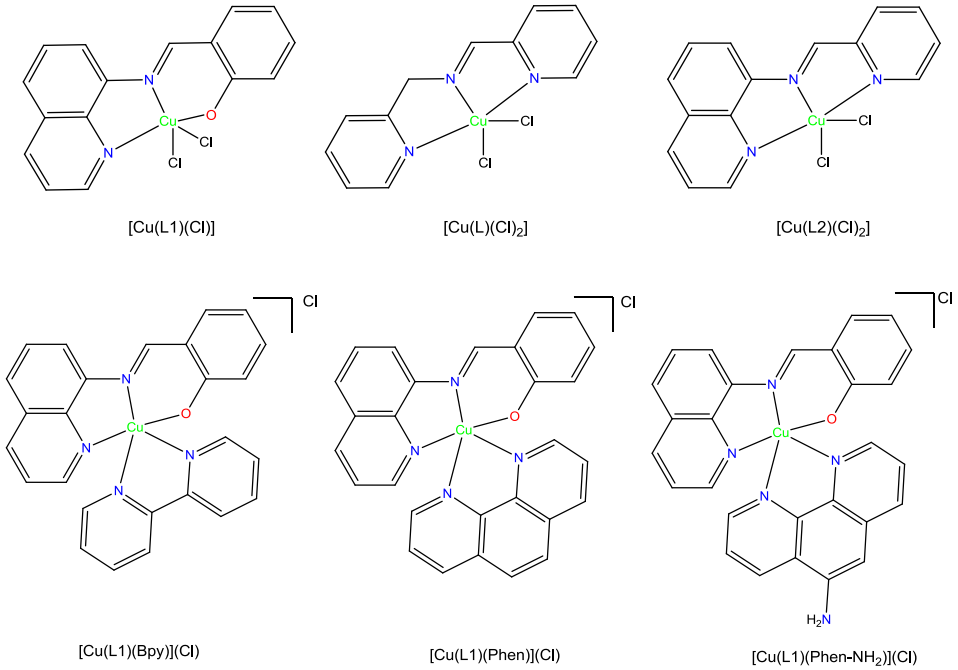

Figure 8.1.1: Structures of the copper(II) Schiff base complexes successfully synthesised in this work.

The *N,N',N''* and *N,N',O* donor Schiff base ligands were synthesised in a one-step, one-pot reaction involving the condensation between the respective aldehydes and amines in a 1:1 ratio. The ligands were characterized by ^{1}H and ^{13}C NMR experiments. In the case of the single-ligand chelates, the metal complexes were synthesised by reacting the respective Schiff base ligands with $CuCl_2$ in a 1:1 molar ratio. The isolated green precipitate of [Cu(L1)(Cl)] was then further reacted with three co-ligands: Bpy, Phen and Phen-NH_2 to afford the three heteroleptic complexes.

IR, Uv/vis and NMR spectroscopy, mass spectrometry and CHN analysis were employed to confirm the identity of the copper(II) chelates. Uv/vis spectroscopy illustrated that as the conjugation increases by the addition of a co-ligand the spectra gains a $\pi \rightarrow \pi^*$ band between 240 - 300 nm depending on the structure of the co-ligand. The MLCT band at approximately 420 nm is ubiquitous in all spectra confirming the presence of the copper(II) metal centre.

The DNA binding affinity of the chelates was studied using fluorescence competitive binding DNA titrations and showed the influence of structural differences on the DNA binding affinities. The K_{app} values of the six chelates range from 1.2(2) - 8.7(2) × 10^5 M^{-1} these compare favourably with the DNA binding affinity measured for the strong DNA intercalator ethidium bromide (7.75 × 10^5 M^{-1}). [Cu(L1)(Cl)] showed the highest DNA binding with a K_{app} value of 8.65 × 10^5 M^{-1}. The copper(II) chelates were also shown to produce hydroxyl radicals in the presence of hydrogen peroxide and ascorbate using a hydroxyl radical assay with Rhodamine B. This is significant as it is a key component in the mechanism of action of copper(II)-based drugs.

The solid state structures of two single-ligand and three heteroleptic chelates were successfully elucidated using X-ray crystallography. Interestingly, [Cu(L2)(Cl_2)] crystallized as two pseudopolymorphs where one lattice was solvated with a methanol molecule and the other was solvent-free. The copper(II) chelates all exhibited a square pyramidal coordination geometry around the metal centre which is in keeping with reported chelates of this class. The bond lengths and bond angles of the metal chelates were comparable to those reported in literature. Measurements of the angles between the ligand planes were taken and showed interesting variations of ring bending as well as angle deviations of the three heteroleptic complexes. The solid state interactions, particularly hydrogen bonding, of which these chelates are capable, provided important links between the solid-state structures and DNA binding affinities.

The geometry optimisations for all copper(II) chelates were performed at the B3LYP/6-311G(d,p) level of theory. A good correlation was observed between the gas phase and solid state structures for all chelates. This was indicated by low RMSDs and indicates that the structures had to undergo minimal structural deformations to allow for optimum packing in the solid state. The B3LYP/6-311G(d,p) level of theory which was chosen for the DFT simulations was therefore appropriate and the data calculated for the gas phase structures was likely reliable. The main difference in all the structures was the angle subtended by the co-ligands; both the chloro ligands and the bidentate N-donor ligands.

The copper(II) chelates were screened against a panel of four human cell lines: one normal cell line (HEK293) and three cancerous cell lines (TK-10, U937, MT-4). The HEK293 cell line was used as a control to investigate any specificity towards neoplastic tissue. The copper(II) chelates in general showed similar cytotoxicity in both the healthy and tumour cells. This data

therefore highlights the need for targeted drug delivery to ensure the chelates are selective towards cancerous tissue (*vida infra*).

The most active chelate was found to be $[Cu(L)(Cl)_2]$ with the highest mean cytotoxicity (IC_{50} = 2.19 μM). Interestingly, the same chelate showed the lowest toxicity towards the healthy cell line HEK293 (IC_{50} = 3.18). This chelate could therefore be more suitable as the primary ligand for the development of the next generation of heteroleptic chelates. There was no correlation between DNA binding affinity and cytotoxicity. This suggests that the catalytic production of ROS *in vitro*, which are known to cleave DNA and induce apoptosis, is likely a key step in the mechanism of action.

The proposed objectives of the project have been accomplished: DNA binding copper(II)-based chemotherapeutics with good cytotoxicity have been successfully synthesised. The data obtained have shown a few interesting trends and will be an excellent grounding to many avenues of future research.

8.2 Future work

The research on the copper(II) chelates in this study shows there is significant potential for further development as chemotherapeutic agents. This preliminary data opens the floor to several possible areas of research which require further development. In the present work, two phenanthroline-derivatised co-ligands were also successfully synthesised and characterized by ^{1}H and ^{13}C NMR experiments: L3 and L4. These ligands contained a biotin and propionic acid substituent, respectively, appended to phenanthroline by an amide bond. Biotin was incorporated into the co-ligand design to aid with biodistribution of the chelates, making them more selective towards neoplastic tissue. Since many tumour cell lines over-express receptor sites for this important growth factor, appending it to the chelates should increase uptake in cancerous tissue. The propionic acid derived ligand (L4) was synthesised as a control since both co-ligands contain the secondary amide functional group. Bioactivity studies, such as DNA binding and cell screening, will be undertaken on both to investigate the role biotin plays in terms of biodistribution and cell uptake. The proposed structures of chelates [Cu(L1)(L3)](Cl) and [Cu(L1)(L4)](Cl) are shown in Figure 8.2.1.

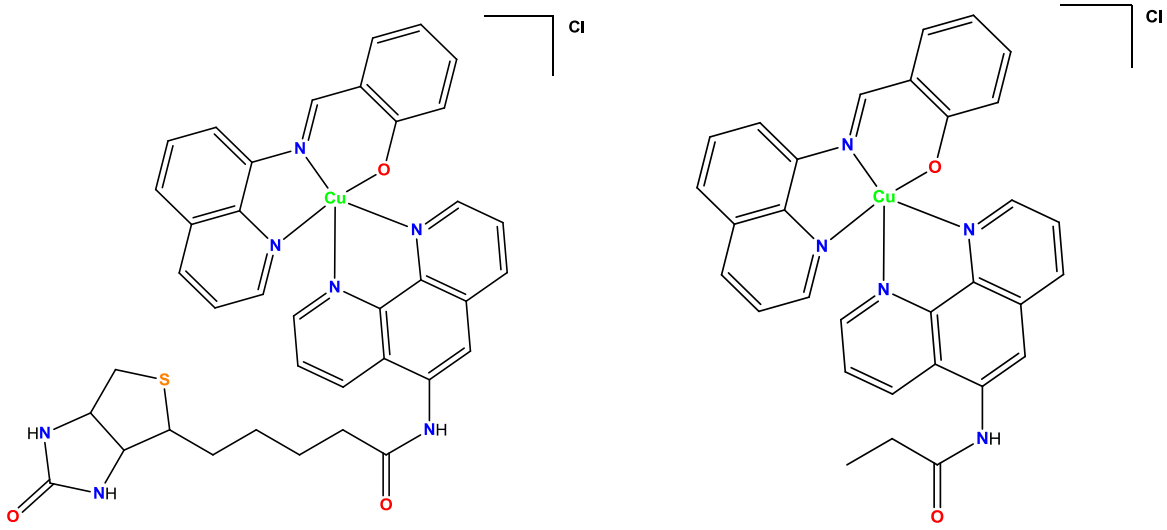

Figure 8.2.1: Structural formulae for chelates [Cu(L1)(L3)(Cl)] and [Cu(L1)(L4)(Cl)].

Preliminary data for the synthesis of the above compounds is promising with the synthesis of both chelates confirmed using mass spectrometry. [Cu(L1)(L3)(Cl)] will be further discussed as a representative example for both chelates. The mass spectrum in Figure 8.2.2 shows a base peak of 731.2191 m/z which correlates to the molecular ion peak of [Cu(L1)(L3)(Cl)] (M^+). The peak at 733.2188 m/z shows the expected isotopic ratio of Cu-63 and Cu-65 and is indicative of successful metal ion chelation.

However, the spectrum also shows a number of unwanted materials. The two largest impurity peaks are 310.0352 m/z which correlates to [Cu(L1)(Cl)](M^+), the primary ligand, while the peak 444.1732 m/z correlates to the biotin co-ligand's mass. These peaks highlight that the reaction does not go to completion and further method development is still required.

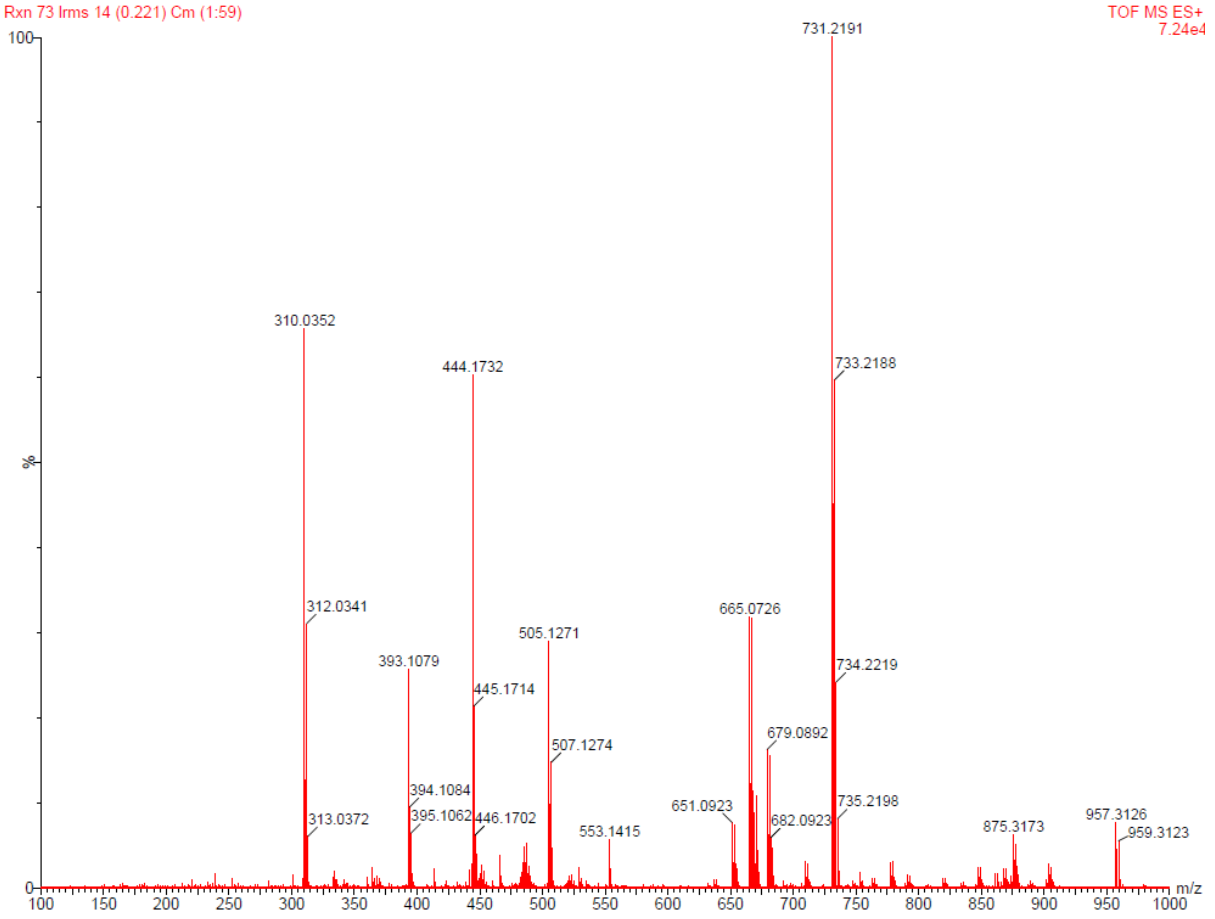

Figure 8.2.2: Mass spectrum of [Cu(L1)(L3)(Cl)].

In terms of co-ligand design and biodistribution, a study by Slim *et al.* successfully synthesised the biotin derivatized DPPZ ligand.[99] The DPPZ-Biotin ligand along with its propionic acid derivative will also be synthesised as co-ligands in the future development of the heteroleptic complexes. Another study by Bos *et al.*[100] showed the successful synthesis of a Bpy derivatized ligand which will be further reacted with biotin using methods previously described in this study for the synthesis of L3 and L4. Once again, the propionic acid derivative will also be synthesised for comparative studies. Figure 8.2.3 firstly shows a reaction scheme for the two desired ligands followed by the predicted chelate structures for the respective heteroleptic chelates.

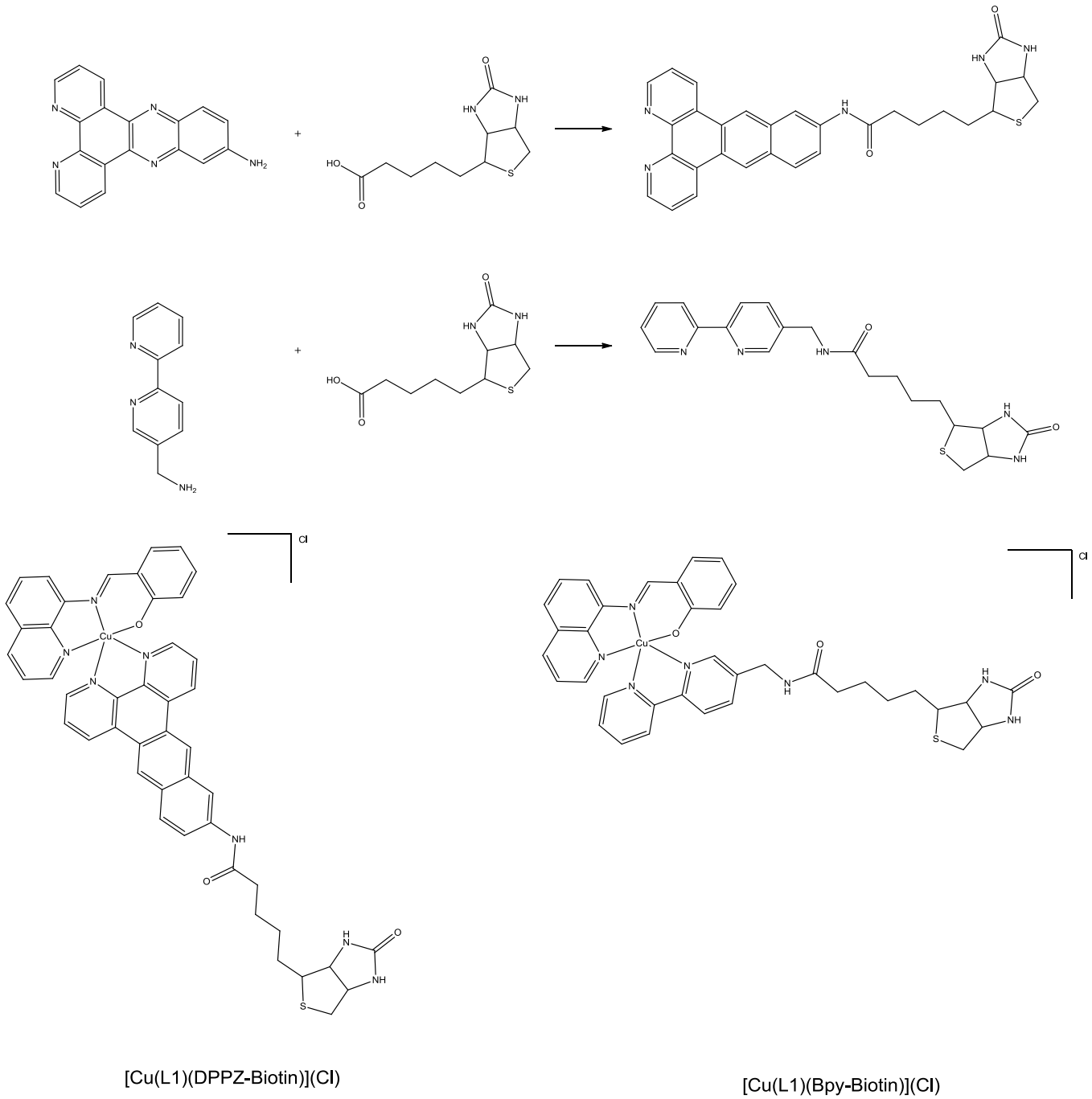

Figure 8.2.3: Reaction schemes for the synthesis of co-ligands DPPZ-Biotin and Bpy-Biotin, as well as the structure of the desired copper(II) chelates.

Another chelate modification will include changing the primary *N,N',O* donor Schiff base ligand as was used in this research to an *N,N',N''* donor Schiff base ligand. There are numerous possible *N,N',O* and *N,N',N''* donor Schiff base ligands, however, preference will be given to the Schiff bases which have already shown cytotoxic properties in the current study, i.e. ligand L from $[Cu(L)(Cl)_2]$.

In the early stages of drug design, the lipophilicity of the compounds has been shown to be a key physico-chemical property for determining biodistribution. The octonal-water partition coefficients will therefore be measured in the future work of this project. Lipophilicity gives

insight into the behaviour of the copper(II) chelates in the mammalian environment in terms of distribution, absorption, metabolism and excretion. It is also a reflection of the ability of a compound to permeate the cell membranes in a living organism.[101] The intended cellular target of the copper(II) chelates is DNA. Therefore the efficiency with which the drugs can cross the phospholipid bilayer of cells is a key parameter in determining their success as chemotherapeutics. It has also been shown that any small changes to the structure of metal chelates can have a marked effect on cell uptake and biodistribution.

DNA binding studies carried out in this work showed promising binding affinities as determined *via* competitive DNA binding studies. The exact mode through which the chelates bind to the DNA is, however, unknown. The method applied does not discriminate between intercalation and groove binding. Gel electrophoresis and DNA melting experiments will be carried out to investigate the exact DNA binding mode. In gel electrophoresis the mobility of the DNA through the agarose gel is largely dependent on the length of the DNA molecule. If the copper(II) chelate intercalates the DNA strand, the strand is lengthened resulting in reduced mobility.[102]

Melting of DNA is a phenomenon observed when double-stranded DNA molecules are heated and separated into two single strands. This is caused by disruption of the intermolecular forces such as π-π stacking and hydrogen bonding interactions which stabilise the DNA helix. This is monitored by the resulting hyperchromic effect in the DNA absorption spectra. The melting temperature (T_m) is the temperature at which half of the total base pairs are un-bonded and is easily measured form a DNA melting curve. The presence of a molecule intercalated between the double-stranded DNA will result in a notable increase in the value of T_m. Results from DNA melting will provide insight into the binding mode of the copper(II) chelates.[102]

The copper(II) chelates in this study have been tested against four human cell lines from MINTEK in order to determine a cross section of the cytotoxicity profile. An improved, more accurate representation of the cytotoxicity can be achieved by increasing the number of cell lines with the National Cancer Institute's sixty human cell line panel (NCI 60). This will provide an activity profile for the chelates which can be compared with other compounds with known modes of action, giving an indication of the likely mechanism of action. These data will also be important as the preliminary data has shown increased cytotoxicity towards leukaemia cells. Testing the chelates against different forms of leukaemia will confirm a preference for the treatment of leukaemia.

Further studies that are still to be carried out on all existing and the proposed paramagnetic copper(II) chelates using Electron Spin Resonance (ESR) spectroscopy since NMR is not amenable to the study of paramagnetic copper(II) chelates.

Lastly, the copper(II) chelates will be radiolabelled using the isotope ^{64}Cu. Radiolabelling the chelates will enable several experiments such as biodistribution determination, PET imaging applications and xenograft experiments. In biodistribution experiments, the radiolabelled ^{64}Cu chelates are injected into Sprague Dawley rats. After a set period of time, the rats are sacrificed and the radioactivity of each organ is measured. This is an important test for copper(II)-based drugs as if the metal ion is not sufficiently stabilised toxic liver accumulation is observed. This would prevent their application as metallodrugs.

The radiolabelled chelates will also be utilised in xenograft experiments. These experiments will determine whether the chelates are selective towards neoplastic vs healthy tissue as well as show whether the chelates can reduce the size of tumours *in vivo*. A 'sack' of cancerous cells is inserted into an animal followed by a dose of the chelate, which is administered intravenously. After a set amount of time the xenograft is removed and the growth of the cells measured. The selective tissue uptake of the chelate is also measured by the radioactivity of the xenograft.

PET is an imaging technique in which a computer-generated image of a radioactive tracer distributed in tissue is produced through the detection of annihilation photons (refer to the introduction for a full explanation). These photons are emitted when radionuclides are introduced into the body, decay and release positrons. PET is a favourably sensitive, non-invasive imaging technique that is well suited for pre-clinical and clinical imaging of cancerous regions in the body. The imaging of target molecules which are associated with cancer should allow for earlier diagnosis and better management of oncology patients.

An eventual goal of this project is to develop "theranostic" agents, a compound in which a combination of diagnostic and therapeutic capabilities exist in a single agent. The addition of cell targeting groups as discussed above will be key to achieving this goal.

References

1. Cancer Statistics. http://www.cancer.gov/about-cancer/understanding/statistics (accessed 26/08/2016).

2. M. Galanski, V. B. Arion, M. A. Jakupec and B. K. Keppler; *Current Pharmaceutical Design,* **2003,** *9* (25), 2078-2089.

3. R. P. Feldman and J. T. Goodrich; *Child's Nervous System,* **1999,** *15* (6-7), 281-284.

4. J. P. Ruparelia, A. K. Chatterjee, S. P. Duttagupta and S. Mukherji; *Acta Biomaterialia,* **2008,** *4* (3), 707-716.

5. M. J. Hannon; *Pure and Applied Chemistry,* **2007,** *79* (12), 2243-2261.

6. I. Ott and R. Gust; *Archiv der Pharmazie,* **2007,** *340* (3), 117-126.

7. I. Ott; *Coordination Chemistry Reviews,* **2009,** *253* (11–12), 1670-1681.

8. P. C. A. Bruijnincx and P. J. Sadler; *Current opinion in chemical biology,* **2008,** *12* (2), 197-206.

9. A Brief History of The Health Support Uses of Copper. https://www.purestcolloids.com/history-copper.php (accessed 07/10/2016).

10. C. J. Anderson and R. Ferdani; *Cancer Biotherapy and Radiopharmaceuticals,* **2009,** *24* (4), 379-393.

11. B. Murphy and B. Hathaway; *Coordination chemistry reviews,* **2003,** *243* (1), 237-262.

12. M. Magini; *Inorganic Chemistry,* **1982,** *21* (4), 1535-1538.

13. H. Dollwet and J. Sorenson; *Trace elements in Medicine,* **1985,** *2* (2), 80-87.

14. R. B. Thurman, C. P. Gerba and G. Bitton; *Critical Reviews in Environmental Science and Technology,* **1989,** *18* (4), 295-315.

15. A. Samuni, M. Chevion and G. Czapski; *Radiation research,* **1984,** *99* (3), 562-572.

16. R. Sterritt and J. Lester; *Science of the Total environment,* **1980,** *14* (1), 5-17.

17. C. Manzl, J. Enrich, H. Ebner, R. Dallinger and G. Krumschnabel; *Toxicology,* **2004,** *196* (1), 57-64.

18. M. J. Domek, M. W. LeChevallier, S. C. Cameron and G. A. McFETERS; *Applied and Environmental Microbiology,* **1984,** *48* (2), 289-293.

19. R.-Ș. Mezey, I. Máthé, S. Shova, M.-N. Grecu and T. Roșu; *Polyhedron,* **2015,** *102*, 684-692.

20. B. G. Que, K. M. Downey and A. G. So; *Biochemistry,* **1980,** *19* (26), 5987-5991.

21. J. Luis García-Giménez, M. González-Álvarez, M. Liu-González, B. Macías, J. Borrás and G. Alzuet; *Journal of Inorganic Biochemistry,* **2009,** *103* (6), 923-934.

22. B. M. Zeglis, V. C. Pierre and J. K. Barton; *Chemical Communications,* **2007,** (44), 4565-4579.

23. J. M. Ollinger and J. A. Fessler; *IEEE Signal Processing Magazine,* **1997,** *14* (1), 43-55.

24. J. M. Ollinger and J. A. Fessler; IEEE Signal Processing Magazine, **1997**, (14) (1), 57-63

25. D. Delbeke, R. E. Coleman, M. J. Guiberteau, M. L. Brown, H. D. Royal, B. A. Siegel, D. W. Townsend, L. L. Berland, J. A. Parker and K. Hubner; *Journal of Nuclear Medicine,* **2006,** *47* (5), 885-895.

26. S. S. Gambhir; *Nature Reviews Cancer,* **2002,** *2* (9), 683-693.

27. D. L. Smith, W. A. P. Breeman and J. Sims-Mourtada; *Applied Radiation and Isotopes,* **2013,** *76*, 14-23.

28. I. Velikyan; *Theranostics,* **2014,** *4* (1), 47.

29. A. Kumar, S.-T. Lo, O. K. Öz and X. Sun; *Bioorganic & Medicinal Chemistry Letters,* **2014,** *24* (24), 5663-5665.

30. J. Lux, A. G. White, M. Chan, C. J. Anderson and A. Almutairi; *Theranostics,* **2015,** *5* (3), 277.

31. S.-Y. Qin, M.-Y. Peng, L. Rong, H.-Z. Jia, S. Chen, S.-X. Cheng, J. Feng and X.-Z. Zhang; *Nanoscale,* **2015,** *7* (35), 14786-14793.

32. D. N. Heo, D. H. Yang, H.-J. Moon, J. B. Lee, M. S. Bae, S. C. Lee, W. J. Lee, I.-C. Sun and I. K. Kwon; *Biomaterials,* **2012,** *33* (3), 856-866.

33. A. Taheri, R. Dinarvand, F. S. Nouri, M. R. Khorramizadeh, A. T. Borougeni, P. Mansoori and F. Atyabi; *Int J Nanomedicine,* **2011,** *6*, 1863-1874.

34. J. Xie, S. Lee and X. Chen; *Advanced drug delivery reviews,* **2010,** *62* (11), 1064-1079.

35. M. Sirajuddin, N. Uddin, S. Ali and M. N. Tahir; *Spectrochimica Acta Part A: Molecular and Biomolecular Spectroscopy,* **2013,** *116*, 111-121.

36. X. Qiao, Z.-Y. Ma, C.-Z. Xie, F. Xue, Y.-W. Zhang, J.-Y. Xu, Z.-Y. Qiang, J.-S. Lou, G.-J. Chen and S.-P. Yan; *Journal of Inorganic Biochemistry,* **2011,** *105* (5), 728-737.

37. Q.-P. Qin, Y.-L. Li, Y.-C. Liu and Z.-F. Chen; *Inorganica Chimica Acta,* **2014,** *421*, 260-266.

38. J. Ravichandran, P. Gurumoorthy, M. I. Musthafa and A. K. Rahiman; *Spectrochimica Acta Part A: Molecular and Biomolecular Spectroscopy,* **2014,** *133*, 785-793.

39. M. Ganeshpandian, S. Ramakrishnan, M. Palaniandavar, E. Suresh, A. Riyasdeen and M. A. Akbarsha; *Journal of Inorganic Biochemistry,* **2014,** *140*, 202-212.

40. K. J. Akerman, A. M. Fagenson, V. Cyril, M. Taylor, M. T. Muller, M. P. Akerman and O. Q. Munro; *Journal of the American Chemical Society,* **2014,** *136* (15), 5670-5682.

41. C. Liu, Y. Zhu and M. Tang; *Journal of Molecular Graphics and Modelling,* **2016,** *64*, 11-29.

42. B. Dumat, G. Bordeau, E. Faurel-Paul, F. Mahuteau-Betzer, N. Saettel, M. Bombled, G. Metgé, F. Charra, C. Fiorini-Debuisschert and M.-P. Teulade-Fichou; *Biochimie,* **2011,** *93* (8), 1209-1218.

43. P. Gurumoorthy, D. Mahendiran, D. Prabhu, C. Arulvasu and A. K. Rahiman; *Journal of Molecular Structure,* **2015,** *1080*, 88-98.

44. P. Y. Bruice, *Organic Chemistry*. 5th ed.; Prentice Hall: 2006.

45. C. A. Montalbetti and V. Falque; *Tetrahedron,* **2005,** *61* (46), 10827-10852.

46. M. Slim and H. F. Sleiman; *Bioconjugate chemistry,* **2004,** *15* (5), 949-953.

47. A. K. Ghose, V. N. Viswanadhan and J. J. Wendoloski; *Journal of Combinatorial Chemistry,* **1999,** *1* (1), 55-68.

48. A. Fullick and P. Fullick, *Chemistry*. First ed.; Heinemann Educational Publishers: Oxford, 1994.

49. T. Moeller, J. John C. Bailar, J. Kleinberg, C. O. Guss, M. E. Castellion and C. Metz, *Chemistry with Inorganic qualitative analysis.* Third ed.; Harcourt Brace Jovanovich Publishers: USA, 1989.

50. P. Y. Bruice, *Organic Chemistry*. sixth ed.; Prentice Hall: USA, 2011.

51. M. P. Akerman and V. A. Chiazzari; *Journal of Molecular Structure,* **2014,** *1058*, 22-30.

52. M. Ramana, R. Betkar, A. Nimkar, P. Ranade, B. Mundhe and S. Pardeshi; *Journal of Photochemistry and Photobiology B: Biology,* **2015,** *151*, 194-200.

53. J. Ravichandran, P. Gurumoorthy, M. A. Imran Musthafa and A. Kalilur Rahiman; *Spectrochimica Acta Part A: Molecular and Biomolecular Spectroscopy,* **2014,** *133*, 785-793.

54. D. Khare and R. Pande; *J Der Pharma Chemica,* **2012,** *4*, 66-75.

55. L.-M. Chen, J. Liu, J.-C. Chen, C.-P. Tan, S. Shi, K.-C. Zheng and L.-N. Ji; *Journal of inorganic biochemistry,* **2008,** *102* (2), 330-341.

56. C. Rajarajeswari, M. Ganeshpandian, M. Palaniandavar, A. Riyasdeen and M. A. Akbarsha; *Journal of inorganic biochemistry,* **2014,** *140*, 255-268.

57. V. Rajendiran, R. Karthik, M. Palaniandavar, V. S. Periasamy, M. A. Akbarsha, B. S. Srinag and H. Krishnamurthy; *Inorganic Chemistry,* **2007,** *46* (20), 8208-8221.

58. P. Jaividhya, R. Dhivya, M. A. Akbarsha and M. Palaniandavar; *Journal of Inorganic Biochemistry,* **2012,** *114*, 94-105.

59. L. M. Gaetke and C. K. Chow; *Toxicology,* **2003,** *189* (1), 147-163.

60. U. Ashraf, O. A. Chat and A. A. Dar; *Chemosphere,* **2014,** *99*, 199-206.

61. T. P. Szatrowski and C. F. Nathan; *Cancer research,* **1991,** *51* (3), 794-798.

62. F. H. Allen; *Acta Crystallographica Section B: Structural Science,* **2002,** *58* (3), 380-388.

63. A. Hens, P. Mondal and K. K. Rajak; *Dalton Transactions,* **2013,** *42* (41), 14905-14915.

64. D. Gong, B. Wang, X. Jia and X. Zhang; *Dalton Transactions,* **2014,** *43* (10), 4169-4178.

65. F. T. Esmadi and T. Z. Irshaidat; *Synthesis and Reactivity in Inorganic and Metal-Organic Chemistry,* **2000,** *30* (7), 1347-1362.

66. J. Wagler, D. Gerlach and G. Roewer; *Inorganica chimica acta,* **2007,** *360* (6), 1935-1942.

67. W.-H. Sun, K. Wang, K. Wedeking, D. Zhang, S. Zhang, J. Cai and Y. Li; *Organometallics,* **2007,** *26* (19), 4781-4790.

68. G. Paolucci, A. Zanella, L. Sperni, V. Bertolasi, M. Mazzeo and C. Pellecchia; *Journal of Molecular Catalysis A: Chemical,* **2006,** *258* (1), 275-283.

69. S. K. Padhi, R. Sahu and V. Manivannan; *Polyhedron,* **2008,** *27* (2), 805-811.

70. R. N. Patel, A. Singh, K. K. Shukla, V. P. Sondhiya, D. K. Patel, Y. Singh and R. Pandey; *Journal of Coordination Chemistry,* **2012,** *65* (8), 1381-1397.

71. B. de Souza, A. J. Bortoluzzi, T. Bortolotto, F. L. Fischer, H. Terenzi, D. E. Ferreira, W. R. Rocha and A. Neves; *Dalton Transactions,* **2010,** *39* (8), 2027-2035.

72. R. K. Lin, C. H. Hsu, C. I. Chiu, Y. J. Lai, C. M. Chien and C. C. Lin; *Journal of the Chinese Chemical Society,* **2014,** *61* (12), 1333-1340.

73. B.-T. Ko, C.-C. Chang, S.-L. Lai, F.-J. Lai and C.-C. Lin; *Polyhedron,* **2012,** *45* (1), 49-54.

74. K. D. Karlin, J. C. Hayes, S. Juen, J. P. Hutchinson and J. Zubieta; *Inorganic Chemistry,* **1982,** *21* (11), 4106-4108.

75. A. Pyle, J. Rehmann, R. Meshoyrer, C. Kumar, N. Turro and J. K. Barton; *Journal of the American Chemical Society,* **1989,** *111* (8), 3051-3058.

76. B. A. Inc *Bruker APEX2, SAINT and SADABS*, Wisconsin, USA,, 2012.

77. L. J. Farrugia; *Journal of Applied Crystallography,* **1999,** *32* (4), 837-838.

78. G. M. Sheldrick; *Acta Crystallographica Section C: Structural Chemistry,* **2015,** *71* (1), 3-8.

79. (IUCr) checkCIF. checkcif.iucr.org (accessed 24 Oct 2016).

80. H. Liu, F. Gao, D. Niu and J. Tian; *Inorganica Chimica Acta,* **2009,** *362* (11), 4179-4184.

81. A. Hinchliffe, *Modelling molecular structures*. Second ed.; Wiley: Chichester, Sussex, 2000.

82. E. G. Lewars, *Computational Chemistry*. Second ed.; Springer: 2011.

83. C. J. Cramer, *Essentials of Computational Chemistry. Theories and Models*. Second ed.; John Wiley & Sons, Ltd: 2004.

84. J. P. Perdew, K. Burke and M. Ernzerhof; *Physical review letters,* **1996,** *77* (18), 3865.

85. A. McLean and G. Chandler; *The Journal of Chemical Physics,* **1980,** *72* (10), 5639-5648.

86. J. P. Perdew, K. Burke and M. Ernzerhof; *Phys. Rev. Lett,* **1997,** *78*, 1396.

87. R. Krishnan, J. S. Binkley, R. Seeger and J. A. Pople; *The Journal of Chemical Physics,* **1980,** *72* (1), 650-654.

88. P. J. Hay; *The Journal of Chemical Physics,* **1977,** *66* (10), 4377-4384.

89. K. Raghavachari and G. W. Trucks; *The Journal of chemical physics,* **1989,** *91* (2), 1062-1065.

90. A. J. H. Wachters; *The Journal of Chemical Physics,* **1970,** *52* (3), 1033-1036.

91. M. Frisch, G. Trucks, H. Schlegel, G. Scuseria, M. Robb, J. Cheeseman, G. Scalmani, V. Barone, B. Mennucci and G. Petersson; *Inc., Wallingford, CT,* **2009,** *4*.

92. G. L. Patrick, *An Introduction to Medicinal Chemistry*. third ed.; Oxford University Press: New York, 2005.

93. J. Lu, Q. Sun, J.-L. Li, L. Jiang, W. Gu, X. Liu, J.-L. Tian and S.-P. Yan; *Journal of inorganic biochemistry,* **2014,** *137*, 46-56.

94. J. A. Barltrop, T. C. Owen, A. H. Cory and J. G. Cory; *Bioorganic & Medicinal Chemistry Letters,* **1991,** *1* (11), 611-614.

95. E. C. Taylor and B. Liu; *The Journal of organic chemistry,* **2001,** *66* (11), 3726-3738.

96. W.-C. Su, S.-L. Chang, T.-Y. Chen, J.-S. Chen and C.-J. Tsao; *Japanese journal of clinical oncology,* **2000,** *30* (12), 562-567.

97. J. Fischer and C. R. Ganellin, *Analogue-based drug discovery II*. John Wiley & Sons: 2010.

98. G. L. Patrick, *An introduction to medicinal chemistry*. Oxford university press: 2013.

99. M. Slim, N. Durisic, P. Grutter and H. F. Sleiman; *ChemBioChem,* **2007,** *8* (7), 804-812.

100. J. Bos, F. Fusetti, A. J. Driessen and G. Roelfes; *Angewandte Chemie International Edition,* **2012,** *51* (30), 7472-7475.

101. P. Wattanasin, P. Saetear, P. Wilairat, D. Nacapricha and S. Teerasong; *Analytica chimica acta,* **2015,** *860*, 1-7.

102. C. M. Che, M. Yang, K. H. Wong, H. L. Chan and W. Lam; *Chemistry–A European Journal,* **1999,** *5* (11), 3350-3356.